博士論文

Multi-scale structures formed by the Tsushima Warm Current

in the Sea of Japan

（　対馬暖流が形成する日本海のマルチスケールな構造　）

矢部（重村）　いつか

博 士 論 文

Multi-scale structures formed by the Tsushima Warm Current

in the Sea of Japan

（　対馬暖流が形成する日本海のマルチスケールな構造　）

令和 3 年

東京大学大学院　新領域創成科学研究科

矢部（重村）　いつか

Contents

Abstract

The Sea of Japan, a familiar ocean adjacent to the Japanese archipelago, is controlled by various multi-scale phenomena: the Tsushima Warm Current (TWC), the Subpolar Front (SPF), the subarctic gyre, the abyssal circulation, mesoscale eddies, submesoscale structures, tides, internal waves, and turbulence. Comprehensive study is required to understand each phenomenon and their interactions precisely. However, such study has not conducted yet due to the lack of accumulation of observational data. The purpose of this thesis is to contribute to the overall understanding of the multi-scale phenomena in the Sea of Japan. We carried out research from two perspectives.

Firstly, the seasonal variation of the large-scale phenomena including the TWC, the SPF and mesoscale eddies were examined. These are the phenomena in the upper part of the Sea of Japan. Their pathways were determined based on the satellite-based sea surface height, which covers the entire area over 25 years. We specifically classified four branches based on their upstream positions around the Tsushima Strait and examined their downstream pathways which have not been clarified yet in the central and the eastern Sea of Japan. In regions west of 133°E, they mutually flow independently, whereas they become scrambled at eastern longitudes. Our analyses revealed that the three branches, excluding that along the SPF, showed a confluence in the regions around the Oki Islands

and off the Noto Peninsula. The seasonal variation of those branches is addressed by this study. In the Yamato Basin, the TWC branches, particularly the offshore south branch, were affected strongly by the seasonal development of mesoscale eddies and their location. Basin-wide anti-cyclonic and cyclonic eddies develop during winter and summer, respectively. In the eastern area, the TWC branches, mostly exiting towards the Pacific Ocean through the Tsugaru Strait, notably meander in winter, but they were straightforward in summer.

Secondly, small-scale phenomena such as inertial oscillation, internal gravity waves (IGWs) and turbulence were investigated based on the current velocities by the mooring system. Kinetic energy from atmospheric disturbances is one of the main sources in the Sea of Japan. IGWs transport it horizontally and vertically from the surface mixed layer to ocean interior. The near-inertial internal waves (NIWs) with the local inertial frequency are the most energetic among the IGWs in the Sea of Japan. Wind-induced NIWs were examined using a year-round mooring observation off Sado Island in the eastern part of the Sea of Japan. The mooring system was constructed by two sets of acoustic Doppler current profilers and seven of single-layer current meters, covering the upper 1200 m in the full depth of 1770 m. From the data, the local inertial frequency and its vicinity showed the dominant peak especially in the upper 1200 m in depth, which

persisted throughout the year. Any constituent from oceanic tide was negligibly small.

Downward propagation of wind-induced NIWs was clearly observed several times during the mooring period of 2019-2020. Noticeable events of NIW were initiated typically by cyclones passing in summer and relatively persistent outbreaks of northwesterly wind from the Eurasian continent in winter. In this region, meanderings of the TWC and mesoscale eddies add complexity to the behaviors of NIWs. Vertical shears of current velocities were strong at 200–300 m inside the anti-cyclonic eddy. The amplification of NIW signature occurred at depths near the bottom end of the eddy's core. On the other hand, vertical shears were strongest at the surface and decreasing with depth inside the cyclonic eddy. The gradient Richardson number suggested the turbulent mixing through the breaking of the NIWs by Kelvin-Helmholtz instability in all event terms. Around the depth of strong vertical shears (250–300 m), reflection of NIWs was identified from the slope of iso-phase lines. The reflection layer is the pycnocline between the TWC water and the Japan Sea Proper Water. Near-inertial oscillation was determined over the large portion of water column underneath the reflection layer. A large vertical wavelength from the refraction can account for the nearly barotropic nature in the lower layer.

Using actual oceanic data we have investigated multi-scale phenomena of the TWC, the SPF, mesoscale eddies, near-inertial oscillation, NIWs, and turbulence. The

importance of each phenomenon and their interactions were shown in the comprehensive

understanding of the current system.

1. General Introduction

Japan is surrounded by multiple seas, i.e., the Pacific Ocean, the Sea of Japan, the Sea of Okhotsk, and the East China Sea. The northwestern side of the Japanese Archipelago is extensively adjacent to the Sea of Japan (Fig. 1-1), which is an important fishing ground of mackerels, snow crabs, and tunas, and also a development field of natural resources and renewable energies. These industries are strongly influenced by oceanographic phenomena. Figure 1-2 illustrates phenomena in association with various spatial and temporal scales in the ocean (Cushman-Roisin and Beckers, 2011).

We summarize important oceanographic phenomena in the Sea of Japan as depicted in Fig. 1-3. The largest-scale phenomena are the Tsushima Warm Current (TWC), the Subpolar Front (SPF), the subarctic gyre, and the abyssal circulation. The TWC is the ocean current in the surface layer, which enters from the Tsushima Strait and exits through the Tsugaru and the Soya Straits to the North Pacific and the Sea of Okhotsk, respectively (Colored arrows in Fig. 1-1). The SPF is a temperature front between the TWC water and the surface water in the northern Sea of Japan. Eastward flow along the SPF is one of the TWC branches, which we call it as the Subpolar Front Current (SFC). The subarctic gyre, located north of the SPF, is a counterclockwise circulation consisting of the SFC, the Liman Current, and the North Korean Cold Current. In addition to these surface

circulations the abyssal circulation consisting of cyclonic circulations in the Japan, Ulleung, and Yamato Basins has been identified by mooring current measurements (Senjyu et al., 2005, Fig. 1-4).

The middle-scale phenomena are eddies and submesoscale phenomena. Mesoscale eddies have typical spatial scales of less than 100 km and time scales on the order of a month. Eddies are detached from meandering of the TWC, complicated bottom topography and coastlines in the Sea of Japan. These structures impact on hydrographic properties in coastal regions such as Wakasa and Toyama Bays (Kaneda et al. 2017; Igeta et al., 2017). Submesoscale phenomena are filamentary structures formed around mesoscale eddies and ocean currents whose spatial scale is approximately one order smaller than that of mesoscale eddies. Studies of submesoscale structure have just begun with advance of measurement.

The smallest time-scale phenomena are the tide, inertial oscillation, internal gravity wave (IGW), and turbulence. Tides are the oscillations caused by gravitational force of the sun and moon, which is extremely small in the Sea of Japan except for the area around the Tsushima Strait (Mori et al., 2005). Inertial oscillation is the stationary oscillation with a local inertial frequency, and it is commonly observed in the surface mixed layer after atmospheric disturbances pass over the seas. IGW is a wave propagating

horizontally and vertically, which plays a key role in the energy circulation in the ocean (Fig. 1-5) (Mackinnon et al., 2017). It also transfers kinetic energy to turbulent mixing through breaking such as by Kelvin-Helmholtz instability (Fig. 1-3) (Smyth and Moum, 2012).

The purpose of the thesis is to clarify these various phenomena and their relation. However, observation data are quite few in the Sea of Japan. The reasons are a severe climate in winter and the international boundary conflict around the adjacent nations. Shipboard observations are not possible in wintertime when the intense northwesterly monsoon blows on the Sea of Japan. The boundary conflict prevents international research projects and extensive shipboard measurement. To recover these deficiencies, we consider two possible ways as follows. The first is use of satellite altimetry. This observation is available for the whole area of the Sea of Japan and a long term through a year. Because it has a coarse resolution, it is suitably applicable to the large-scale phenomena in the surface layer, i.e., the TWC and the SFC. The second is use of mooring systems. This observation enables us to obtain time-series data of current velocities, hydrography, etc., in a short time interval of measurement. However, the location and term are limited, but by analyzing them, we clarify the small-scale phenomena.

Therefore, we focus our attention on two important phenomena. One is the TWC,

and the other is near-inertial internal wave (NIW). These phenomena respectively have a

prominent kinetic energy for the long-term phenomena and short-term one. The branching

of the TWC and their pathways in the southwestern Sea of Japan have already clarified

by observational and numerical studies, but their pathways and their variations in the

central and eastern Sea of Japan have not clarified yet (Kawabe, 1982a; Kato 1994; Hase

et al., 1999; Morimoto and Yanagi, 2001; Ito et al, 2014). Propagation behavior of NIW

is influenced by ocean currents and mesoscale eddies (Alford et al., 2016), but few

observational studies have been carried out from the full-depth current data.

The research project of Fisheries Research Agency – Atmosphere and Ocean

Research Institute Tsushima Warm Current Observatory (shortly, FATO) has been

launched in the year of 2017. The aim of the FATO is total elucidation of the TWC-related

oceanic phenomena detailed in Kawaguchi et al. (2021b). In FY 2019, three research

cruises had been carried out on this project (Table 1-1). Those will lead to the

determination of kinetic energy circulation over the wide area of Sea of Japan. We actively

participated in the planning, observations, and the recovery of data for all the mooring

and shipboard hydrographic observations to clarify the properties of NIW in association

with the mesoscale structure.

This thesis comprises the following chapters. In Chapter 2, we develop a method

to identify the pathways of the TWC system taking advantage of a satellite-based altimeter dataset. The TWC pathways and their variability are statistically analyzed. In Chapter 3, we clarify a behavior of wind-induced NIWs in the TWC water and the JSPW using the one-year mooring dataset obtained in the FATO project. In Chapter 4, we summarize the present study in terms of the multi-scale phenomena and discuss importance of the comprehensive studies on them in the Sea of Japan. Chapter 2 have been published as Yabe et al. (2021a) and Yabe et al. (2021b), respectively.
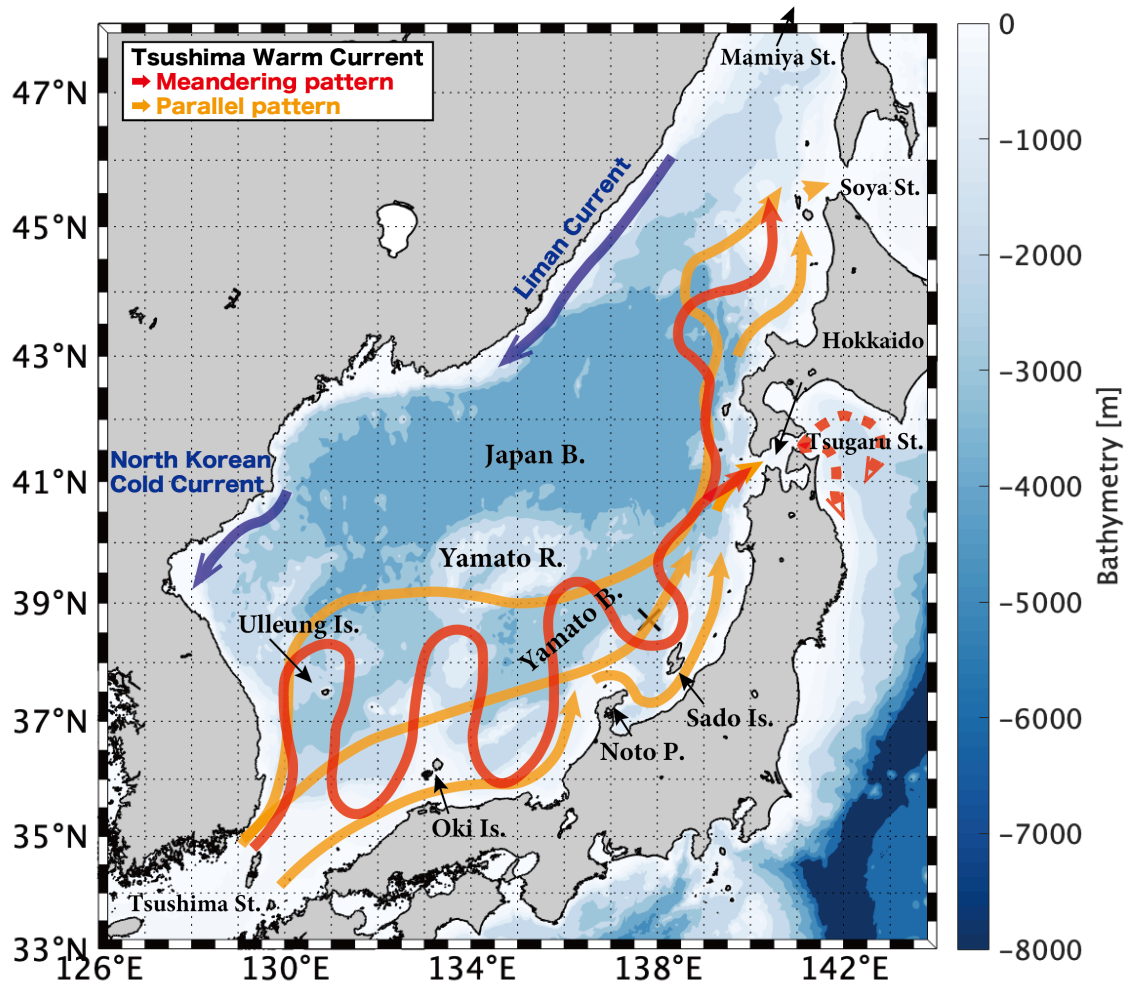
Fig.1-1: Schematic map of the TWC system. Colored solid arrows indicate the ocean currents with reference to Naganuma (1985). Blue shading represents bottom topography. Abbreviations for current names are the following: NKCC, North Korean Cold Current; and LC, Liman Current. The black cross mark denotes the position of the mooring station.
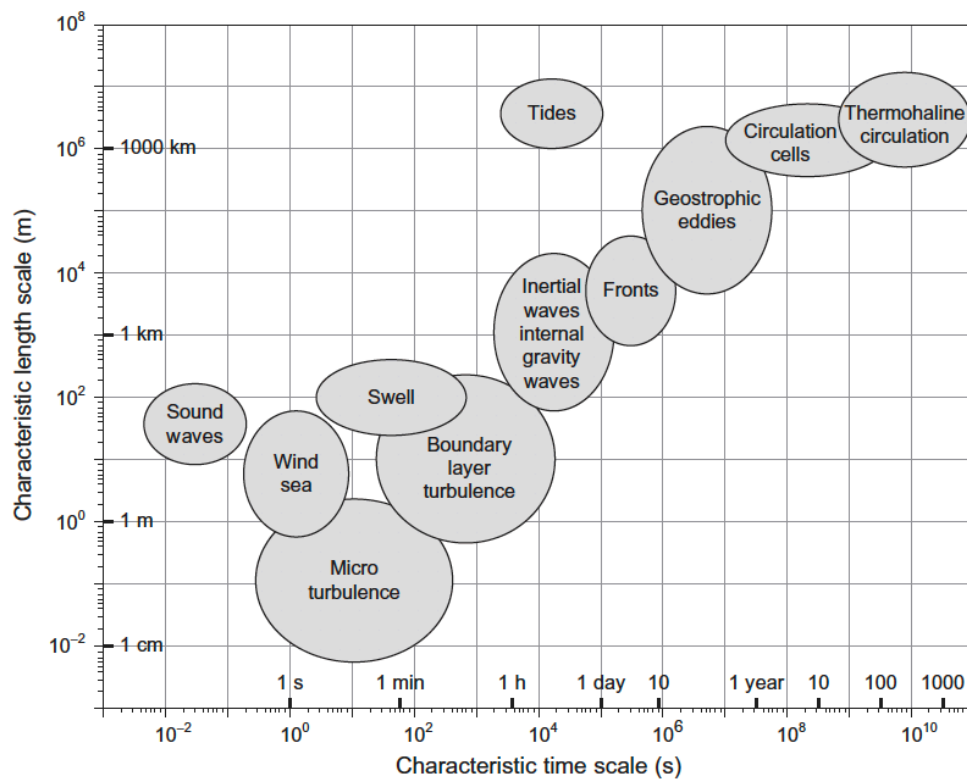
Fig.1-2: Phenomena in association with various spatial and temporal scales in the ocean (Fig. 1-7 of Cushman-Roisin and Beckers, 2011).
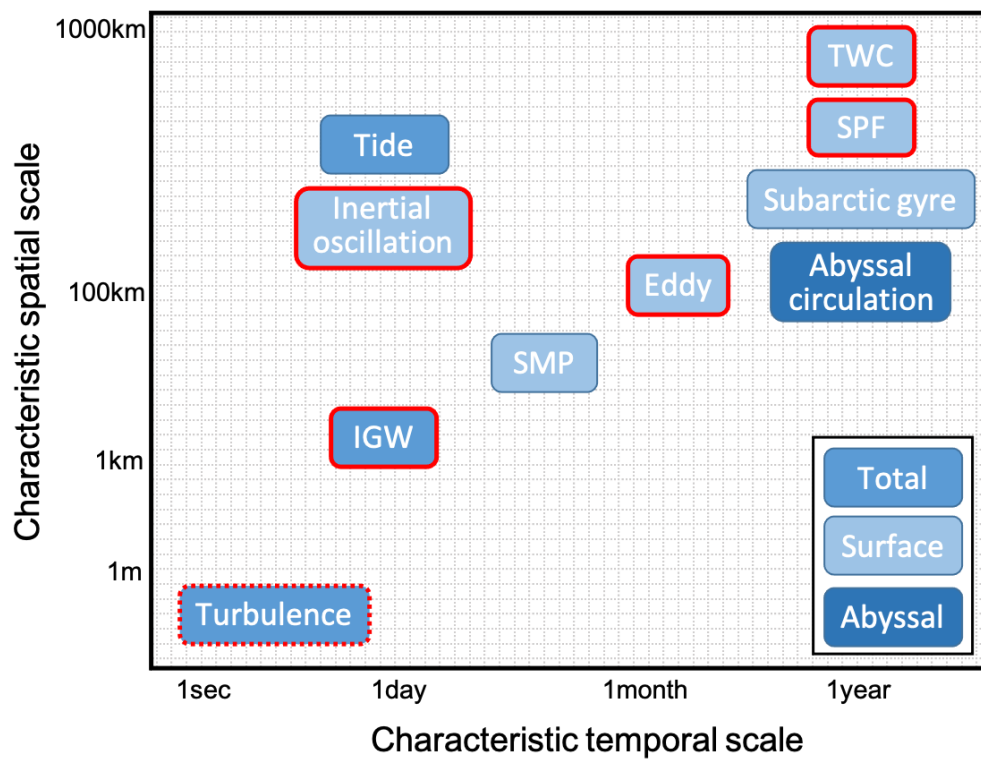
Fig.1-3: Oceanographic phenomena in the Sea of Japan. Abbreviations are the following: TWC, Tsushima Warm Current; SPF, Subpolar Front; SMP, Submesoscale phenomena; IGW, Internal gravity wave. Phenomena marked by a red frame are objects in this study.
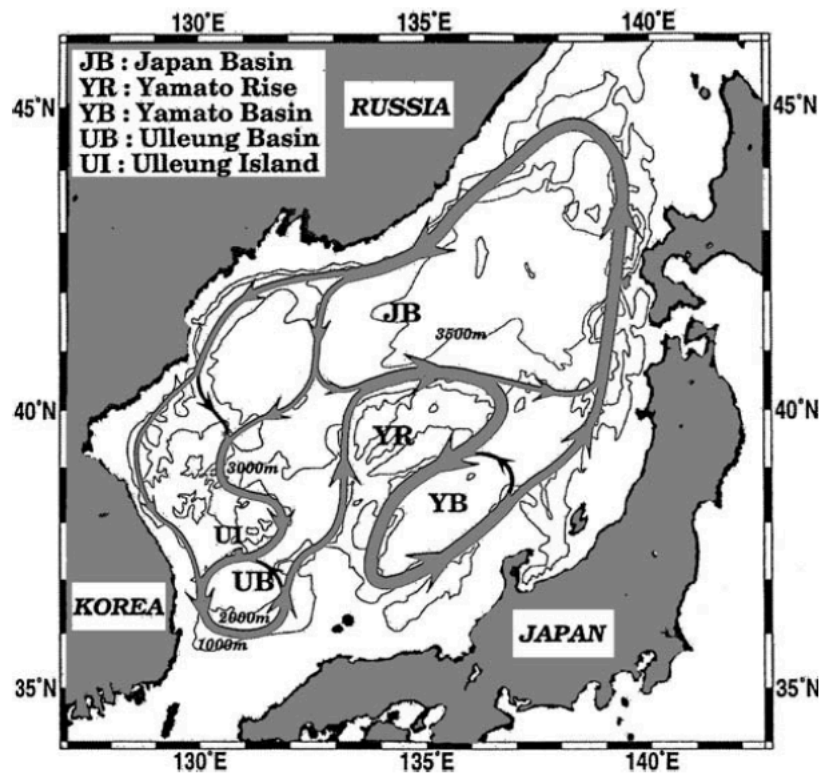
Fig.1-4: Schematic map of the abyssal circulation based on moored current measurements (adapted from Senjyu et al., 2005, Fig. 12). Specific geographical names in the Sea of Japan study domain are shown in abbreviation.
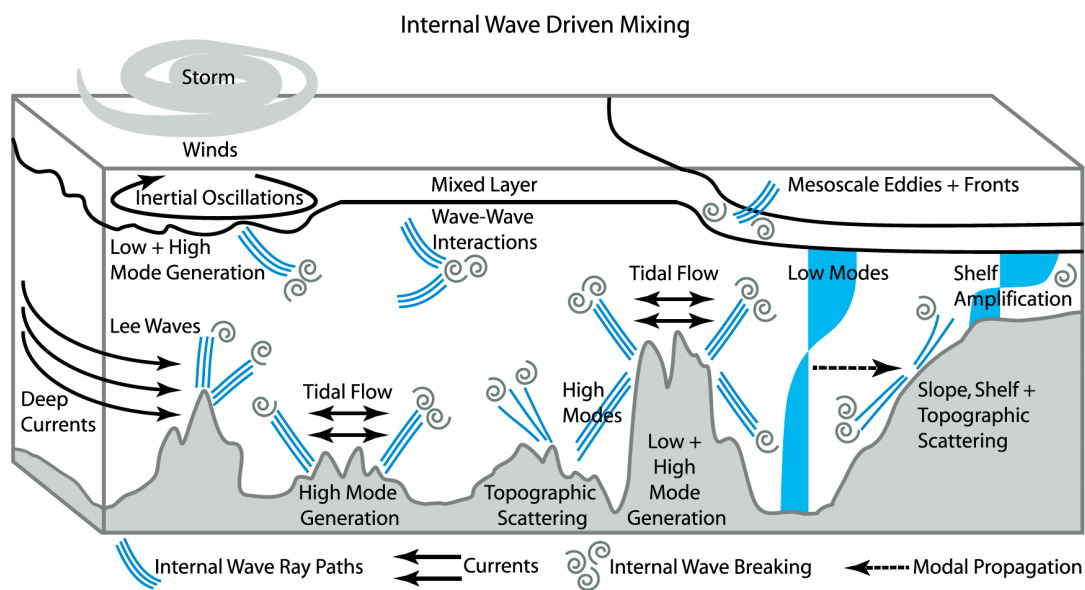
Fig.1-5: Schematic illustration of internal waves and mixing process in the open ocean. Adapted from Mackinnon et al. (2017).

Table 1-1: A list of scientific cruises that I participated for my Ph.D research.

Cruises	Dates
TY1906	13 Jun. 2019–24 Jun. 2019
OS1907	7 Jul. 2019–18 Jul. 2019
KS1910	25 Oct. 2019–31 Oct. 2019
KS2008	23 Aug. 2020–3 Sep. 2020

2. Anatomical study of Tsushima Warm Current: Determination of principal pathways and its variation

2.1 Introduction

The Sea of Japan, a semi-closed marginal sea, is surrounded by continental Eurasia and the Japanese archipelago. Four shallow straits, i.e., the Tsushima, Tsugaru, Soya, and Mamiya Straits, connect this marginal sea to the Pacific Ocean, the East China Sea and the Sea of Okhotsk (Fig. 2-1).

The hydrographic properties in the upper layer of the Sea of Japan are principally influenced by the Tsushima Warm Current (TWC) (Fig. 2-1). The TWC originates from the Kuroshio and enters the Sea of Japan through the Tsushima Strait. According to earlier studies, the TWC system consists of three current branches (Suda and Hidaka, 1932). The coastal branch is believed to originate from the eastern channel (Japanese side) of the Tsushima Strait and to flow along the Japanese coast (Fig. 2-1) (Kawabe, 1982a, b). The offshore branch and the East Korean Warm Current originate from the western channel (Korean side) of the same strait. The former flows on the continental shelf. The continental shelf slope traps it along Japan's main island (Fig. 2-1). The latter flows northward along the Korean Peninsula and then bifurcates into two currents in the downstream. One flows eastward along the Subpolar Front (Fig. 2-1). Another one turns

around clockwise near Ulleung Island, thereafter, heading southward (Fig. 2-1) (Kato, 1994).

The Subpolar Front is spatially coincident with a near-surface temperature front that lies approximately on a zonal line of 40°N, which forms a southern boundary of the Subarctic Gyre in the Sea of Japan (Talley et al., 2006). Additionally, this front is known to outcrop to the surface during wintertime (Lee et al., 2006). The Subarctic Gyre, a basin-scale oceanic circulation, circulates broadly counterclockwise in the northern Sea of Japan. This gyre consists of the TWC, the Liman Current, the North Korean Cold Current (blue dashed arrows of Fig. 2-1), and the Subpolar Front (Senjyu, 1999; Morimoto and Yanagi, 2001).

Some debate persists about the existence of offshore branches among past studies. Kawabe (1982a) shows strong seasonality of its appearance, whereas Morimoto and Yanagi (2001) insist on the year-round appearance with little seasonal variation. It has been widely accepted that the remainder of branches of coastal current, the East Korean Warm Current and the Subpolar Front Current exist throughout a year (Kawabe, 1982a; Hase et al., 1999). One crucially important factor affecting the TWC system is the volume transport into the sea through the Tsushima Strait. According to Fukudome et al. (2010), transport through the western channel achieves its maximum amount during August–

October, whereas transport through the eastern channel reaches a maximum in March and August. Other factors affecting the TWC include the strength of eddy activity along the TWC system, making it more complex by causing multi-scale meanders and bifurcations (e.g. Isoda 1994; Hirose and Ostrovskii 2000; Watanabe et al. 2009).

Many studies have been conducted to clarify the TWC pathways. The existence of the three branches and their seasonality in the southwestern Sea of Japan have been detected based on hydrographic, satellite-tracked drifters, and satellite altimetry data (Kawabe, 1982a; Kato 1994; Lee and Niiler, 2010; Ito et al., 2014). Morimoto and Yanagi (2001) reported the monthly mean current based on altimetry data. Hase et al. (1999) deduced that the offshore branch spread widely from the central and the eastern Sea of Japan based on the horizontal distribution of 100-m-depth temperature. In addition, some studies have indicated that the TWC meanders widely as one pathway, with no bifurcations as independent branches (Naganuma, 1985; Kato 1994; Lee and Niiler, 2010). The relation between the meandering pathway and other three branches is not clear.

With respect to the eastern part of Sea of Japan, it seems that only scant attention has been devoted to the area in earlier studies. We are motivated strongly to redefine and reorganize the TWC system in the central and the eastern Sea of Japan by taking advantage of the elongated oceanographic dataset. Accumulated satellite-based altimetry

and distributed buoy data have contributed to an understanding of the long-term variability of those currents. For example, altimeter data are available today for the long period since 1993. This study uses 25 years of satellite-based altimetric data and hydrographic data obtained along the sections across the TWC.

This paper presents the analyses and their results in the following sections. In Section 2.2, the analyzed data are described. In the section, we also validate the altimetric data by comparison with hydrographical evidence obtained from *in situ* surveys. In Section 2.3, we propose a method to detect ocean currents from the altimetric dataset. In Section 2.4, satellite-detected pathways are interpreted from a statistical perspective. Section 2.5 presents discussion of the eddy development related to the meandering of different currents. In Section 2.6, the overall findings are summarized with concluding remarks.

2.2   Data

2.2.1   Satellite-based altimeter data

For the specific aims of detecting and evaluating oceanic currents, this study takes advantage of a satellite-based altimeter dataset, "Global Ocean Gridded L4 Sea Surface Heights and Derived Variables Reprocessed," which is distributed by the

Copernicus Marine Environment Monitoring Service (CMEMS, http://marine.copernicus.eu/ser-vices-portfolio/access-to-products/). The absolute dynamic topography (ADT), the ADT-based geostrophic velocity and sea level anomaly (SLA) obtained during multiple missions (e.g. TOPEX-Poseidon, Jason 1–3) are used in this study. These data prepared respectively as temporally and horizontally constant resolutions of daily and 0.25 degree (approximately 20 km) intervals. As described herein, the ADT data are analyzed for the period between January 1993 and December 2017. The eddy kinetic energy (EKE) is derived to examine the horizontal distribution of eddy activity. The EKE is a deviation from the monthly mean of the geostrophic velocity field over 25 years in each grid.

With respect to detection and tracking methods of mesoscale eddies, the Mesoscale Eddy Trajectory Atlas ver. 1.0 is adopted. The Centre National d'Etudes Spatiales/ Collecte Localisation Satellites (CNES/CLS) is responsible for the rights and public access, where the data are accessible via the data archive system of Archivage, Validation et Interprétation des données des Satellites Océanographiques (AVISO, https://www.aviso.altimetry.fr). Following the method presented by Chelton et al. (2011), local maxima and minima in terms of SLA are found respectively as anticyclonic and cyclonic eddies if the SLA amplitude exceeds 0.01 m. Information such as position, surface height displacement, rotational direction, and lifetime can be referred from the

data record compiled to daily resolution. We counted the days during which an eddy exists

in each 0.25-degree grid to examine areas where eddies occur frequently.

2.2.2 Mooring velocity

The ADT-based geostrophic current is compared with *in situ* currents from

mooring observations. Data were obtained through the research project of the Fisheries

Research Agency – Atmosphere and Ocean Research Institute Tsushima Warm Current

Observatory (FATO), as detailed by Kawaguchi et al. (2020). The mooring system was

deployed in a region off Sado Island (38.72°N, 137.83°E), marked by a cross in Fig. 2-1,

where the water depth is 1777 m. We use the horizontal current from an upward-looking

Acoustic Doppler Current Profiler (ADCP 75 kHz Workhorse; RDI Inc.), which was

installed at the top of the mooring and which measured horizontal velocities at depths of

54–334 m with vertical resolution of 8 m. For analyses, diurnal and semi-diurnal tides

were removed using a 48-hour tide killer filter as described in an earlier report (Hanawa

and Mitsudera, 1985).

2.2.3 Hydrographic data

ADT-based altimeter data show information obtained at the ocean surface. The

vertical structure of the TWC system was examined using data of the hydrographic survey.

The Japan Meteorological Agency (JMA) has publicly available data resources of

hydrographic surveys that are made regularly in the Sea of Japan (https: //www.data.jma.

go.jp/kaiyou/db/vessel_obs/data-report/html/ship/ship.php). For this study, we use their

high-resolution hydrographic data over the fixed observational line accommodated off

the Echizen Peninsula, which is designated as the 'PM' line (Fig. 2-12). Over the PM line,

surveys were conducted routinely at a scheduled frequency of four times a year (January,

April, June, and October) and were continued during 1997–2008. The nearly full depth

profiles of temperature and salinity were analyzed closely. For quality control of the data,

removal of spikes and data interpolation procedures were done by JMA (McTaggart et al.,

2010).

2.2.4　Validation of ADT-based currents

The resolution of the ADT-based current was 0.25° (approx. 20 km) in space.

The bottom topography and coastline are more complicated than the data resolution,

especially in the coastal area. We have compared the ADT-based data with *in situ* mooring

and repeated observation data. Details of the mooring data are presented in Section 2.2.2

The latter data are observed from shipboard ADCP mounted on the bottom hull of a

commercial ferry; regular collection of current velocity data was done at Tsushima Strait.

Fukudome et al. (2010) presents additional details. The available data period extends from

1997 through 2007.

According to the comparison, the temporal variations of ADT-based current data

and mooring data are mutually consistent (Fig. 2-2). The correlation coefficient between

the ADT-based current (u_g, v_g) and the moored current (u_{ADCP}, v_{ADCP}) at 50 m depth is 0.86

for the eastward velocity and 0.80 for the northward velocity. In addition, comparison of

the monthly average of the shipboard ADCP data shows reasonable mutual agreement

(Fig. 2-3). The correlation coefficients between the ADT current and direct observation

are 0.70 at the western channel and 0.35 at the eastern channel. The value in the eastern

channel is low, but both values are inferred as statistically significant above the 95%

confidence level. Irrespective of the reduced precision of ADT current, particularly in

coastal areas, the ADT-based current well reproduces the seasonal variation of water

transport, which is a key point for ascertaining the TWC system variation in most of the

Sea of Japan.

2.3   Satellite-based Current Tracking Method (STCM)

According to Qiu and Chen (2005), the Kuroshio Extension is tracked accurately

by an ADT contour coincident with a local maximum of the ADT gradient. Nakano et al. (2018) proposed a method to track multiple frontal jets in the northwestern Pacific Ocean. They used temporally variable values of the ADT to track the seasonal variation for each jet. For this study, some modifications have been made to apply the method to the TWC system in the Sea of Japan.

For this study, one can identify following particular branches based on the earlier studies (Suda and Hidaka, 1932; Kawabe, 1982a; Kato, 1994; Hase et al., 1999): Coastal Current (CC), Offshore South Current (OSC), Offshore North Current (ONC), and Subpolar Front Current (SFC) (Fig. 2-1). In the definition, the CC, OSC, and ONC can be regarded respectively as the first, second, and third branches of TWC in past studies. We separately defined the ONC and SFC because the East Korean Warm Current forms two distinct currents after leaving the Korean Peninsula to the east, as described earlier (Fig. 2-1) (Kato, 1994; Ito et al., 2014).

The TWC tracks and eddies in the Sea of Japan are assumed to be in geostrophic balance, such that short-term variation like diurnal oscillation can be ignored. Isoda (1994) reported that the propagation speed of mesoscale eddies is less than 0.1 m s^{-1} in the eastern Sea of Japan. Regarding determination of TWC pathway, his study implies that the daily or shorter than daily variations can be negligible. For detailed analyses, we

prepare a monthly average of ADT and consequent velocity based on the original daily

database. The geostrophic balance is written as

$$f u_g = -g \frac{\partial \eta}{\partial y}, \quad (1a)$$

$$f v_g = g \frac{\partial \eta}{\partial x}, \quad (1b)$$

where x and y respectively represent the eastward and northward axes, u_g and v_g

respectively denote the x and y components of geostrophic velocity, f is the Coriolis

parameter, g represents the acceleration of gravity, and η signifies the ADT (Gill, 1982).

For this reason, the isolines of ADT can be assumed to yield non-divergent two-

dimensional motions near the surface level.

Detailed processes for the algorithm are described next. In Step 1, all isolines on

the monthly mean ADT field are traced at an interval of 0.01 m (Fig. 2-4). Matrix of

geographic position (latitude, longitude) is created for each ADT isoline using the

"contour" Matlab tool. Horizontal resolution of the matrix is approximately 20 km.

Velocities at all coordinates in the matrix are horizontally interpolated using the ADT-

base geostrophic velocity, for which the resolution is 0.25 degrees.

In Step 2, the mean current magnitude and total path length for each ADT isoline

are derived from the velocity, latitude, and longitude data. Figure 2-5a displays the

example for July 2006. We specifically examined isolines with the strong current

magnitude and the sufficiently long path length. The criterion for the current magnitude is set as 0.15 m s^{-1}, whereas that for the path length is set as 500 km. The criterion is determined using the mean current magnitude at each ADT isoline for a total of 300 months (e.g., Fig. 2-5a). The distance between the Tsushima Strait and the Oki Island is approximately 500 km. This procedure is applied to define all four branches, and to define the isoline travel through Oki Island.

In Step 3, we classify these ADT isolines into four kinds of TWC branches based on certain conditions: their origins, directions and routes (Fig. 2-4). Those currents are determined according to the following rules based on ADT. As described in the earlier section, pathways of these four currents are topographically trapped in the southwestern area. The CC, OSC, and ONC streamlines emanate from the Tsushima Strait, whereas the SFC originate in other areas (Step 3–1 in Fig. 2-4). The CC passes through the eastern channel, whereas the OSC and the ONC goes through the western channel (Step 3–2). The current forms two currents after passage through the western channel (Step 3–3). The OSC flows along the continental shelf adjacent to Japan, heading nearly due east (Fig. 2-1). By contrast, the ONC is presumed to direct northward and travel along the Korean Peninsula (Fig. 2-1). Specifically, the OSC must not cross the ad hoc latitude of 36°N to the north in longitudes between 130°E and 131°E, whereas the ONC crosses this latitude

to the north. Regarding the SFC branch, we pick up isolines for which the mean latitude is 38.5°N – 41°N (Step 3–4). The mean latitudes of SFC isolines are estimated to have longitudes of 131°E to 138°E.

In Step 4, we finally determine one isoline as representative of each TWC branch. In the steps used up to this point, multiple candidates exist for TWC isolines. The isoline nearest to the median value is determined as the pathway representing each pathway. The median ADT is calculated those among the candidates. It is noteworthy that no pathway is determined for the OSC and ONC if the number of candidates is inadequate i.e. less than three. One example for the traced pathways in July 2006 is depicted in Fig. 2-5b.

It is generally accepted that the definition of the pathway is approximately consistent with the one suggested by peaks of current magnitude, representing a jet structure. We examined the correlation between the latitude of the defined pathway (hereinafter streamline-based latitude) and the latitude of the current magnitude peak (hereinafter peak-based latitude) to validate the method. The spatial relevance was assessed at three longitudes of 132°E, 135°E, and 138°E in the southern part of the sea. The streamline-based latitude and the peak-based latitude exhibit a significant positive correlation for the four TWC branches at all longitudes. The data number and root mean square differences (rmsd) between the streamline-based latitude and the peak-based

latitude are presented in Table 2-1. The rmsd horizontal scale for OSC, SFC, and CC is

as large as the limitation of ADT grids, i.e. 0.25 degree, whereas that for ONC is just a bit

smaller than the limit. We therefore assume that the method has sufficient accuracy to

define the TWC pathways in the Sea of Japan.

2.4   Results

2.4.1   Statistics

The ADT-based current tracking sheds light on a well-drawn picture of the TWC

system, which flows in the Sea of Japan. Figure 2-6 presents an example of monthly

pathways for 1999 for the four defined currents: CC, OSC, ONC, and SFC. These currents

are perceived independently in regions west of the 133°E line. However, it shows more

complex, tangled features in more downstream regions in the direction of the Tsugaru and

Soya Strait.

Statistically, the detection is successful at the respective percentages of CC, OSC,

ONC, and SFC: 43 ± 18, 64 ± 13, 88 ± 9, and $95 \pm 5\%$, where the standard deviation

denotes the month-by-month variation. Figures indicate that the ONC and SFC

appearance is stably perceptible throughout a year. However, the OSC rate is the highest

in July (92%) and lowest in November (32%). Ito et al. (2014) reported that the OSC

stably exists throughout a year except for November. The seasonal variation in detection

rate for OSC corresponds well to the result in their study.

Based on the data, month-by-month variation of current magnitude and volume

transport for each branch can be reported (Fig. 2-7). According to the figure, the ONC

tends to be strongest in current magnitude throughout a year. The monthly mean is

minimal in March; then it elevates in fall months, reaching its greatest value of 0.31 m s^{-1} in September. According to Fukudome et al. (2010), the volume transport through the

western channel of the Tsushima Strait becomes maximal in October (Fig. 2-7a). Seasonal

variation of the current magnitude roughly corresponds to that of the volume transport

through this channel. Isobe (1997) also indicates that the ONC's transport reaches its

largest value in summer. Volume transport through the eastern channel reaches the

maximum in March and August (Fig. 2-7a). The CC becomes maximum in August (Fig.

2-7b), which can be confirmed by the volume transport through the eastern channel.

2.4.2 Mean routes and their deviations

This subsection presents the occurrence frequency for each current on the map.

The frequency is counted as the ratio of months of pathways detected to the entire period

of time, i.e. 300 months. Herein, we present results obtained for winter months (December,

January, and February) and summer months (June, July, and August). For this, we particularly examine the clear difference in the routes of TWC pathways between winter and summer. It is emphasized here the volume transport through the Tsushima Strait strongly affects the results of TWC routes in downstream regions (Fig. 2-7a). Water masses entering the sea through the strait take several months to reach the exit. Therefore, the pathway in winter is influenced by the water masses entering in autumn.

The TWC pathways are also influenced by stratification, as well as volume transport. According to Isobe (1997), the volume of the Eastern Korean Warm Current reaches a maximum value in summer because of the stratification formed by the bottom cold water in the western channel.

1) OSC

The OSC shows a stable pathway in the western region of the Sea of Japan, where the OSC flows along the Japanese coast to the north of the Oki Islands (Figs. 2-8a and 8c). The pathways on the line A (132°E) show a high frequency around 35.5°N, which is overlapped with the shelf slope near a 200-m isobath (Fig. 2-8).

In the central Sea of Japan between the Oki Islands and the Noto Peninsula, pathways differ among seasons. The OSC flows northeastward from the Oki Islands to

the south of the Yamato Rise in winter, whereas it flows along the continental shelf in summer (Figs. 2-8a and 2-8c). For the central region at the line B (135°E), the frequency peaks are present at around 38°N for winter, but approximately 36°N for summer (Figs. 2-8b and 2-8d). Both pathways for summer and winter, i.e. respectively onshore and offshore, show a consistent way point off the Noto Peninsula around 38°N (line C in Figs. 2-8b and 2-8d).

Related to the points above, Watanabe et al. (2009) presented a detailed discussion of TWC bifurcation around the Yamato Basin based on data from surface drifting buoys. They demonstrated the dependence of the pathway on the presence of local eddies. Hirose and Ostrovskii (2000) clarified that the eddy oscillates quasi-biennially in the same basin. The relation between OSC/ONC paths and the eddies is addressed further in Section 2.5.

2) ONC

According to Fig. 2-9, the ONC frequency is distributed widely from the shelf slope to the north of 39°N in the range of 130–136°E (Figs. 2-9a and 2-9c). This result implies meandering pathways in both seasons.

The maximum frequency of ONC exists around 38°N in both seasons on the

meridional line B (135°E, Figs. 2-9b and 2-9d) and flows northeastward from the Oki

Island to the Yamato Rise. The frequency drops to almost zero at the south of the Yamato

Rise in winter, where the bottom relief shoals up to approximately 230 m. The TWC jet

is regarded as roughly 200 m thick or thicker, such that the shoals of Yamato Rise are

expected to affect the ONC strongly. At line B, the secondary peak for the ONC is found

around 36.5°N only for summer (Fig. 2-9d). This finding implies that the seasonal current

extends along the continental shelf slope in parallel with the coastal branch of OSC (Fig.

2-8c).

In the eastern domain (i.e. east of 136°E), the ONC paths show a slight difference

on the way to the Tsugaru Strait among different seasons: smaller meanders in winter and

nearly straight paths in summer (Figs. 2-9a and 2-9c). The frequency in winter is high at

the offshore side of the climatological pathway (line C in Fig. 2-9b), whereas it is

concentrated at the coastal side of the pathway in summer (line C in Fig. 2-9d).

In the easternmost region, most of the ONC streamlines enter the Tsugaru Strait

(Fig. 2-9). Statistically speaking, 87% of overall isolines connect to this strait.

Consequently, the Tsugaru Strait can be regarded as the main exit for the ONC waters.

3) SFC

Next, the SFC results are presented (Fig. 2-10). The figure shows that the SFC are broadly present between 130–140°E (Figs. 2-10a and 2-10c), apparently along the southern boundary of the Japan Basin.

On line B (135°E), the frequency peak exists at approximately 39°N latitude in winter and 39.5°N in summer (Figs. 2-10b and 2-10d). The frequency distribution shows a rapid decrease at the northern side where it immediately faces the Yamato Rise. In the southern Japan Basin, the Yamato Rise extends east–west, separating the deep basin into two parts. Its minimum depth is about 230 m, which is approximately same depth as the bottom of TWC water. It is noteworthy that the SFC is affected strongly by topographic features (Fig. 2-10), similarly to the ONC (Fig. 2-9).

Statistically speaking, roughly 83% of the entire SFC paths detected goes along the Hokkaido Island, whereas the rest of the SFC enters the Tsugaru Strait (16%). Seasonal variation is negligible. We assume that most of the SFC waters exit through the Soya Strait, located around 46°N, and enters the Sea of Okhotsk, although the exact isolines are not identifiable by the present ADT technique because of the reduced accuracy near the coast, as presented in the discussions for CC. In addition, the remaining SFC waters are assumed to travel further north as a part of the Subarctic Gyre.

4) CC

The image depicted in Fig. 2-6 shows that most detected CC paths cross Japan's coastline and terminate its further tracking. Consequently, the occurrence frequency for CC decreases drastically in regions east of the Oki Islands (Fig. 2-11). The CC travelling in the coastal area cannot be examined sufficiently by the ADT-based method because of the reduced accuracy.

Watanabe et al. (2006, 2009) used cross jet hydrographic data and the surface drifter buoys to show that the CC's pathway continues along the Japanese coastline. We consider the coverage of the lack of gridded-data in the downstream region for CC by direct tracking of the current with drifting buoys. In July 2019, six sets of Iridium satellite-tracked drifters are deployed in the central Sea of Japan. Those possess a holey-sock drogue under the water, which is designed to evaluate the water movement efficiently at 30 m depth (Lee and Niiler, 2010; Thomson and Emery, 2014). Figure 2-11 exhibits similar trajectories along which the buoys moved in parallel to the west coast of Japan's main island. These trajectories suggest the existence of a northern extension of CC branch toward the Tsugaru Strait after it passes off the Noto Peninsula. Some questions related to additional details such as its variation and uncertainties are expected to be resolved based on results of future studies.

2.5   Discussion

2.5.1   Influences of mesoscale eddies in the Yamato Basin

As described in the earlier section, two pathways exist around the Yamato Basin

for the OSC (Figs. 2-8a and 2-8c) and the ONC (Figs. 2-9a and 2-9c). These pathways

have already been reported as the offshore route and the coastal route by Watanabe et al.

(2009). Their study demonstrated that the transition of these routes is influenced by any

interannual variation of eddies. The interannual variation of pathways in this study

similarly exists as their study, but the seasonal variation is as large as the interannual one.

The seasonal transition of OSC/ONC related to the eddy existence has not been described

to date in any study. Therefore, this section addresses interaction between TWC and

mesoscale eddies around the Yamato Basin in greater detail.

Figure 2-12 depicts the mean EKE over 25 years and the number of eddies over

23 years. Details of the eddy detection technique are presented in Section 2.2.1. The EKE

is high around Ulleung Island, the Yamato Basin, and the offshore area of Sado Islands

(39°N, 138°E), where the eddies are frequently distributed. These results were shown by

the root mean square of the temporal variation of SSH (Morimoto et al., 2000), describing

the nonseasonal component of SSH as the first mode of empirical orthogonal functions.

The ONC meanders around these three areas (Figs. 2-9a and 2-9c). Accordingly, a relation

is suggested between the eddy distribution and the meandering.

The effect of eddies on the TWC pathways is examined using the hydrography

along the PM line, which crosses the Yamato Basin (Fig. 2-12). Figure 2-13 shows the

vertical section of temperature, salinity and geostrophic current with potential density in

January 2007 and June 2004. The warm and saline TWC water is distributed from the

surface to about 200 m depth. A strong pycnocline exists around 40 m in June because of

the distribution of the low-salinity water (Fig. 2-13b). According to Isobe et al. (2002),

the Chang Jiang River is the most important source of freshwater for the Sea of Japan.

The warm eddy exists around 37.2°N in January and 38°N in June, as judged from the

depressed pycnocline. In addition, the temperature is higher than in the surrounding area.

Lower panels in Fig. 2-13 present the geostrophic velocity across the PM line as referring

to 500 dbar. The eastward and northeastward jet over 0.3 m s^{-1} is around 38°N in January,

around 37.3°N and 38.5°N in June. This result is consistent with the seasonal transition

of the OSC and the ONC in the Yamato Basin (line B in Figs. 2-8 and 2-9). The lower

panel in Fig. 2-13a shows the jet structure of the SFC in the north of 39°N in January,

which is not clear in June. The possibility exists of a northward shift of the SFC in summer

and in autumn. Park et al. (2007) reported the seasonal variation of the Subpolar Front

using the gradient of sea surface temperature in a latitudinal direction. They show that the

front moves northward in summer. In this case, the PM line is out of range for detecting

the SFC.

Next, we discuss the horizontal location of anticyclonic and cyclonic eddies to

clarify the seasonal TWC pathways. Figures 2-14 show the monthly climatology of ADT

and relative vorticity in October, January, April, and July. Anticyclonic eddies develop in

October and in January to the east of Oki Island (Figs. 2-14a and 2-14b). A cyclonic eddy

develops between the Oki Island and the Noto Peninsula in July (Fig. 2-14d). The

anticyclonic eddies in October and in January form the northeastward flow to the east of

the Oki Island. Therefore the OSC takes the offshore route (Figs. 2-14a and 2-14b). The

cyclonic eddy in July forms the southeastward flow to the east of the Oki Island, so that

the OSC takes a coastal route (Fig. 2-14d). The ONC, in contrast, shows the offshore

route throughout a year. The passage latitude of ONC moves northward in October, which

reflects the development of the anticyclonic eddy in autumn and the northward shift of

this eddy (Fig. 2-14a). It is likely that the seasonal variation for the choice of the current

route in the Yamato Basin is explainable based on the geographical positions of eddies.

2.5.2   Meandering of TWC branches and SFC pathways

As presented in Fig. 2-12, the meandering pathway occurs particularly when the eddies grow simultaneously in the three areas: Ulleung Island, the Yamato Basin, and off the Sado Islands. To observe the eddies in these areas throughout a year, Fig. 2-15a shows a Hovmöller diagram of SLA during 2003–2008. Its position is the central latitude of the ONC (Fig. 2-12). For example, the mean latitudes of the ONC on longitudinal line B are 38.0°N in winter and 37.8°N in summer. Factors affecting the eddy movement are not only the background velocity, but also the westward propagation velocity of planetary Rossby waves C_R. The C_R is defined as $-\frac{\beta}{\lambda_i^2}$ with the internal Rossby deformation radius $\lambda_i = \frac{\sqrt{gh_1(\rho_2-\rho_1)/\rho_1}}{f}$, where g represents the acceleration of gravity, f is the Coriolis parameter, $\beta = 1.8 \times 10^{-11}$ m^{-1} s^{-1} denotes the latitudinal gradient of the Coriolis parameter, $\rho_1 = 1025–1027$ kg m^{-3} signifies the density of the upper layer, $\rho_2 = 1029$ kg m^{-3} stands for the density of the lower layer, and $h_1 = 150–200$ m denotes the upper layer thickness. These values are chosen based on the result from the hydrography on the PM line in each month (Fig. 2-13). The resulting yearly mean phase speed of C_R is 0.01 m s^{-1}.

The SLA shows clear seasonal variation, which is high in autumn and low in spring. The high SLA around the Ulleung Island and in the Yamato Basin appears repeatedly and always in the same position, whereas that on Sado Island varies year by year. Characteristics of these eddies have been clarified already by Isoda (1994). The

period during which SLA becomes high in all three areas is limited from late 2006 through 2007. We suggest that the meandering pathway of the TWC develops in autumn and in winter. In addition, the temporal variation of SLA at the Yamato Basin is not only the seasonal development of anti-cyclonic eddy but also suggests reflecting the northward/southward shift of the eddy as described in the preceding subsection (Fig. 2-14).

The eddy movements are inferred to account for the current strength of the TWC because the eastward or northeastward movement of eddies are detected eastward of the Yamato Basin (Fig. 2-15a). The time series of the mean current magnitude along the ONC is presented in Fig. 2-15b. Whereas eddies propagate westward in the North Pacific based on the westward propagation velocity of planetary Rossby waves (Qiu et al., 2007), those in the Sea of Japan show complex features. The high SLA to the east of the Yamato Basin and at Sado Island show eastward movement when the current magnitude of the ONC exceeds approximately 0.3 m s^{-1}. The propagation speeds of eddies a and b (black dashed line of Fig. 2-15a) are, respectively, 0.005 m s^{-1} and 0.02 m s^{-1}. The ONC velocity and migration speed of eddies are of a different order of magnitude. Eddies move separately with the ONC, but it is plausible that the current forces the eddy movement.

Figure 2-16 shows the monthly ONC pathways from July through December in

2003 and 2006. These two years show different eddy movements around Sado Island. An anti-cyclonic eddy remained approximately in the same area in 2003, but an eddy showed a faster northeastward movement in 2006 (Fig. 2-15a). The monthly evolution of ONC pathways can track these eddy migrations (Fig. 2-16). The migration speed of meandering ONC track can probably be found as a result of competition between the westward propagation by the planetary wave and the northeastward advection by TWC (e.g. Morie et al. 2015).

According to Fig. 2-15, the anticyclonic eddies develop when the current magnitudes of the TWC strengthen. The eddies serve an important role in the establishment of the meandering pathway. Actually, it remains unclear which come first: jets or eddies. This subject is beyond the scope of this paper and limitations imposed by the available altimetric data.

2.6   Summary

The TWC system shows complex figures of water current throughout the entire Sea of Japan region. This study was conducted to elucidate those patterns by defining and tracking the major currents in the TWC system (CC, OSC, ONC, and SFC) based on monthly ADT data for 1993–2017.

A schematic map of the TWC system including the central and the eastern Sea of Japan based on this study is depicted in Fig. 2-17. By tracking specific ADT isolines, we obtained results elucidating the meandering pathways and the nature of each current (Fig. 2-1). According to these analyses, the ONC is the strongest current magnitude among the four major currents throughout the year (Fig. 2-7). The ONC notably shows meandering features throughout the year (Fig. 2-17). The SFC turns out to flow eastward around the roughly constant latitude of 40°N with negligible seasonal variation (Fig. 2-17). The major part of the SFC stream heads northward along Hokkaido Island. Results also suggest that the SFC exits through the Soya Strait, whereas the remaining water joins the Subarctic Gyre in the northern Sea of Japan.

The OSC shows a stable pathway with flow along the shelf slope, reaching the west of the Oki Islands (Fig. 2-8). Subsequently, this flow indicates two routes around the Yamato Basin: an onshore route along the shelf slope and an offshore route towards the Yamato Rise (Fig. 2-17). When a well-developed warm-core eddy is present around the west of Yamato Basin, the OSC tends to take the offshore route. However, in the presence of a cyclonic eddy south of the same basin, the OSC tends to take the onshore route. This finding then appears to explain the seasonal difference in the choice of OSC paths, i.e., between summer and winter months. After all, the OSC currents are confluent at the north

of the Noto Peninsula.

This study prioritizes elucidation of complications related to issues of TWC determination using statistical methods based on long-term satellite data. Consequently, some fundamental questions related to dynamical problems, e.g. formation of mesoscale eddies and the hydrographical difference among TWC branches, remain unresolved. These issues should be clarified through future research efforts.
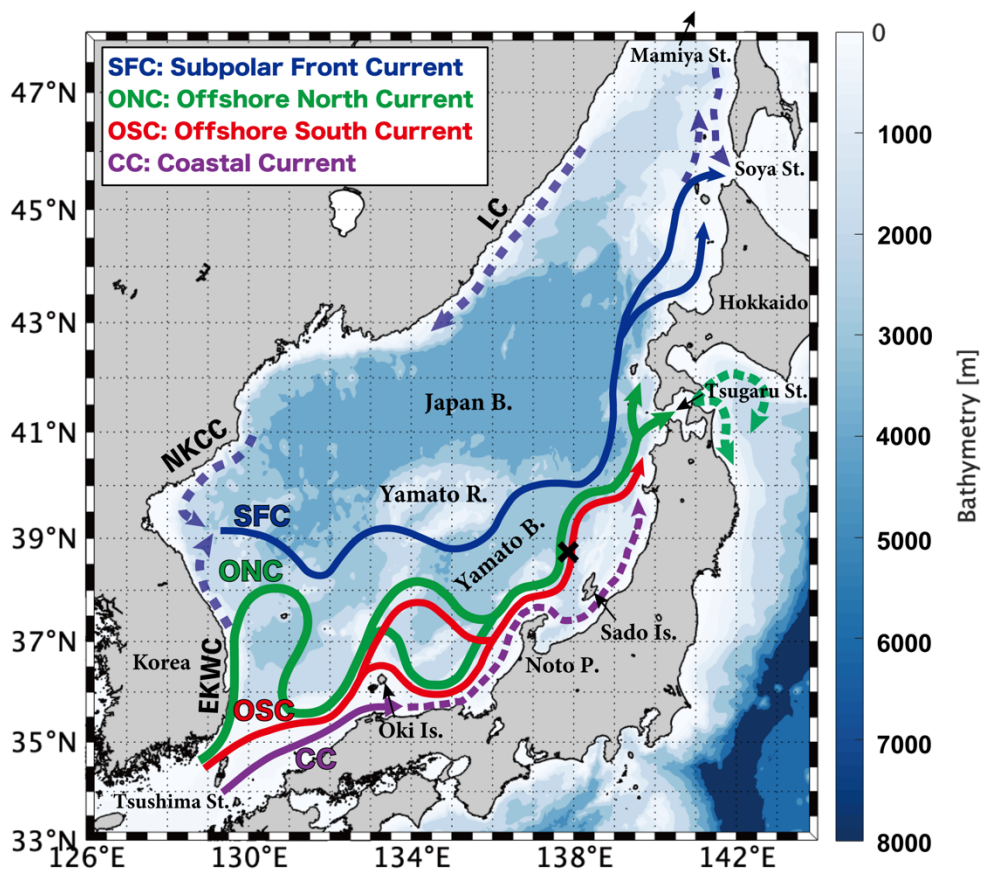
Fig.2-1: Schematic map showing the TWC system on this study. Specific geographical names in the Sea of Japan study domain. Colored solid arrows indicate the pathways emphasized for this study. Blue shading represents bathymetric contours. Abbreviations for current names are the following: EKWC, East Korean Warm Current; NKCC, North Korean Cold Current; and LC, Liman Current. The black cross mark denotes the positions of FATO where the mooring measurements conducted.
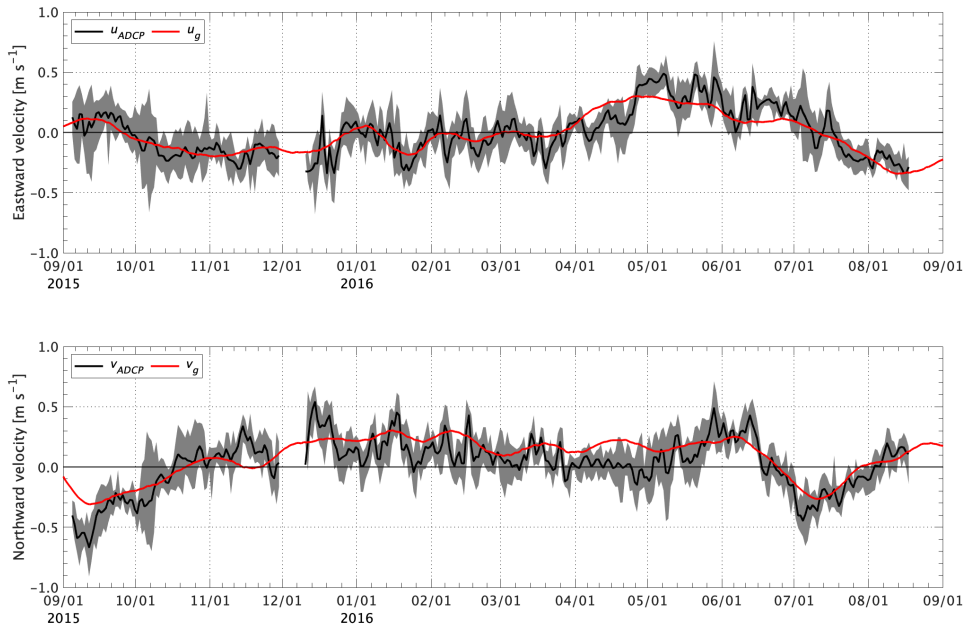
Fig.2-2: Time series of eastward (upper) and northward (lower) velocity at the FATO site. Red lines and black lines respectively show velocities of ADT-based geostrophic current (u_g, v_g) and measured current velocities (u_ADCP, v_ADCP) at 50 m depth using upward ADCP. Tidal signals are removed by a 48-hour tide-killer filter presented by Hanawa and Mitsudera (1985). Gray shading shows the daily range of (u_ADCP, v_ADCP).
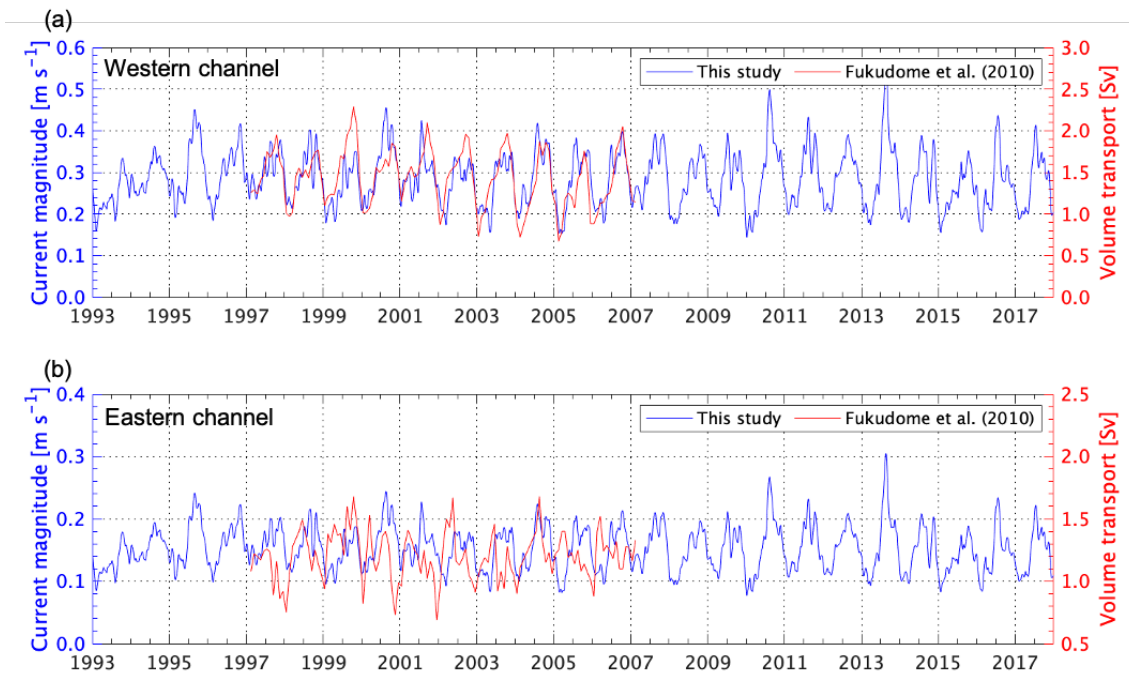
Fig.2-3: Time series of the current magnitude entering through the (a) western channel and (b) eastern channel of the Tsushima Strait during 1993–2017. A blue curve represents the value from the ADT-based geostrophic current, whereas a red one denotes the volume transport (Sv) from the direct current measurement of vessel-mounted ADCP (Fukudome et al., 2010).

Step 1	Pickup ADT isolines at an interval of 0.01 m	All isolines in the Sea of Japan
Step 2	Select isolines based on: ・mean velocity U along isoline ・total length L	$U \geqq 0.15$ m s^{-1} and $L \geqq 500$ km
Step 3	Define the TWC branches	
Step 3-1	Isolines path through the Tsushima Strait	Tsushima Strait / Other
Step 3-2	Isolines path through the eastern channel or the western channel	Eastern Channel / Western Channel
Step 3-3	Isolines direction after the passage from the western channel	Eastward / Northtward
Step 3-4	Check mean latitude ψ between 131°E and 138°E	$38.5°$ N $\leqq \psi \leqq 41°$ N
Step 4	Select one isoline among the candidates of pathways	Median ADT among isolines

CC   OSC   ONC   SFC

Fig.2-4: The flow chart of the ADT based method to track multiple frontal jets in the Sea of Japan.

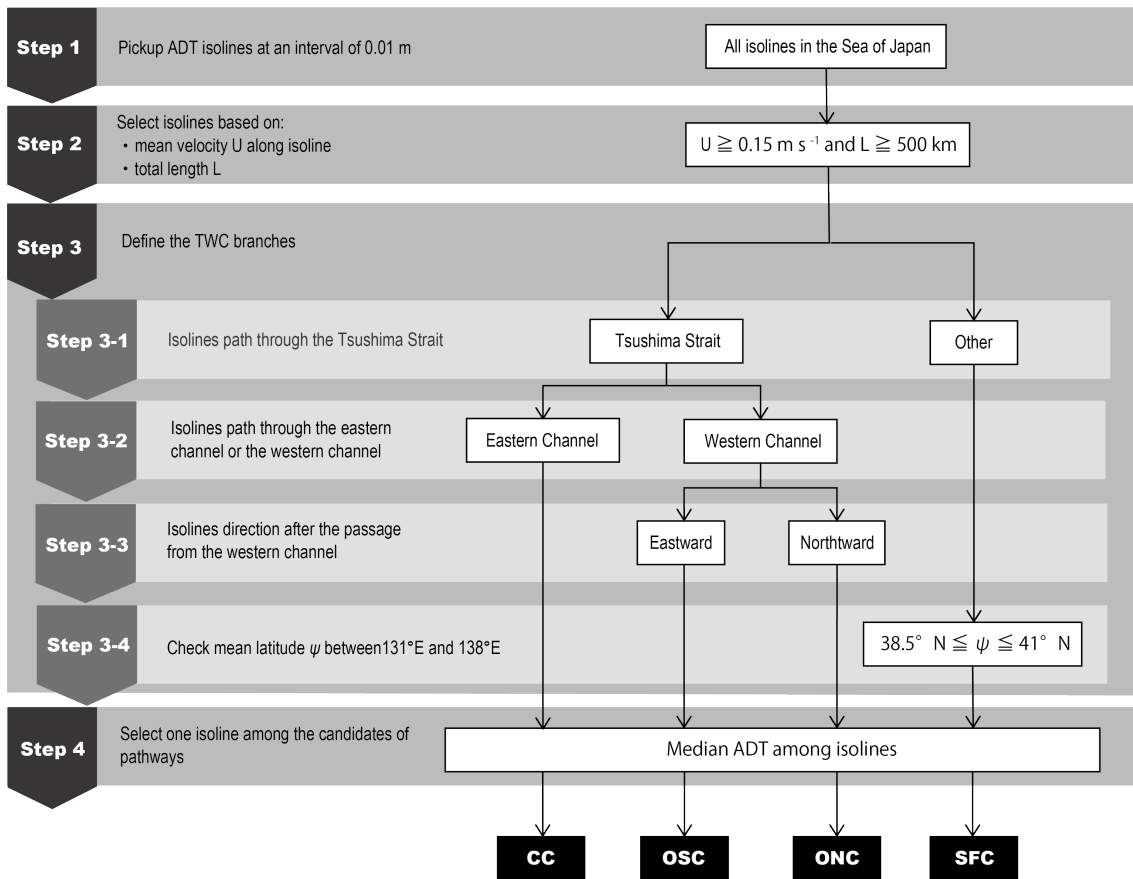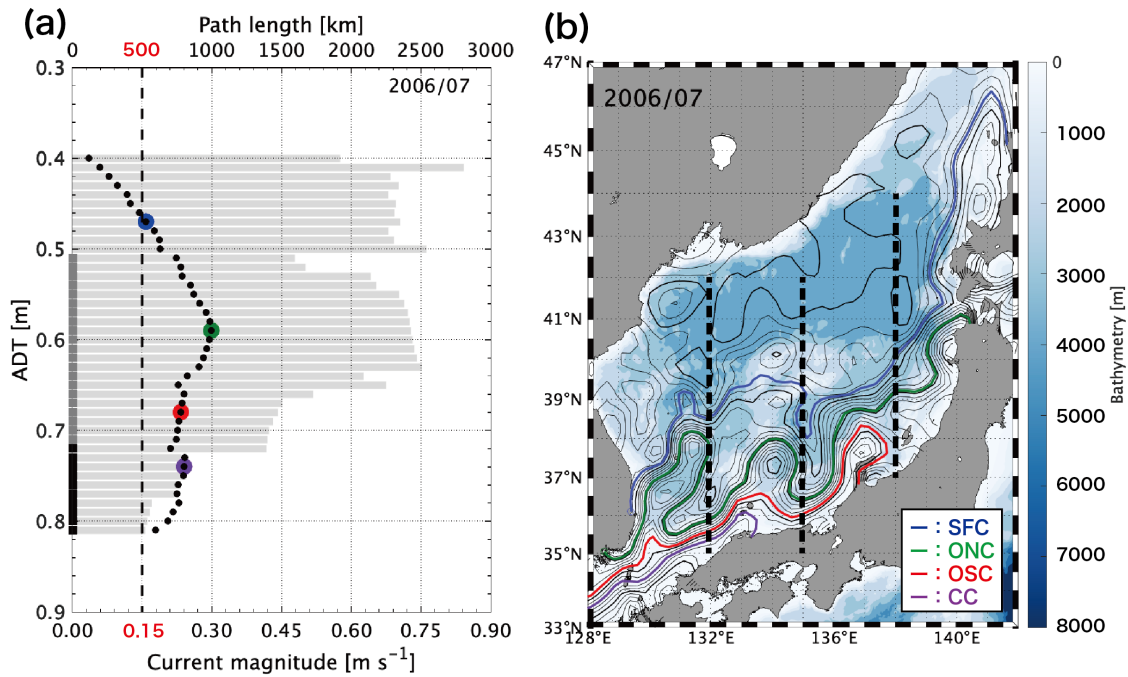Fig.2-5: (a) Mean geostrophic current magnitude along the isoline of ADT (black circle), and gray bars show the total path length of each ADT isoline at an interval of 0.01 m in July 2006. Purple, red, green and blue marks respectively show the ADT values selected as the pathways of CC, OSC, ONC and SFC. The ADT ranges marked by the black and gray areas on left axis respectively indicate the isoline passes through the eastern channel (EC) and the western channel (WC). (b) Monthly mean ADT map (black isolines) in July 2006. Purple, red, green and blue lines respectively show the selected pathways of CC, OSC, ONC and SFC. Color shade shows the bathymetry. Black dashed lines indicate the position on the validation of algorithm (Table 2-1).
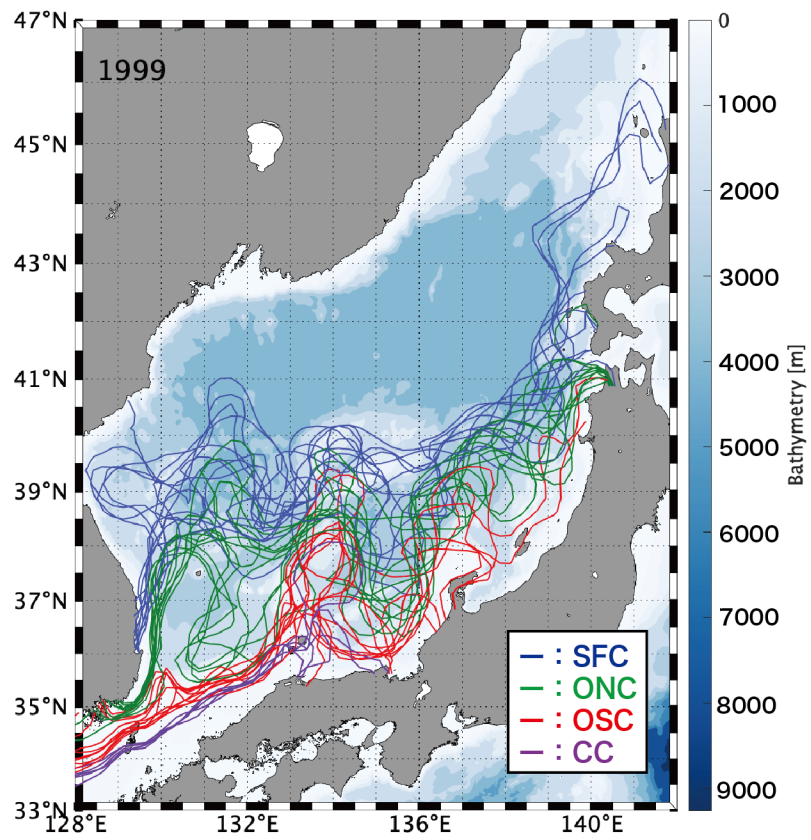
Fig.2-6: Monthly pathways of the four main currents in 1999. Purple, red, green, and blue curves respectively show the CC, OSC, ONC, and SFC. Color shade shows the bathymetry.

(a)

(b)
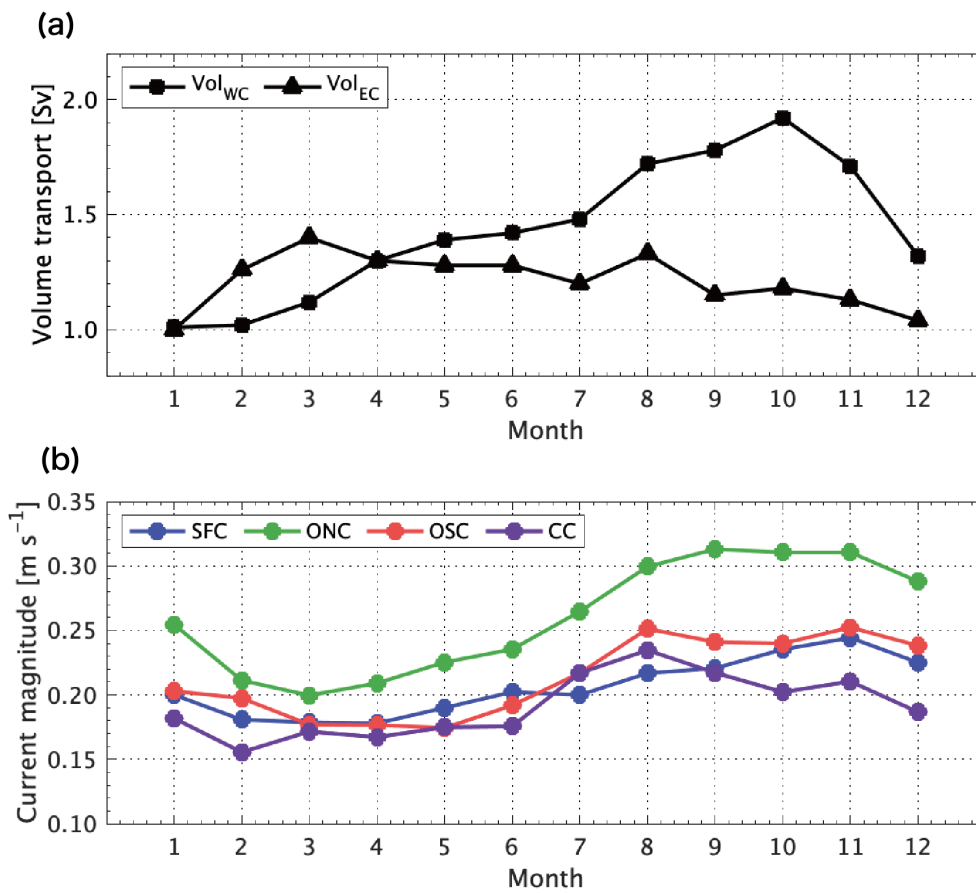
Fig.2-7: (a) The monthly mean volume transport values through the Tsushima Strait estimated by Fukudome et al. (2010). Black squares and triangles respectively show the values through the western channel (Vol_{WC}) and the eastern channel (Vol_{EC}) of Tsushima Strait. The monthly mean volume is averaged from February 1997 through February 2007. (b) Monthly mean current magnitude along the pathway averaged over 25 years. Purple, red, green, and blue circles respectively portray the current magnitudes of the CC, OSC, ONC, and SFC.
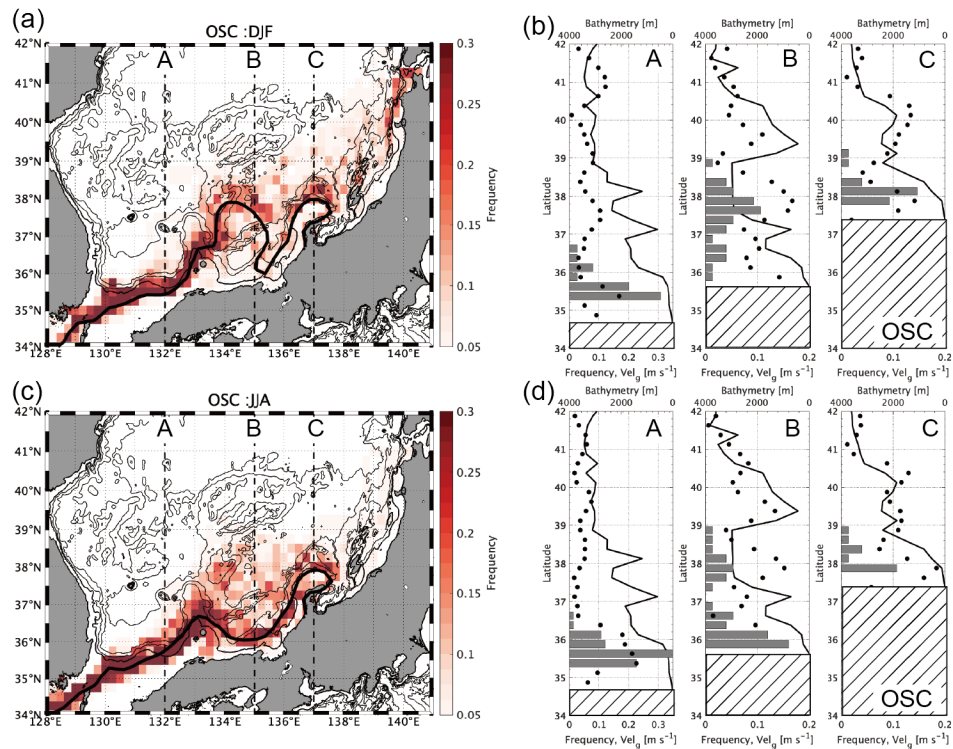
Fig.2-8: Horizontal distribution of occurrence frequency of the OSC in (a) winter (December, January, February; DJF) and (c) summer (June, July, August; JJA), as counted at 0.25° grid points over the full record of the dataset. Bold black curves show the pathways defined by the monthly climatology of ADT in (a) December and (c) July. Contours respectively show bathymetry of 200 m, 500 m, 1000 m, 2000 m, and 3000 m. The occurrence frequency of the OSC is shown along the 132°E, 135°E, and 137°E in (b) winter and (d) summer. The positions are shown as the dotted line in the left panels. Black circles and bold black lines respectively show the geostrophic velocity and the bathymetry along each longitudinal line, and hatched areas indicate onshore.
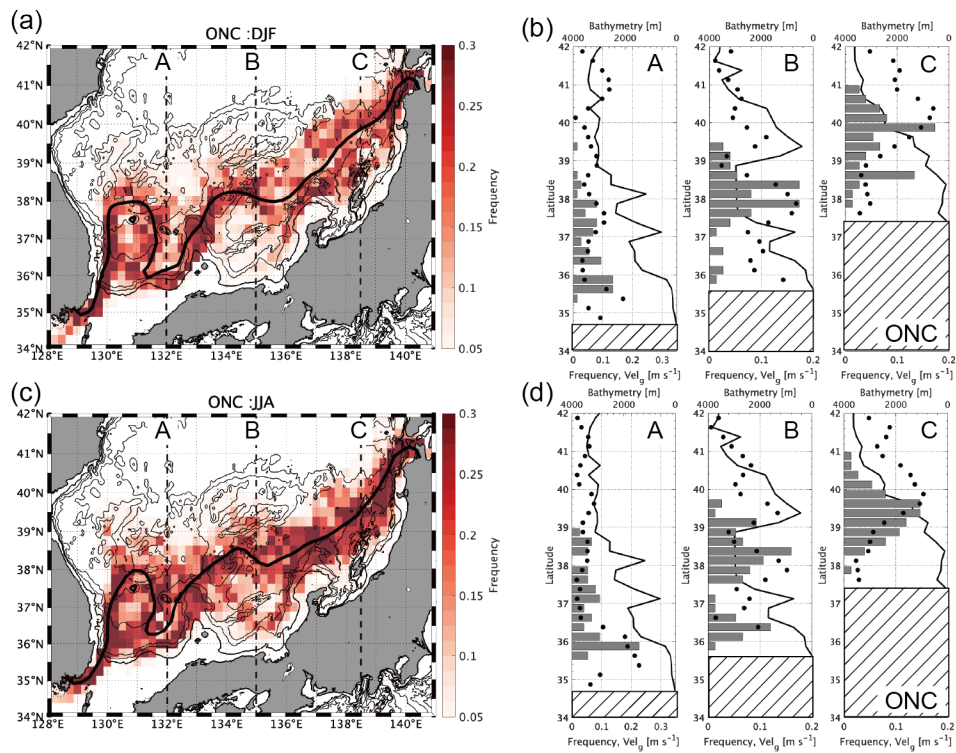
Fig.2-9: Same as Fig. 2-8, except for the ONC.
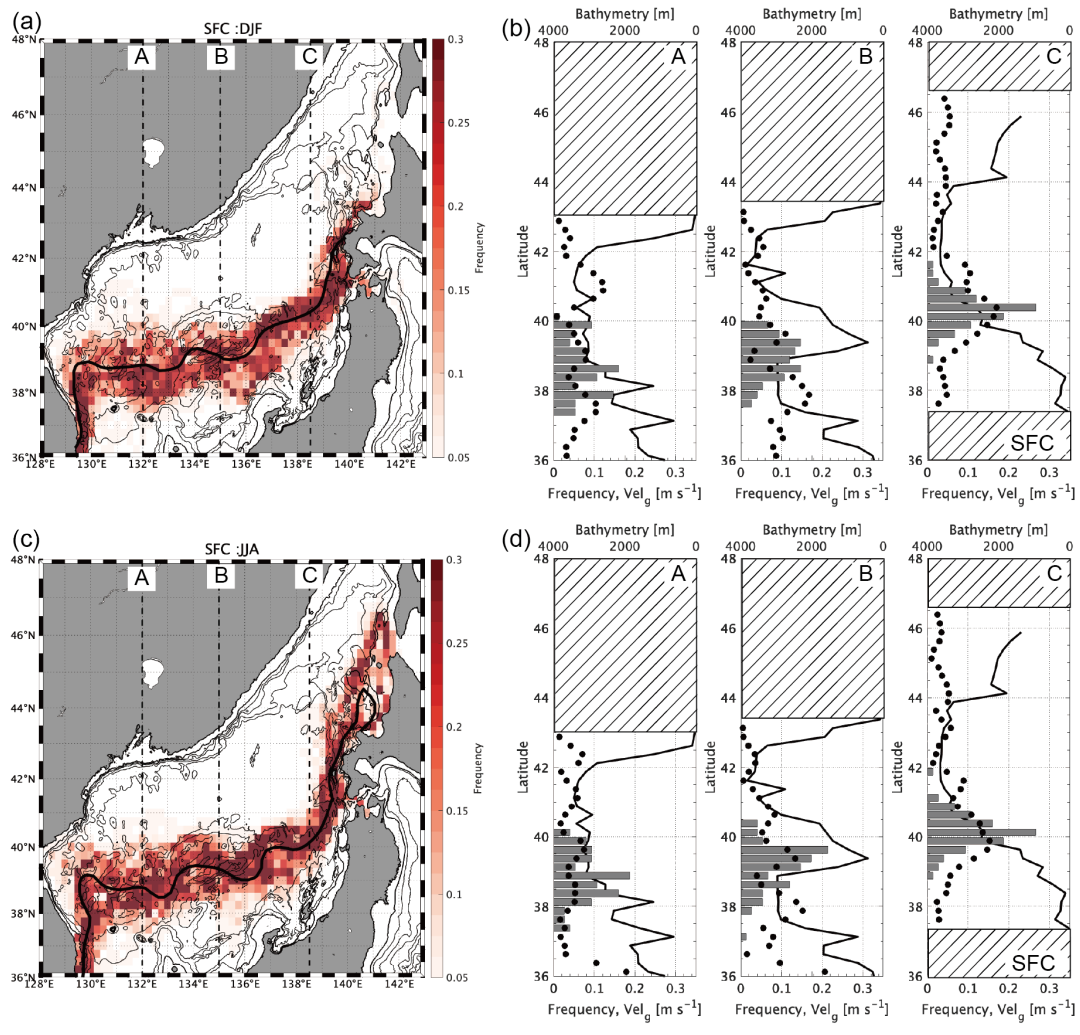
Fig.2-10: Same as Fig. 2-8, except for the SFC.
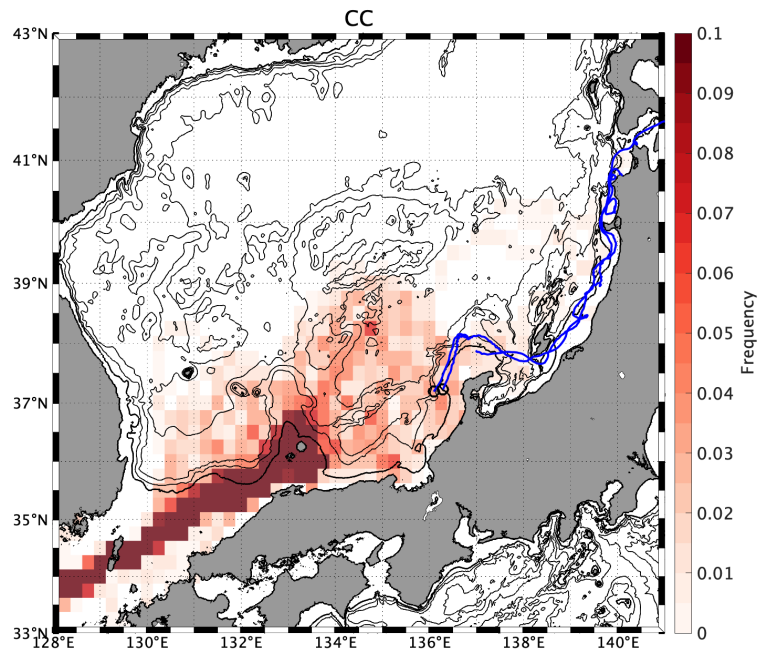
Fig.2-11: Horizontal distribution of accumulated occurrence frequency of the CC, as counted at 0.25° grid points over the full record of the dataset. Contours respectively show bathymetry of 200 m, 500 m, 1000 m, 2000 m, and 3000 m. Blue thick lines show trajectories of the Iridium satellite-tracked drifter deployed in July 2019.
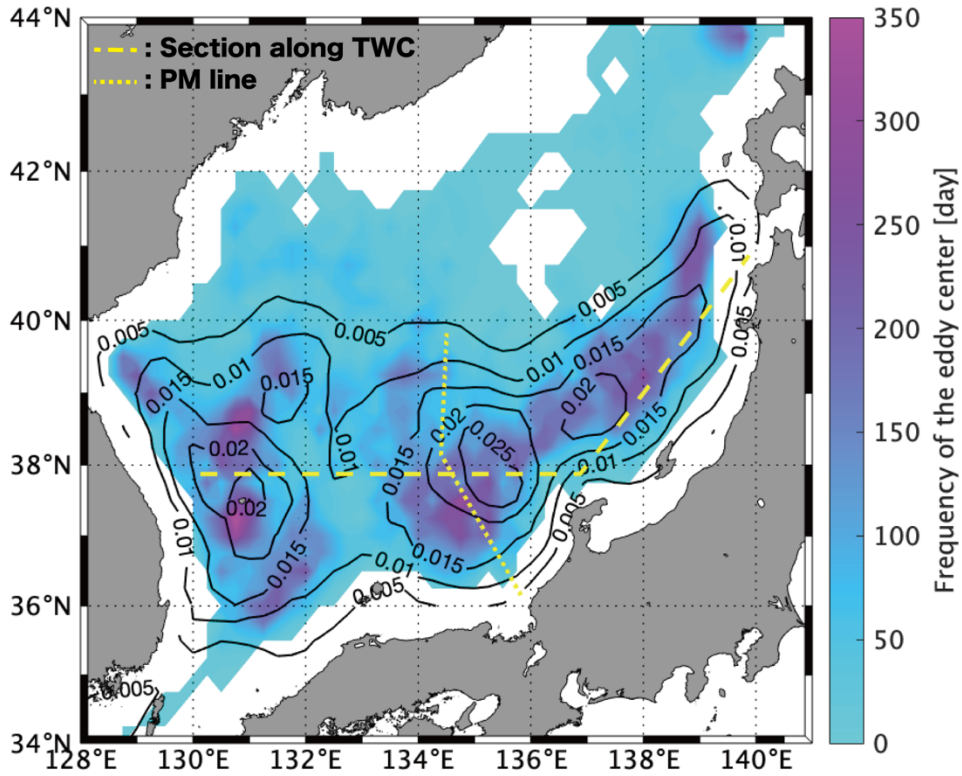
Fig.2-12: Spatial distribution of mesoscale eddies computed over the entire data record of 23 years (1993–2015) and eddy kinetic energy (EKE) over 25 years (1993–2017). The number of eddies in each 0.25° grid is represented by the color shade. The black contours show the EKE. The yellow dotted line represents the position of the PM line. The yellow dashed line shows the section along the TWC, as presented in the Hovmöller diagram (Fig. 2-15a).
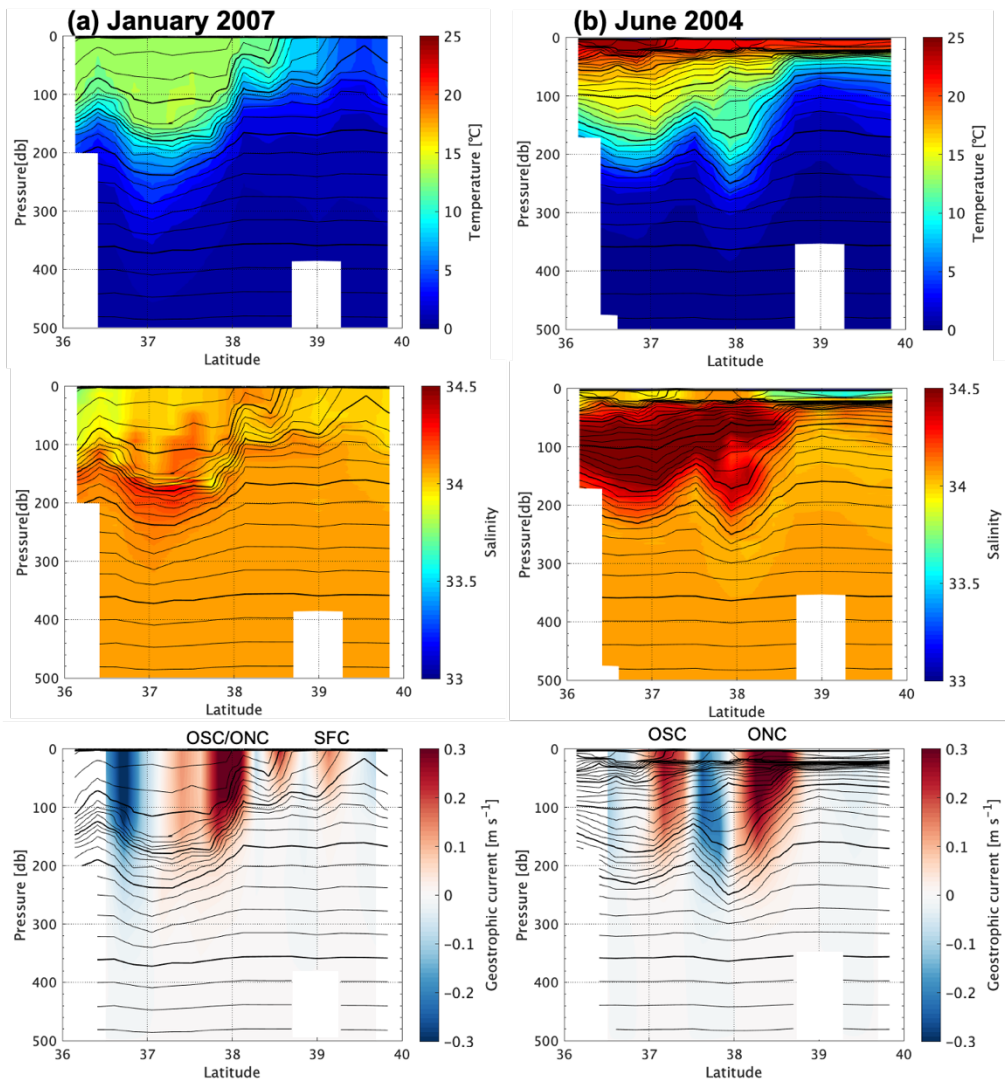
Fig.2-13: The hydrographic structure of temperature (upper panels), salinity (middle panels) and geostrophic current (lower panels) along the PM line in (a) January 2007, and (b) June 2004. Color shows temperature or salinity or geostrophic velocity and isolines show potential density. Positive values indicate eastward or north-eastward current.
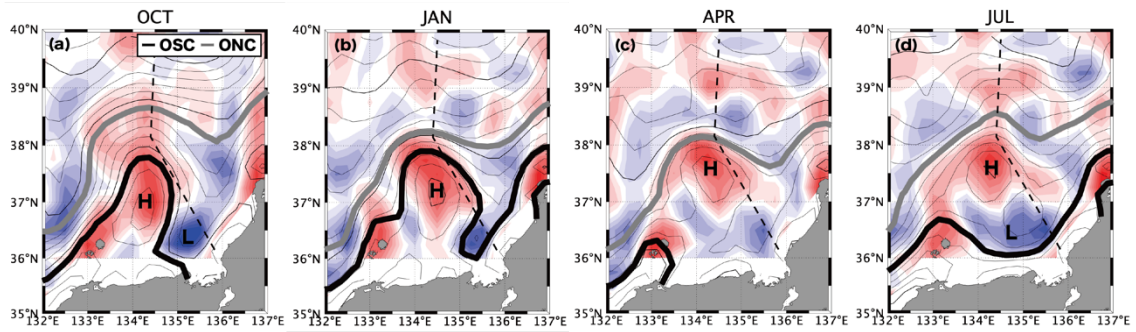
Fig.2-14: Monthly climatology of ADT (isolines) and relative vorticity (color shade) in (a) October, (b) January, (c) April and in (d) July. In panels, thick black and gray line show the OSC and ONC pathways.
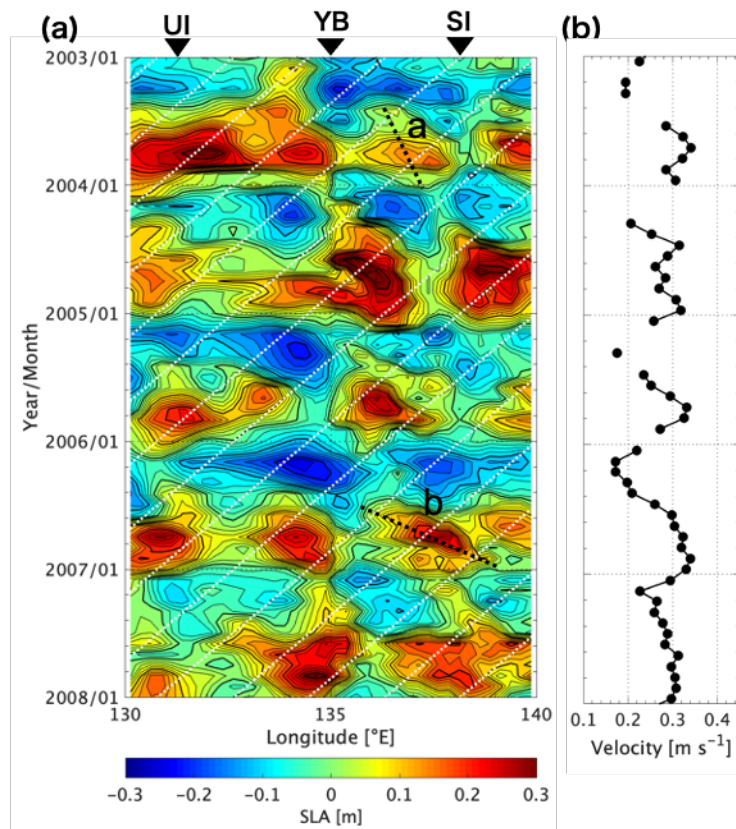
Fig.2-15: (a) Timeseries of SLA along the TWC pathway (yellow dashed line in Fig. 2-12) during 2003–2008. The white dashed line represents the westward velocity of the planetary Rossby wave. Black triangles show positions of the respective topographic features: the Ulleung Island (UI), the Yamato Basin (YB), and the Sado Islands (SI). The black dashed lines indicate the movements of eddies for which propagation velocities are calculated. (b) Current magnitude along the ONC.
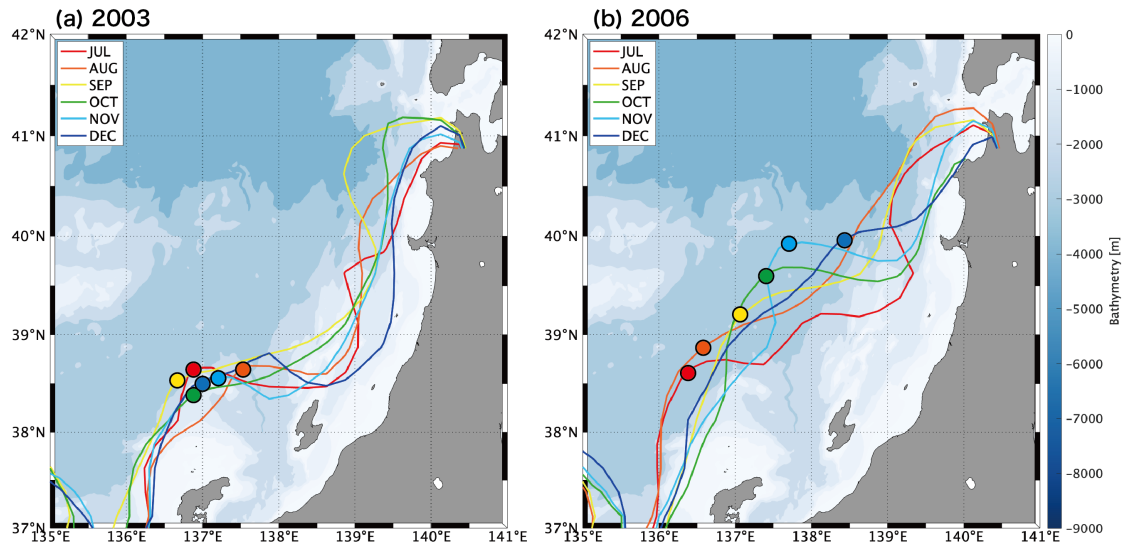
Fig.2-16: Transition of ONC's monthly pathway from July to December in (a) 2003 and in (b) 2006. Maximum curvature points of each meandering pathway were indicated by filled, colored circles, which track the temporal change of ONC paths during the meandering event. Color shade shows the bathymetry.
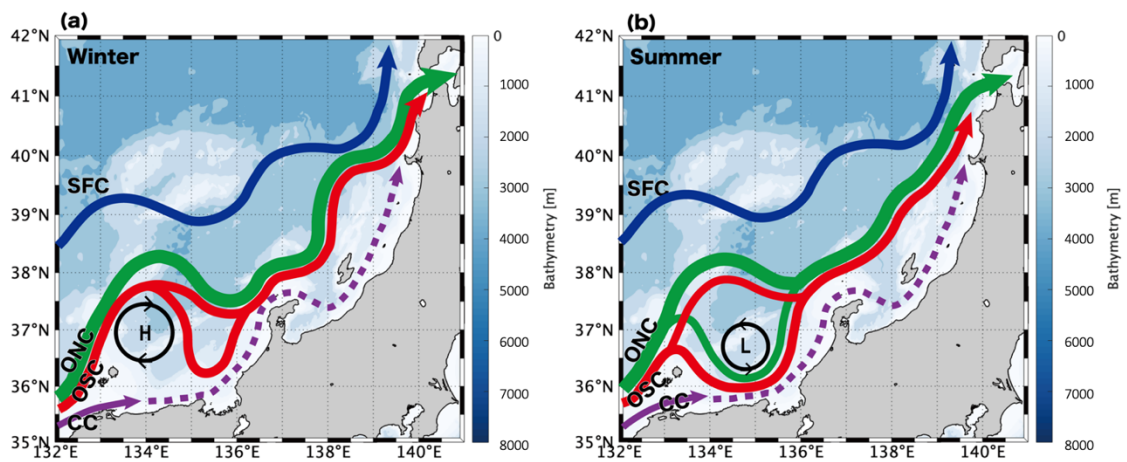
Fig.2-17: Schematic map showing three branches of the TWC and the SFC based on this study in (a) winter and (b) summer. Solid lines show the main pathway of each branch in this study. Abbreviations for current names are the following: CC, Coastal Current (purple); OSC, Offshore South Current (red); ONC, Offshore North Current (green); and SFC, Subpolar Front Current (blue). Broken lines show known pathways from past studies. However, these pathways were not detected in this study. Black circles respectively show the anti-cyclonic and cyclonic eddies refer to the mean hydrography. Blue shading shows the bathymetric contours.

	A (132°E)		B (135°E)		C (138°E)		mean
	n	*rmsd*	*n*	*rmsd*	*n*	*rmsd*	
OSC	224	0.27	146	0.21	48	0.38	0.29
ONC	264	0.25	264	0.22	239	0.25	0.24
SFC	286	0.27	286	0.31	286	0.28	0.28
CC	56	0.35	11	0.20	2	-	0.27

Table 2-1: Relationship between streamline-based latitudes and peak-based latitudes of ADT-based geostrophic current magnitude. Data number (n) and root mean square difference between two latitudes (*rmsd*) at longitude line of 132°E, 135°E, and 138°E for the four TWC branches (Fig. 2-5b).

3. Intra-annual variation of wind-induced near-inertial internal waves in association with the Tsushima Warm Current and mesoscale eddies

3.1   Introduction

Atmospheric disturbances can generate inertial oscillations in the oceanic surface mixed layer (SML; D'Asaro, 1985). Kinetic energy in the SML is transported into the ocean interior via near-inertial internal wave (NIW), which plays a key role in energy circulation in the ocean. The NIW propagates horizontally and vertically. Their behavior is restricted by a dispersion relation based on linearized equations of motion (Alford et al., 2016). The frequency range of NIW is resident between the inertial frequency dependent of latitude $f(\varphi)$ and buoyancy frequency $N(z)$. Here, $f(\varphi)$ and $N(z)$ are defined as

$$f(\varphi) = 2\Omega \sin \varphi \qquad (1)$$

$$N(z) = \sqrt{-\frac{g}{\rho}\frac{d\rho}{dz}}. \qquad (2)$$

Therein, φ denotes the latitude, Ω stands for the angular velocity of rotating Earth, ρ expresses the seawater density, g denotes the acceleration of gravity, z signifies a vertical coordinate, positive upward.

If horizontal shear exists in geostrophic current, then ζ_g, the vertical component of relative vorticity (RV), can modify the minimum frequency of NIW ω_{min}, i.e. from $f(\varphi)$

to

$$\omega_{\min} = f(\varphi) + \frac{\zeta_g}{2}. \qquad (3)$$

The RV is expressed as

$$\zeta_g = \frac{\partial v_g}{\partial x} - \frac{\partial u_g}{\partial y}, \qquad (4)$$

where u_g and v_g respectively represent the zonal and meridional geostrophic current velocities (Kunze, 1985). In general, subinertial internal waves, where the wave frequency is less than $f(\varphi)$, can propagate only through a body of negative vorticity ($\zeta_g <$ 0) (Kunze, 1985). A good example is an inner core of anti-cyclonic eddy (ACE). The RV approaches zero at the bottom of ACE. Thereby, downward propagation of the NIW below the ACE is prevented. Amplification of NIW kinetic energy occurs by accounting for the conservation of action flux. Kunze et al. (1995) reported energy transfer through the breaking of NIW to turbulent mixing based on the high dissipation rate at the ACE bottom.

Whitt and Thomas (2013) explained that vertical shear of geostrophic current Ri_g affects the minimum frequency $\omega_{\min}$ of NIW, defined as

$$\omega_{min} = f(\varphi)\sqrt{1 + Ro - Ri_g^{-1}}, \qquad (5)$$

using the dimensionless quantity of Rossby number Ro and the gradient Richardson number Ri_g as

$$Ro = \zeta_g / f(\varphi), \quad (6)$$

$$Ri_g = N(z)^2 \Big/ \left[\left(\frac{\partial u_g}{\partial z} \right)^2 + \left(\frac{\partial v_g}{\partial z} \right)^2 \right]. \quad (7)$$

The minimum frequency ω_{min} becomes small when Ri_g is large.

The NIW is a ubiquitous phenomenon, occurring in any ocean on the Earth. Details of its behaviors might be modulated because of the background environments: latitude-dependency of the NIW minimum frequency, distribution of RV, vertical shear of geostrophic current, and so on. The Sea of Japan, a semi-closed marginal sea, is adjacent to continental Eurasia to the north and the Japanese archipelago to the south. Vertically, the sea is largely separated into two layers. Hydrographic structures of the upper layers are mostly affected by the Tsushima Warm Current (TWC) (salinity > 34, and σ_θ > 26.7 kg m^{-3}), whereas the Japan Sea Proper Water (JSPW) (temperature $\leq$ 1.0 °C, and σ_θ > 27.2 kg m^{-3}) is underneath the main thermocline, from roughly 300 m depth (Senjyu, 1999; Wagawa et al., 2019).

Many studies have been conducted to elucidate the NIWs in the Sea of Japan based on hydrographic surveys and numerical simulations (e.g. Mori et al. 2005; Jeon et al. 2019; Watanabe and Hibiya, 2018). Based on multiple mooring observations that were conducted throughout wide regions of the Sea of Japan, Mori et al. (2005) reported temporal and spatial variations of near-inertial oscillations in the deep water. According

to their calculations made using a mixed-layer slab model, the atmospheric energy input to the ocean becomes greatest during winter when the seasonal northwesterly wind from the Eurasian Continent tends to dominate. They estimated that nearly 30% of wind-induced energy in the SML can reach a depth of 1450 m in the Yamato Basin.

Jeon et al. (2019) estimated the amount of near-inertial energy in SML and interior waters underneath SML, based on a high-resolution numerical model with realistic wind forcing (Hirose et al. 2017). According to their analyses, the inertial motion in SML is higher north of the Subpolar Front. The NIW kinetic energy in the deep layer (400–1000 m) is large in the Yamato Basin, where the surface RV is negative. They indicated that the NIW kinetic energy is transported efficiently from SML to deep layers in the negative RV area.

In the region off the Sado Island in the eastern Sea of Japan (Fig. 3-1), mesoscale oceanic structures such as meandering of the TWC and isolated eddies associated with the TWC exist and add complexity to the mean current field (Wagawa et al., 2019). Eddy activity in this area is regarded as the most energetic in the Sea of Japan as well as those in the Yamato Basin and Ulleung Basin (Fig. 2-12) (Isoda 1994; Morimoto et al. 2000). In the region off Sado, the Fisheries Research Agency of Japan has regularly conducted ship-based hydrographic surveys and bottom-mooring observations to clarify the

hydrographic structures and their variation (Wagawa et al., 2019; Kawaguchi et al. 2020).

Kawaguchi et al. (2020), based on the current meter data obtained by the mooring observations at the site during 2015 (yellow circle in Fig. 3-1), reported a remarkable event: the trapping and amplification of NIW inside an ACE. The amplification of NIW occurred at the bottom of the ACE. Multiple inertial (MI) oscillations (e.g., $2f$, $3f$, $4f$, $5f$) were identified at the amplified depth. The gradient Richardson number Ri_g (Eqn. (7)) indicated Kelvin–Helmholtz (KH) instability, suggesting turbulent mixing via breaking of NIWs.

The research project of the Fisheries Research Agency – Atmosphere and Ocean Research Institute Tsushima Warm Current Observatory (shortly, FATO) was launched in the year of 2017, aimed at elucidation of the TWC-related oceanic phenomena, such as long-term variations of the TWC system (Chapter 2), short-term responses of internal waves and microscale turbulence to atmospheric forcing (Kawaguchi et al., 2021b). Those might engender the determination of kinetic energy circulation over the wide area of the Sea of Japan. Three research cruises and a mooring observation were conducted for the FATO project in 2019. The present study examines characteristics of NIW, which plays a key role in transmitting kinetic energy from the surface layer, which is often controlled by the TWC, to the deep layer occupied by the JSPW. Our main questions are

the following: To what depth does kinetic energy in the SML reach? How do the TWC and mesoscale eddies affect NIW behaviors?

This chapter consists of the following subsections. Section 3.2 presents the data and methodology. Section 3.3 gives a description of the current structures with year-round mooring data. Temporal variations of currents are assessed from two perspectives: geostrophic currents representing the TWC and super-inertial currents associating with NIWs. This subsection includes particular examination of three events forced by wind disturbance to examine propagation properties of NIWs. Section 3.4, presents reflection and refraction of NIW in the discontinuity of buoyancy frequency $N(z)$. In Section 3.5 gives a summary of all findings obtained from this study.

3.2   Data

This study mainly analyzed a time series of oceanic current data obtained from year-round mooring at the FATO site, along with hydrographic data from repeated ship-based observations during the mooring period. In addition, wind speed data were examined to evaluate the energy source of internal waves from the atmosphere. Details of observation programs and data treatments are provided hereinafter.

3.2.1 Mooring observations

A year-long time series of oceanic current data obtained off Sado Island (38.72°N, 137.83°E), designated as the FATO mooring station, are marked by a yellow circle in Fig. 3-1. The water depth is approximately 1777 m. The local inertial frequency, $f(\varphi)$ is 9.123 $\times 10^{-5}$ s^{-1}. The local inertial period is 19.1 h. Using data from these year-long observations, we tried to answer a key question: How does kinetic energy in the SML reach to great depths? On the mooring system, the position of instruments was determined carefully to maximize the data coverage in a vertical range. Thereby, we combined multiple sets of current meters on the mooring system: upward-looking and downward-looking acoustic Doppler current profilers (ADCP 75 kHz and 300 kHz Workhorse; Teledyne RD Instruments Inc.) set respectively at depths of 390 and 420 m, with three sets of electromagnetic current meters (INFINITY-EM; JFE Advantech Co., Ltd.) set at 600, 700, and 800 m, and four single-point current meters (Aquadopp; Nortek) at 900, 1000, 1100, and 1200 m (Fig. 3-2). This allocation of instruments provides constant vertical resolution of 8 m for depths from 57 m to 494 m, and 100 m from 600 m to 1200 m. The temporal interval for the measurements was set to 1 h at the entire depths. According to the specifications provided by the manufacturers, the velocity precision is 0.005 m s^{-1} for the Workhorse and Aquadopp, and 0.01 m s^{-1} for INFINITY-EM. Before the analyses for

NIW, velocity data larger than 1.0 m s^{-1} were regarded as error and were removed manually. Correction for magnetic deviation of +8.90 degrees at the site was applied.

On the same mooring, we obtained a time series of temperature and salinity data at selected depths of 450 and 1770 m with CT-sensors (INFINITY-CTW; JFE Advantech Co., Ltd., and SBE-37 MicroCAT; Sea-Bird Electronics, Inc.). The temporal measurement interval was set as 1 h. According to the specifications, the precisions of conductivity and temperature were, respectively, 0.01 mS cm^{-1} and 0.01 °C for the Infinity-CTW, while they were 0.003 mS cm^{-1} and 0.002 °C for the MicroCAT.

3.2.2 Hydrographic observations

Four research cruises were conducted during the mooring period – June, July, October in 2019 and February 2020, respectively, using the T/V Tenyo-maru of the National Fisheries University, the T/S Oshoro-maru of Hokkaido University, the R/S Shinsei-maru of the Japan Agency for Marine–Earth Science and Technology (JAMSTEC), and the R/V Hokko-maru of the Japan Fisheries Research and Education Agency. For convenience, those four ship-based expeditions are abbreviated hereinafter respectively as (1) TY1906, (2) OS1907, (3) KS1910, and (4) HK2002.

During the cruises, conductivity–temperature–depth (CTD; Sea-Bird Electronics,

Inc.) profiles were collected at depths from the surface nearly to the seafloor around the

FATO mooring site (yellow circle in Fig. 3-1). The raw CTD data were averaged to 1-

dbar intervals. The salinities were calibrated using salinity determination procedures of

bottle-sampled waters. The temperature and salinity profiles were used to estimate the

mixed-layer depth (MLD) and the buoyancy frequency $N(z)$. In this study, the MLD was

defined as the first depth at which the temperature was 0.25 °C less than the temperature

at 5 m (Hosoda et al., 2010).

3.2.3   Satellite altimetry

For the aim of detection of mesoscale features in the near-surface layer, this study

uses a satellite-based altimeter dataset, "Global Ocean Gridded L4 Sea Surface Heights

and Derived Variables NRT," which is distributed by the Copernicus Marine Environment

Monitoring Service (CMEMS, http://marine.copernicus.eu/ser-vices-portfolio/access-to-

products/). The sea surface height (SSH) and SSH-based geostrophic velocity (u_g, v_g)

were obtained during multiple satellite examinations (e.g., TOPEX-Poseidon, Jason 1–3).

The daily resolutions were of 0.25 degree (approximately 20 km) in horizontal scope. The

geostrophically balanced RV, ζ_g (Eqn. (4) presents the definition) is calculated in each

grid for SSH data.

3.2.4　Atmospheric forcing

The kinetic energy input from the atmosphere to SML, generating the inertial oscillation, was estimated from the slab model (Pollard and Millard, 1970; D'Asaro, 1985). The complex form of equations for the inertial current in the SML is

$$\frac{dZ}{dt} + DZ = \frac{T}{H}, \quad (8)$$

where complex quantities Z, T, and D are introduced for convenience.

$$Z = u + iv, \quad (9)$$

$$T = \frac{(\tau_x + i\tau_y)}{\rho}, \quad (10)$$

$$D = d + if(\varphi). \quad (11)$$

Therein, τ_x and τ_y respectively denote zonal and meridional wind stress components, H signifies the SML thickness, and d is the damping constant. Damping constant d parameterizes the energy decay from the SML to the deeper layer. For calculation, the damping constant d is set as $d^{-1} = 4$ days and to the thickness of the SML. H is assumed to be constant: findings reported by Kawaguchi et al. (2021a) indicate that $H = 30$ m. The wind stress vector is computed using the conventional quadratic law: $\tau_x = C_D \rho_a |w_x| w_x$, where air density ρ_a is 1.2 kg m^{-3} and drag coefficient C_D is 1.3×10^{-3}. The inertial component of velocity Z_I is

$$Z_\text{I} = Z_\text{SML} - Z_\text{E}, \quad (12)$$

where Z_E is the Ekman transport modified by frictional damping

$$Z_\text{E} = \frac{T}{DH}. \quad\quad (13)$$

The equation for the inertial component of velocity is obtained from substituting Eqn.

(12) to Eqn. (8) as

$$\frac{dZ_I}{dt} + DZ_I = -\frac{dZ_E}{dt}. \quad\quad (14)$$

An energy equation for the SML is obtained by multiplying (14) by the complex conjugate

Z_I^* as

$$\frac{d|(1/2)Z_\text{I}|^2}{dt} = -r|Z_\text{I}|^2 - \mathcal{R}\left[\frac{Z_\text{I}}{D^*H}\frac{dT^*}{dt}\right]. \quad\quad (15)$$

For the calculation of surface wind stress, we use the eastward and northward

wind velocity (w_x, w_y) at 10 m height above the sea surface in the "grid point value of

meso-scale model (GPV-MSM)" dataset compiled by the Japan Meteorological Agency

(JMA). The horizontal resolutions are 0.05 degree in latitude and 0.0625 degree in

longitude. The temporal resolution is 1 h.

3.3   Results

3.3.1   Characteristics of the observed currents in 2019–2020

In this subsection, the intra-annual variation of mesoscale phenomena and super-

inertial phenomena are described from the current velocity data, and from atmospheric

disturbances from wind velocity data at the FATO mooring site.

1)   Mesoscale current structures

We first examine the intra-annual variation of mesoscale phenomena, which can

strongly affect the NIW behavior, as described in Section 3.1. Figure 3-3a indicates the

time series of RV at the mooring site; Fig. 3-4 shows a horizontal map of SSH and RV.

The geostrophic component of current velocity (u_g, v_g) in Fig. 3-3b was estimated using

the running mean over 10 days for the removal of short-term variability. The Okubo–

Weiss parameter OW is a parameter to identify mesoscale eddies, which indicates the

importance of deformation and rotation (Okubo, 1970). This parameter is expressed as

$$OW = S_n^2 + S_s^2 - \zeta_g^2, \qquad (16)$$

where $S_n{}^2$ represents the normal strain and $S_s{}^2$ denotes the shear strain:

$$S_n^2 = \frac{\partial u_g}{\partial x} - \frac{\partial v_g}{\partial y}, \qquad (17)$$

$$S_s^2 = \frac{\partial v_g}{\partial x} + \frac{\partial u_g}{\partial y}. \qquad (18)$$

The sum of $S_n{}^2$ and $S_s{}^2$ is called the total strain, which implies energy transfer from a

mesoscale phenomenon to internal waves (Polzin, 2008).

The FATO mooring site shows complex mesoscale structures as the TWC.

Mesoscale eddies pass through one after another (Figs. 3-3 and 3-4). According to the SSH-based geostrophy, the near-surface jets existed intermittently during June to early September in 2019 (Figs. 3-3b and 3-4a). The maximum of the geostrophic current reaches 0.4 m s^{-1}. It reaches 0.1 m from 60 m to 150 m at the end of August. It is well defined that the offshore north branch (ONC) of the TWC passes through the mooring site. The definition of the TWC pathway was presented in Chapter 2. Paired vortices of a cyclonic eddy (CE) and an ACE reside at north and south sides across the main axis of the ONC (Fig. 3-4a). The OW parameters are -9.3 × 10^{-3} for the ACE and -8.7 × 10^{-3} for the CE (middle panel of Fig. 3-4a). The relative vorticity ζ_g inside these vortices is greater than the total strain. Additionally, the total strain shows a large value of 0.21 northeast of the FATO mooring (lower panel of Fig. 3-4a). Kawaguchi et al. (2021a) observed signals of internal waves and marked turbulent mixing at the boundary between the ACE and the CE, where the total strain shows a large value (Fig. 3-11d).

It is noteworthy that that the mooring site was located near the center of the CE during October–December 2019 (Fig. 3-4b), when the surface RV indicates positive values through at the period (Fig. 3-3a). The current magnitude was especially small. It was less than 0.1 m s^{-1} during October through mid-November.

The ACE persisted for longer periods near the FATO mooring (Fig. 3-4c).

Corresponding to the ACE, the surface relative vorticity clearly indicates negative values

(Fig. 3-3a). The current magnitude was persistently strong as approx. 0.2 m s^{-1} during

January–May 2020 (Fig. 3-3b). The maximum geostrophic current magnitude (running

mean over 10 days) reached almost 0.5 m s^{-1} at 60 m depth in January and March. This

ACE was migratory: it moved northeastward during this period. The mean travel velocity

estimated from the location of the ACE core (Figs. 3-4b and 3-4c) was approx. 0.01 m s^{-1}.

2)   Signatures of super-inertial motion

Deviation of the current magnitude from the running mean over the local inertial

period (19 h) and its vertical shear are shown respectively in Figs. 3-3c and 3-3d. Vertical

shear is represented as the sum of vertical gradient of eastward and northward components

(i.e. $Vz = \sqrt{u_z^2 + v_z^2}$) based on the vertical profile consisting of data of 75 kHz and 300

kHz ADCPs (Fig. 3-2), where the vertical spacing is 8 m, as described. These figures

clearly depict the existence of internal gravity waves (IGWs) and its vertical propagations.

The "IGW" includes the NIW, but it also stands for oceanic motions with super-inertial

frequency. In the high-passed velocity, the strong current exceeding 0.2 m s^{-1} was present

recurrently in the upper layer for the periods of August 11–19, September 20 – October

14, November 13 – December 17, and December 27 – May 2 (Fig. 3-3c).

As presented earlier (Fig. 3-4), mesoscale structures in the downstream region of TWC off Sado Island were dynamic and transitional during mooring observations in 2019–2020. For the SSH-based mesoscale structures and vertical shear of the high-passed velocity, we particularly examine the following periods: August 15 – September 15 in 2019 (Term I), November 20 – December 20 in 2019 (Term II), and February 10 – March 10 in 2020 (Term III). These terms have different mesoscale structures, respectively characterized by a meandering TWC jet, an isolated CE, and an ACE. We specifically examine the influences of those mesoscale features on the propagation properties of IGWs in the upper layer. Among these terms are included differences of density stratification and wind forcing attributable to seasonal variation. It is difficult to eliminate these effects completely using one year mooring data. Therefore we assess these differences in a later subsection.

Regarding details of wave characteristics, vertical migration of a profound kinetic energy patch was tracked temporally in the time series of the vertical velocity shear (Fig. 3-5). Findings indicate that certain wave packets, characterized by recognizable vertical shear, propagate downward from 100 to 200 m during August 20– 30 of Term I (Fig. 3-5a). The downward group velocity estimated from wave packet

77

migration is approximately 17.5 m day^{-1}, which is a rough estimation because density stratification effects were ignored (black arrows in Figs. 3-3d and 3-5a). During the period, the super-inertial current exceeds 0.1 m s^{-1} in magnitude at depths from the surface to deeper than 500 m (Fig. 3-3c). The maximum depth of the downward internal wave is of similar depth at the bottom of baroclinic geostrophic flow (solid lines in Fig. 3-5a). Underneath the maximum level, the wave signature visualized in the vertical shear attenuates rapidly. During Term II, the super-inertial current and vertical shear are amplified at depths of 100–250 m during November 30 through December 15 (Figs. 3-3c, 3-3d and 3-5b). The downward group velocity is 7.3 m day^{-1}. The maximum depth of strong vertical shear in Term II is greater than that in Term I.

From the super-inertial current field (Fig. 3-3d), it is noteworthy that the indication of vertically isolated wave signature persisted for a month of Term III: February–May 2020. During the period, the magnitude of vertical shear was extraordinarily large: 0.02 s^{-1} for depths of 150–350 m (Fig. 3-5c). The level of strong vertical shear apparently coincides with the bottom depth of geostrophic current. Near-surface RV shows negative anomaly attributable to the existence of ACE (Figs. 3-3a and 3-4c). Thereby, we assume that the NIW amplification occurred in association with vertical variation of vorticity for the anti-cyclone, as observed in that neighborhood (e.g.

Kawaguchi et al., 2020).

The strength of the upper 200 m vertical shear during Term III is less, at 3.1×10^{-4} s^{-1}, than those in the remainder of the mooring period. Additionally, downward propagations of wave packets are not evident in this term (Fig. 3-5c). Figure 3-6 shows vertical profiles of temperature, salinity, density, and buoyancy frequency from the shipboard CTD observation. The MLD is estimated according to the temperature profile and described in Section 3.2.2. Consequently, we estimated MLD of 176 m for Term III, where it is based on the temperature profile of HK2002. The MLDs in Terms I and II (12 m and 35 m respectively) are beyond the measurement range of the upward ADCP at the FATO mooring (Table 3-1). According to the CTD profile (Fig. 3-6), one would say that strong vertical shears are restricted at the vertical level underneath the SML.

3) Kinetic energy and momentum input from the atmosphere

An important energy source for NIWs in the Sea of Japan is atmospheric disturbances that often traverse the sea from west to east (Mori et al., 2005). We estimate the near-inertial kinetic energy input from the atmospheric disturbances and the inertial current in SML using the slab model presented in Section 3.2.4 (Pollard and Millard, 1970; D'Asaro, 1985).

The cumulative energy input into the SML for the mooring period is depicted in Fig. 3-3a. During Term I, the kinetic energy is increased in association with the passage of typhoon KROSA, which passed through the Sea of Japan on 15–16 August 2019 (Figs. 3-3a and 3-7a). Following KROSA, multiple cyclones passed over the Sea of Japan during three terms of November 11, 13, and 15 (Figs. 3-3a and 3-7b) and on February 3 (Figs. 3-3a and 3-7c). According to the slab model calculation, the accumulated near-inertial kinetic energy inputs are 1.41 kJ m^{-2} (0.47 kJ m^{-2} day^{-1}), 2.37 kJ m^{-2} (0.40 kJ m^{-2} day^{-1}), and 1.81 kJ m^{-2} (0.61 kJ m^{-2} day^{-1}) for the respective periods of August 14–17, November 10–16, and February 2–5 (Fig. 3-3a, Table 3-1). For the annual record, the maximum amount of total energy gain occurred during Term II, when the magnitude of vertical shear was strongest at the surface (Fig. 3-5b).

In general, the horizontal scale of atmospheric disturbances is an important factor for determining the horizontal wavelength of internal waves that propagate into the ocean interior (Alford et al., 2016). The horizontal scale will be used for calculation of the wave frequency and group velocity based on the linear theory of internal-wave dispersion relation (Section 3.3.4). The radius of typhoon KROSA, as estimated from the area in which the wind speed was greater than 30 knots, was 300 km (https://www.data.jma.go .jp/fcd/yoho/typhoon/position_table/format_csv.html) (Fig. 3-7a). When particularly

addressing the horizontal structures of wind stress curl $\boldsymbol{\tau}$, one creates some finer-scale features (Fig. 3-7), so that their horizontal scale is roughly one order smaller than the radii indicated above. The wind stress curl $\boldsymbol{\tau}$ is

$$\text{curl } \boldsymbol{\tau} = \frac{\partial \tau_y}{\partial x} - \frac{\partial \tau_x}{\partial y}. \qquad (19)$$

For this study, the widths of band-shaped strong wind stress curl were roughly estimated. According to our estimate, the scales of the wind stress curl are, respectively, about 40, 70, and 40 km for the cases of air disturbances during the terms. Kawaguchi et al. (2021a) reported that the wind disturbance caused by the Ekman pumping triggered generation of NIWs.

3.3.2   Frequency spectra

Figure 3-5 shows the vertical shear of high-passed velocity greater than the local inertial frequency. Therefore the figure includes signals of multiple frequencies. Calculation of rotary frequency spectra of the ADCP horizontal currents enables characterization of every prominent frequency that forms the intricate signature of IGWs. For that, we use the complex form of horizontal current ($u + iv$), where u and v respectively represent the zonal and meridional components. The complex velocity respectively has clockwise (CW) and counterclockwise (CCW) rotation for negative and

positive frequencies. Power spectra density (PSD) curves are referred from semi-empirical canonical curves reported by Garrett and Munk (1975). In addition, the reference level of the energy ratio

$$\frac{E_{CW}}{E_{CCW}} = \frac{(\omega+f)^2}{(\omega-f)^2}, \quad (20)$$

based on the linear wave theory (Gill, 1982), is shown for evaluation of the observed current (Fig. 3-8).

Actually, horizontal kinetic energy (HKE) for CW rotation takes a maximum value around the local inertial frequency, $f(\varphi) = 9.123 \times 10^{-5}$ s^{-1} ($\varphi = 38.72$ °N). It is dominant throughout the year-long mooring record (upper and middle panels in Fig. 3-8). From rotary spectral analysis, results show that that the energy peak near-f for CW is greater by a factor of 100 and more than that for CCW. In all three terms, the near-f peak is recognizable at the overall depth range, from the surface to the maximum observed depth of 1200 m (top panels in Fig. 3-8). From this evidence, one can ascertain the predominance of NIW over all frequencies of high frequency motions at the mooring location.

The HKE around f is the largest in Term II as 7.1×10^3 m^2 s^{-2} cph^{-1}. The energy is more than 10 times greater than that in other terms. The kinetic energy input from the wind into the SML is the largest in Term II (Fig. 3-3a, Table 3-1) (Section 3.3.1). The

HKE for the geostrophic current, with a frequency that is less than diurnal, is high in Term III, although it is low in Term II (top and middle panels in Fig. 3-8). This difference is attributable to the geostrophic currents associated with ACE, which remained near the FATO mooring in Term III (Fig. 3-4c). Additionally, the geostrophic current magnitude is small in Term II, which is likely to be associated with the fact that the mooring location is close to the center of CE with the positive RV (Fig. 3-4b).

The vertical distribution of kinetic energy differs greatly among the three terms irrespective of the dominant peak near f throughout the whole depth (top panels in Fig. 3-8). In Terms I and III, the near-inertial energy is strongest at middle depths roughly between 200 and 300 m, whereas in Term II it is strongest in the shallower depths from the surface to 200 m. The depth range characterized by the maximum HKE in Terms I and III correspond well to the bottom part of the geostrophically balanced baroclinic current (10 days running mean current magnitude in Fig. 3-3). Amplifications of the NIW signal at the bottom of the geostrophic current are displayed in both terms, as discussed previously at the same site of Kawaguchi et al. (2020).

The energy ratio between CW and CCW motions emphasizes double inertial oscillations, i.e. $\omega = 2f$ (bottom panels in Fig. 3-8). Kawaguchi et al. (2020) reported MI oscillations in October 2015, based on year-long mooring at the FATO site. The

oscillations were recognized at the bottom of the anti-cyclonic core, where NIW amplification occurred. Danioux et al. (2008) has theoretically and numerically elucidated that the MI oscillations are generated by the nonlinear interaction of waves. Energy ratios between CW and CCW motions in this study correspond well to the reference curve (lower panels in Fig. 3-8), which is evaluated from the linear wave theory (Gill, 1982). The near-inertial energy in this study is 10 times lower than the energy reported by Kawaguchi et al. (2020). The nonlinear effect is presumed to be small for the mooring current obtained in Term III. Although the HKE in Term II is 10 times higher than that in Term III, the MI oscillations are not detected, which remains an unsettled question.

Tidal components of the HKE are small at the overall depth range in all terms (Fig. 3-8) as noted in earlier studies (Mori et al., 2005). This tendency arises because the four straits connecting the Sea of Japan with other oceans are shallow (approx. 150 m) and narrow. Therefore tidal oscillations are small, except near the straits. We explicitly exclude the frequencies of MI oscillations and typical tidal constituents for the discussion of HKE at the FATO mooring. In short, we assume that the activity of NIW dominates the high-frequency motion. We mainly describe inertially band-passed signatures in the following subsection.

3.3.3 Near-inertial internal waves

Before detailed examination of NIW characteristics, the Wentzel–Kramers–Brillouin (WKB) scaling procedures were adopted for these velocity data to reduce the effects of vertically varying density stratification (Leaman and Sanford, 1975). The velocity components, $u(z)$ and $v(z)$, at each depth are normalized using the local buoyancy frequency $N(z)$ as

$$u^*(z) = \frac{u(z)}{\sqrt{N(z)/N_0}}, \qquad (21)$$

where $N_0 = 5.24 \times 10^{-3}$ s^{-1} = 3 cycles per hour (cph) is the reference buoyancy frequency. The stretched depth for a given $N(z)$ profile is

$$dz^* = \frac{N(z)}{N_0} dz. \qquad (22)$$

Vertical profiles of $N(z)$ were calculated from those of temperature and salinity at the FATO mooring site, as depicted in Fig. 3-6. The vertical shear of the band-passed eastward velocity near $\omega = f$ for each term is depicted in Fig. 3-9 (note: northward velocity shows similar features, so it is not shown). The near-inertial component (u_f, v_f) is band-passed using an FFT filter, with upper and lower limits of $0.9f$ and $1.1f$ (Thomson and Emery, 2014). Upward and downward phase propagations can be identified clearly by band-passing procedures and WKB scaling.

The iso-phase lines show intricate features by which they climb up and down in

Term I (Fig. 3-9a). A wave packet following the passage of KROSA on August 15 (Fig. 3-7a), propagates downward on August 15–30, from 200 to 500 stretched meter (sm) in the stretched depth (Fig. 3-9a). The propagation speed in a vertical sense, regarded as group velocity C_{gz} of internal wave, is estimated as about 20 sm day^{-1} by tracking energetic wave packets (dashed arrow in Fig. 3-9a). Both the iso-phase line (solid arrow in Fig. 3-9a) and wave packet (dashed arrow in Fig. 3-9a) move downward during this period. Phase and energy are widely known to propagate vertically in opposite directions (Gill, 1982). This inconsistency remains an open question. The atmospheric front passed over the mooring site on August 27, followed by subsequent travelling of multiple wave packets observed in the current meters.

In Term II, a wave packet originating from the cyclone propagates from the surface to 450 sm (Fig. 3-9b), providing vertical speed of approximately 17 sm day^{-1}. The kinetic energy provided from the atmosphere is continuous: between November 2019 and March 2020 (Fig. 3-3a). The wave signals remain strong throughout periods of Terms II and III (Figs. 3-9b and 3-9c). In Term III, the near-inertial HKE was outstanding throughout the entire observed depth, i.e. from near-surface to 300 sm (Fig. 3-9c).

Term III had a noticeable event of wave traveling in which the slope of the wave's iso-phase lines changed from upward to downward direction on February 28; the

respective vertical propagation speeds were 12.5 sm day^{-1} and 10.0 sm day^{-1}. We regard the direction change of the wave phase and the packet migration as reflecting at the horizontal plane at middle depth of approx. 300 sm. We will closely discuss the reflection of NIW and details of its properties in Section 3.5.

Figure 3-10 shows the gradient Richardson number Ri_g (defined in Eqn. (7)), a measure of the flow's stability. The value of Ri_g was calculated from vertical profiles of buoyancy frequency $N(z)$ (Fig. 3-6) and the magnitude of vertical shear, $\sqrt{u_z^2 + v_z^2}$, where we use the observed current velocity u and v (Fig. 3-5). In general, the flow becomes unstable when Ri is less than an *ad hoc* threshold of $Ri_c = 0.25$, where the destabilizing effect attributable to vertical shear dominates the counterpart of density stratification which stabilizes the system. The critical value for instability corresponds to 0.6 if its reciprocal, Ri^{-1}, is represented on a logarithmic scale (Fig. 3-10).

From this calculation, one can infer that KH instability can occur in a patchy manner during all three periods (Fig. 3-10). In Term I, a significant value of $Ri^{-1} > 100$ can be found for the downward-going wave packet in August 22–30 (Figs. 3-9a and 3-10a). In Term III, possible instability can be spotted in the dates of February 22–24 at 100–250 sm depth. Strong shear can cause internal wave breaking and subsequently results in smaller-scale turbulence through KH instability, which indicates a transfer of

kinetic energy across different-scale physical phenomena (Thorpe, 2005; Alford et al., 2016). Thereby, turbulent mixing occurs during atmospheric event areas.

Kawaguchi et al. (2021a) reported evidence of a relation between KH instability and turbulent mixing in the TWC eddies. They analyzed the current velocity measured from a shipboard ADCP and vertical profiles of the dissipation rates of turbulent kinetic energy ε with a quasi-free-falling turbulent profiler (VMP-250; Rockland Science, Inc.). Their shipboard observation was conducted along the E line across the two vortices in the off-Sado region (dashed line in Fig. 3-1). The dissipation rates of turbulent kinetic energy ε are defined as

$$\varepsilon = 7.5\nu\langle u_z^2\rangle, \quad (23)$$

where ν represents the molecular viscosity of seawater, u_z^2 signifies the variance of velocity shear measured by VMP-250, and the bracket represents ensemble averaging. According to Kawaguchi et al. (2021a), ACE exists on the western side of the line, whereas CE existed around the FATO mooring. The RV is negative in the core of the ACE, which is the same eddy observed at the FATO site in Term III (Figs. 3-4c and 3-11a). From VMP observations, dissipation rate ε became high at the bottom of ACE, where the vertical shear of geostrophic current changed rapidly (Figs. 3-11c and 3-11d). The strong vertical shear, satisfying the necessary condition of KH instability (Figs. 3-9 and 3-10),

likely to generate the turbulent mixing at the middle depths.

3.3.4   Characteristics of NIWs

In earlier sections, the vertical group velocities were estimated by tracking specific wave packets (Section 3.3.3). In this subsection, we evaluate the wave properties of the NIWs based on the linearized dispersion relation for internal waves. For this evaluation, we assume that vertical variation in $N(z)$ as negligible, and assume that wave frequency ω is near-inertial ($\omega \ll N(z)$). Then, we obtain the linear dispersion relation as (Massel, 2015) as

$$\omega^2 = f_{eff}^2 + \frac{N^2 k_h^2}{k_h^2 + k_z^2}, \qquad (24)$$

where ω stands for the wave frequency, k_h and k_z respectively denote the horizontal and vertical wavenumbers. The group velocities, C_{gh} and C_{gz}, respectively express horizontal and vertical directions as

$$C_{gz} = -\frac{(N^2 - f^2)\beta^3}{k_h(1+\beta^2)^{3/2}(f^2 + N^2\beta^2)^{1/2}}, \quad (25)$$

$$C_{gh} = -\beta^{-1}C_{gz}, \qquad (26)$$

where $\beta = k_h/k_z$ represents the propagation angle off the vertical (Cuyper et al., 2013). The wave frequency ω strongly influences the vertical propagation range because of the frequency range of the NIW as described in Section 3.1.

First, one can start from the estimation of vertical wavenumber. Figure 3-12 shows the vertical-wavenumber rotary spectra of the horizontal current vector that is band-passed around f. It is noteworthy that the stretched vertical profiles of complex horizontal velocity were Fourier transformed (Thomson and Emery, 2014). For calculations, the spectral energy was also separated into upward and downward energy propagation using the 2D-FFT (Thomson and Emery, 2014). The results are averaged over all spectral profiles, i.e. 745, 721 and 617 profiles, respectively, in Term I, Term II and Term III. Additionally, it is noteworthy that the shear spectrum was calculated by multiplying $(2\pi k_z)^2$ (right in Fig. 3-12).

According to Fig. 3-12, the vertical wavenumber spectrum in Term I is less energetic than the GM model (Fig. 3-12a), whereas the spectral level is more energetic in Term II (Fig. 3-12b) (Garett and Munk, 1975; Cairns and Williams 1976). In Term I, downward-propagating signals exceed upward-propagating signals by a factor of 3–4 at the high vertical wavenumber ($> 5\times10^{-3}$) (Fig. 3-12a). In Term III, upward and downward signals are almost comparable (Fig. 3-12c). We discussed this point in relation to the reflection of NIW in the next section. We determine the vertical wavelength from the shape of spectral curve (Fig. 3-12). According to Fig. 3-9, the structure of vertical shear changes with time. The kinetic energy shows broad peaks in Terms I and III, but these

peaks are not statistically significant. In Term II, the spectral curve represents a remarkable spectral peak at 5.5×10^{-3} cycle per sm (corresponding to 183 sm wavelength) (right panel in Fig. 3-12b). In Terms I and III, the vertical wavenumbers of near-inertial frequency are 7.0×10^{-3} cycle per sm (i.e., 142 sm) (right panel in Figs. 3-12a and 3-12c). Calculated values of vertical length are presented in Table 3-2.

We additionally evaluate the vertical wavelengths from the analyses of the empirical orthogonal function (EOF) (Thomson and Emery, 2014) for the vertical shear of the band-passed mooring velocity (Fig. 3-9). From EOF analysis, the eigenvectors can indicate a series of modal vertical wavelengths (left panels in Figure 3-13). The vertical wavelengths of the first three modes for the three event terms are presented in Table 3-2. According to Fig. 3-9, especially in Term I, multiple wave packets observed with temporal variation. The mean vertical wavelengths incorporated consideration of the variance is comparable with the vertical wavelength determined by the vertical wavenumber shear spectra (Fig. 3-12). In Term II, the iso-phase line slope is constant (Fig. 3-9b). The vertical wavelength in Term II is longer than that in Term I or Term III (Table 3-2).

Next, we estimate the internal wave frequencies ω and group velocities C_{gh} and C_{gz} from the dispersion relation for linear internal waves (Eqns. (24), (25), and (26)). Wavenumber k_z was found from the vertical wavenumber spectra (Fig. 3-12) and EOF

analysis (Fig. 3-13). In the meantime, the potential candidate of horizontal wavenumber k_h was inferred from horizontal scale of wind stress curl τ (Eqn. (19), Section 3.3.1 and Fig. 3-7). We estimated the wave frequency as near-inertial (i.e. $\omega \sim f$) from spectral analyses (Section 3.3.2, and Fig. 3-8). A high-precision value of wave frequency cannot be obtained from the spectrum because of the poor temporal resolution (0.08 cph, corresponding to 2 h) for the ADCP current data.

Variables related to observed internal waves are overviewed in Table 3-3. In Term I, the frequency of the internal wave generated by the typhoon KROSA is 1.08f. The vertical group velocities estimated using Eqn. (25) are 46.7 sm day^{-1} in Term I and 33.5 sm day^{-1} in Term II. The vertical group velocities estimated by the dispersion relation are twice as large as the velocity estimated from the propagation of wave packet, i.e., 17.5 sm day^{-1} in Term I and 7.3 sm day^{-1} in Term II (Figs. 3-9a and 3-9b). In Term II, the vertical group velocity is smaller than that in Term I. One reason for the difference of the vertical group velocity between the observation and the dispersion relation is that the horizontal wavelength and the vertical wavelength in Term II are both larger than that in Term I. The vertical group velocity estimated using Eqn. (25) in Term III is the largest among the three terms: 79.3 sm day^{-1}. During this term, the strong vertical shear is observed at 200–400 m depths (Fig. 3-5c). The wind energy is input continuously into the

ocean surface during this period (Fig. 3-3a). Therefore the near-inertial kinetic energy is

presumed to be transported efficiently by the large vertical group velocity. In Term III,

NIW frequency is $0.98f$, which is smaller than the local inertial frequency. This wave

cannot propagate the area, where RV is positive. Additional studies must be conducted to

elucidate the origin of NIW under the ACE.

3.4   Discussion

3.4.1   Reflection processes of NIWs

Numerous earlier studies addressed the reflection/penetration processes of waves

at solid boundaries (e.g. sea ground, lateral wall) and/or interfacial boundaries splitting

different media of fluid, e.g. the water surface that is adjacent to the air (Gossard and

Hooke, 1975; Smith, 1979). No report of the relevant literature describes a study

examining the propagation of internal waves at an "internal" boundary as they travel

towards an interface between different water masses. In this section, we pursue behaviors

of near-inertial waves that travel towards the interfacial plain splitting the upper

baroclinic eddy and the lower body of water (Fig. 3-15).

With respect to the general mechanisms of internal wave behaviors near an

internal boundary, a certain number of theoretical and observational studies (Byun et al.,

2010; Wunsch et al., 2014). Some have attempted to shed light on the reflection processes

of internal waves in the atmosphere, especially at the internal discontinuity of density

stratification (Gill, 1982). For example, Gill (1982) solved problems of the wave

reflection for the lee waves, which are formed in the stratified air behind mountainous

terrains when prevailing winds strike the topography. A simple two-layer situation is

considered, where N_n is assumed to be constant for each layer of $n = 1, 2$ n: the number

of the layer of interest.

We apply difficulties of atmospheric wave reflection to our oceanic situation,

with resolution of the vertical coordinate. We therefore consider a two-layer system of

seawater separating the upper part of TWC water and the lower part of JSPW. Especially

in the case of Term III, the NIW occurs within the ACE, where the potentially wind-

induced NIW propagates in the upper layer (Fig. 3-9c).

Wave propagation of four types can be considered depending on the stratification

in the two-layered oceanic system. In the upper two cases (Figs. 3-14a and 3-14b),

stratification is stronger in the upper layer. Whereas the stratification is stronger in the

lower layer in the bottom two cases (Figs. 3-14c and 3-14d). In the case of $N_n > \omega_{min}$, a

packet of internal waves can propagate. The former cases can assume a situation in which

jets and eddies exist in the surface layer. In the latter cases, we assume a situation in which

the SML develops in the upper layer.

Figure 3-15a portrays the vertical profile of σ_θ and $N(z)$ in the stretched

coordinate for Term III. We set an ad hoc boundary depth at $H = 300$ sm splitting the two

layers, based on the reflecting signatures of NIW (Fig. 3-15). In reality, it is common that

the seawater is stratified seamlessly in vertical sense (Fig. 3-15a). For convenience's sake,

we assume a two-layered ocean that consists respectively of $N_1 = 2.58$ cph and $N_2 = 0.74$

cph for the upper and lower layers. It must be emphasized that the buoyancy frequencies

of N_1 and N_2 are greater than f, so that the NIW can be propagative not only in the upper

layer but also in the lower layer (Fig. 3-14a). We designate this type of NIW propagation

across the interfacial boundary as "the penetration mode".

The band-passed ADCP current is separated into upward and downward

components so that it can clearly indicate the phase and energy propagation in a vertical

sense (Fig. 3-16). According to this procedure, results show that that the downward

component of the vertical shear dominates in the first half of the period, continuing until

February 28 (Fig. 3-16b), by contrast, the upward component is dominant in the latter

half (Fig. 3-16c). For convenience, we introduce a parameter of the "reflection rate" r,

which is defined with regard to the observed vertical shear of horizontal current as

$$r = \frac{|\boldsymbol{u}_z|_{\text{up}}}{|\boldsymbol{u}_z|_{\text{down}}}. \qquad (27)$$

Dimensionless parameter *r* is regarded as the relative strength of the upward-going wave to the downward-going counterpart, as represented in terms of vertical shear.

Figure 3-16a presents the time series of *r*, which is shown as a vertical average from the surface to 300 sm. The upward component exceeds the downward component as of 10:00 on February 27. Both components become significantly attenuated once it descends to depths greater than 300 sm. Thereby, the vertical propagation of NIW (represented by slanting phase lines) is not clearly confirmed in the deep layer (Figs. 3-16b and 3-16c). In this representation, it can be confirmed that the downward-going NIW coming from the surface is reflected at depths of 250–300 sm.

Figure 3-17 presents a schematic illustration for reflection and refraction of internal waves, as reported by Gill (1982). Refraction occurs at the boundary of two layers, with a certain angle, going downward in the lower layer (Fig. 3-17; Gill 1982). Provided that the wave frequency is fundamentally invariant in spite of the discontinuous density, the following relation is obtainable in terms of N and φ'.

$$N_1 \cos \varphi'_1 = N_2 \cos \varphi'_2 \qquad (28)$$

Therein, φ'_1 and φ'_2 respectively stand for the angles of wave propagation from the vertical for the upper and lower layers (Fig. 3-17). The subscript denotes the layer number. The vertical velocity of internal wave in uniform stratification takes the form of

$$w = w_0 \exp\big(i(kx + mz - \omega t)\big), \quad (29)$$

where w_0 stands for the amplitude of vertical velocity, $\boldsymbol{k} = (k, m)$ represents the two-dimensional wavenumber vector, consisting of the horizontal and vertical components, and ω is the wave frequency. According to Gill (1982), the wave formulation can be decomposed into upward-traveling and downward-traveling components. Vertical velocity w and perturbation pressure p' are expressed respectively as shown below.

$$w = w_1\big[\exp\big(im_1(z - H)\big) + r\exp\big(-im_1(z - H)\big)\big]\exp\big(i(kx - \omega t)\big) \qquad (30)$$

$$p' = \frac{m_1\omega\rho_0 w_1}{k^2}\big[-\exp\big(im_1(z - H)\big) + r\exp\big(-im_1(z - H)\big)\big]\exp\big(i(kx - \omega t)\big) \quad (31)$$

As a key point, we introduce the invariant quantity of "impedance", Z, that is unchanged irrespective of the rapidly change of N (Gill, 1982). In principle, Z can be expressed as a product of two independent variables of p' and w as

$$Z = p'/\rho_0 w = -\omega m/k^2. \qquad (32)$$

The right-most side of the equation derives from the substitution of (30) and (31). For each layer, Z can be derived as

$$Z_1 = \frac{\omega m_1}{k^2}\frac{-\exp\big(im_1(z-H)\big) + r\exp\big(-im_1(z-H)\big)}{\exp\big(im_1(z-H)\big) + r\exp\big(-im_1(z-H)\big)}, \quad (33)$$

$$Z_2 = -\frac{\omega m_2}{k^2}. \qquad (34)$$

From the invariant aspect of Z across the density gap, Z_1 and Z_2 must be identical at $z = H$. Therefore, reflection coefficient r can be represented as

$$r = \frac{m_1 - m_2}{m_1 + m_2}. \qquad (35)$$

We evaluate the vertical wavenumber in the lower layer observed in Fig. 3-18 from (35). The vertical wavenumber in the upper layer is already evaluated using vertical wavenumber rotary spectra (Fig. 3-12 and Table 3-2). Reflection coefficient r is calculable from the temporal average of vertical shear (Fig. 3-15c). The vertically averaged value between the surface and the boundary depth H is $r = 0.78$ (Figs. 3-15b and 3-15c). The value of $m_2 = 7.5 \times 10^{-4}$ (corresponding to $\lambda_2 = 5343$ m in an actual length) can be estimated for the lower layer. Apparently, it is smaller than the upper-layer wavenumber of $m_1 = 7.0 \times 10^{-3}$ ($\lambda_1 = 142$ sm, Table 3-2). The vertical wavelength in the lower layer is greater than the water depth at the mooring site, although the validity of that finding remains somewhat doubtful.

As depicted in Fig. 3-8, HKE for the near-inertial fluctuations, i.e. $\omega \sim f(\varphi)$, was high particularly at depths below the boundary depth ($H = 300$ sm; $\sigma_\theta = 27.2$). In Fig. 3-18c, the full vertical range of near-inertial velocity is shown for the original depth coordinate. We ascertain the certain strength of near-inertial oscillation over the large portion of water column residing underneath the boundary depth: the vertical structure of near-inertial current seems nearly barotropic, with nearly absent vertical variation.

We hypothesize that the vertical wavelength in the lower layer, as calculated

from the relation of (35), is explainable from the nearly barotropic nature of observed

near-inertial oscillation in the lower layer (Fig. 3-18c). The HKE in the upper layer varies

temporally, although that in the lower layer is constant over time (Fig. 3-18a). The

minimum value of HKE ratio between the upper and lower layer is 0.15 in Term III (Fig.

3-18b). The possible route of energy route can be attributable to the refraction process at

the pycnocline, segregating the eddy core and deeper waters, where it follows the

reflection of NIWs (Figs. 3-18a and 3-18b).

3.4.2　Resonant responses by wave reflection

The preceding subsection presented discussion of the shift of wavenumber m_1

at the discontinuity of N for the upper layer. The concept of wave decomposition into the

incident and reflected components was introduced as in Fig. 3-17, and Eqns. (30) and

(31). Superposition effects on the kinetic energy flux were examined. From Eqns. (30)

and (31), w and p' at $z = 0$ are found to be

$$w = w_1[\exp(-\mathrm{i}m_1 H) + r\exp(\mathrm{i}m_1 H)]\exp(\mathrm{i}(kx - \omega t)), \qquad (36)$$

$$p' = \frac{m_1 \omega \rho_0 w_1}{k^2}[-\exp(-\mathrm{i}m_1 H) + r\exp(\mathrm{i}m_1 H)]\exp(\mathrm{i}(kx - \omega t)). \qquad (37)$$

Vertical energy flux density F_z, irrespective of the vertical axis (Gill, 1982), is definable

with the boundary conditions of Eqns. (36) and (37) as

$$F'_z = \frac{1}{2}\mathcal{R}(p'w^*), \qquad (38)$$

where $\mathcal{R}$ represents the real component and an asterisk * denotes a complex conjugate.

With substitution of Eqns. (36) and (37) into Eqn. (38), the full expression for F'_z is

$$F'_z = -\omega m_2 \rho_0 w_0^2/2k^2/[1 + ((m_2/m_1)^2 - 1)sin^2 m_1 H], \quad (39)$$

where w and p' are transformed to trigonometric form by Euler's formula. According to Eqn. (39), the denominator consists of an important term of $sin^2 m_1 H$, which changes considerably depending on the number of a quarter wavelength $\left(\frac{1}{4}\lambda_1 = \frac{2\pi}{4}m_1^{-1}\right)$ over the vertical segment H between the surface ($z = 0$) and the lower boundary ($z = H$).

Figure 3-19 schematically displays two examples that provide a vast contrast from the combination of λ_1 and H. If the wavelength is close to an even integer of a quarter of H, then $sin^2 m_1 H = 0$ (Case A in Fig. 3-19). Actually, Eqn. (39) provides

$$F'_z = \omega m_2 \rho_0 w_0^2/2k^2, \quad (40)$$

while it is an odd integer, then $sin^2 m_1 H = 1$ (Case B in Fig. 3-19), so the equation becomes

$$F'_z = \omega m_1^2 \rho_0 w_0^2/2m_2 k^2. \qquad (41)$$

In the latter case with $m_1 > m_2$, F'_z is enhanced. According to the preceding subsection, m_1 and m_2 are, respectively, 7.5×10^{-4} and 7.0×10^{-3}. In the extreme condition of $m_2 = 0$, F'_z becomes infinite, which corresponds to "resonance".

In Fig. 3-20, the temporal evolutions of w and p' (Eqns. (30) and (31), respectively) are demonstrated for the two extreme cases of Fig. 3-19. Here, $w_0 = w_1 (z = 0)$. All constants used for the calculation are presented in Table 3-4. As anticipated from the configuration, w and p' show wave-like structures (Figs. 3-20 a-h). We used reflection rate $r = 0.78$ based on observations (Fig. 3-15). Consequently, the maximum amplitude of w and p' by superposition is 2 (Figs. 3-20e-h).

Based on the analytical solutions of Eqn. (39), Gill (1982) described that the resonance mechanism of interfered waves can be attributable to the situation of an odd integer of a quarter wavelength as a result of superposition of incident and reflected waves. Figure 3-21 displays the solution of (39) for F'_z as a function of vertical wavenumber m_1 in the upper layer. F'_z recurrently attains the extremal maxima exactly at a rate of twice every one wavelength. The magnitude of F'_z lead to huge differences between the two cases of Case A and Case B, respectively, as 2.7×10^{-3} and 2.3×10^{-1} (Fig. 3-21).

Amplification of the interference waves can occur because of the resonance depending on the vertical wavelength. The range of observed wavelength is 80–170 m for Term III (Table 3-2). It is addressed on the analytical solution by a blue bar. Thereby, one can readily observe the notable variation of F'_z, that is, attaining a maximum of 3.0×10^{-1} at $\lambda_1 = 170$ sm and a minimum of 5.5×10^{-3} at $\lambda_1 = 150$ sm.

3.5   Summary

We have examined wind-induced NIWs based on year-round horizontal current data obtained at the FATO mooring station off Sado Island in the eastern Sea of Japan (Fig. 3-1). Four hydrographic surveys and the mooring observation were conducted during 2019–2020 as the FATO project. The mooring system was made up by two sets of ADCP and the seven single-layer current meters, covering the upper 1200 m at full depth of 1770 m at 1 h intervals from June 2019 through June 2020 (Fig. 3-2).

The TWC and the mesoscale eddies constituted complex oceanographic structures in the upper 300 m around the mooring area (Figs. 3-3b and 3-4). The offshore branch of the TWC existed intermittently during the period from June through early September in 2019 (Figs. 3-3b and 3-4a). The mooring site was located near the center of the CE between October and December 2019 (Figs. 3-3b and 3-4b), while the ACE remained for the periods during January–May 2020 (Figs. 3-3b and 3-4c). The high-passed current velocity shorter than the local inertial period (=19 h) showed multiple internal wave signals generated by an atmospheric disturbance (Figs. 3-3a, 3-3c and 3-3d). We examined the three downward-propagating internal wave events with different mesoscale phenomena (Fig. 3-5). The RV and the current baroclinicity produced by these

mesoscale features influence the properties of internal waves (Figs. 3-3, 3-4 and 3-5). The vertical shear of the horizontal current velocity was extraordinarily large at depths between 150–350 m (Fig. 3-5c).

The HKE of current velocity showed a dominant peak around the local inertial frequency in the upper 1200 m throughout the mooring period (Fig. 3-8). The HKE ratio between the CW and the CCW motion indicates double inertial oscillation ($\omega = 2f$), but the nonlinearity was presumed to be small. Any constituent from the oceanic tide was negligibly small (Fig. 3-8). From the viewpoint of the HKE, the internal wave signals corresponded to the NIW (Figs. 3-3 and 3-5).

Multiple downward-propagation of wind-induced NIWs were observed clearly during the mooring period between 2019 and 2020. We examined the three downward-propagating NIW events with different mesoscale phenomena (Figs. 3-9). The remarkable NIW events were generated typically by fast-travelling cyclones in summer, and by relatively persistent outbreaks of northwesterly wind from the Eurasian continent in winter (Fig. 3-7). The vertical shear of the band-passed current velocity was strong at 200–300 sm inside the ACE in Term III: February 10–March 10 2020 (Fig. 3-9c). The amplification of NIW suggested to be occurred at depth near the bottom end of eddy's core. The NIW's vertical shear was strong at the surface and decreasing with depth inside

the CE in Term II: November 20 – December 20 2019 (Fig. 3-9b). All the three terms, the

gradient Richardson number Ri_g around the strong vertical shear suggest turbulent mixing

through the breakage of the NIWs by KH instability (Fig. 3-10). The wave properties of

NIWs, i.e., the wave frequency ω, and the group velocity C_{gz} and C_{gh}, were evaluated

based on a linearized dispersion relation for internal waves (Eqns. (24), (25), and (26)).

Horizontal wavelengths were estimated from the horizontal scale of wind curl τ (Fig. 3-

7). The vertical wavelengths were estimated from the vertical wavenumber rotary spectra

(Fig. 3-12) and EOF analysis of the vertical shear of the band-passed current velocity

(Figs. 3-9 and 3-13). The vertical group velocities C_{gz} were found to be 46.7 sm day^{-1} in

Term I and 33.5 sm day^{-1} in Term II (Table 3-3).

According to the time–depth plot of the vertical shear of the band-passed current

velocity in Term III (Fig. 3-9c), the iso-phase line slope changed from upward to

downward as of 10:00 on February 27. A simple two-layer system was regarded as

examining the reflection and the refraction of internal waves related to Gill (1982). The

reflection of the NIW was identified from depths of 250 and 300 sm (Figs. 3-15 and 3-

16). The reflection layer was the pycnocline between the TWC water and the JSPW (Fig.

3-15). Near-inertial oscillation was observed in the lower layer underneath the reflection

layer (Fig. 3-18c). The HKE in the lower layer had approximately 40% of HKE of the

upper layer (Figs. 3-18a and 3-18b). Results suggest that the vertically coherent near-inertial oscillation was generated from the wavelength change by wave refraction. The vertical wavelength in the lower layer was estimated from the reflection rate; the vertical wavenumber in the upper layers was 5343 m (Eqn. (35)). Also, vertical wavelength-dependent amplification of NIW in the upper layer was inferred (Fig. 3-21).
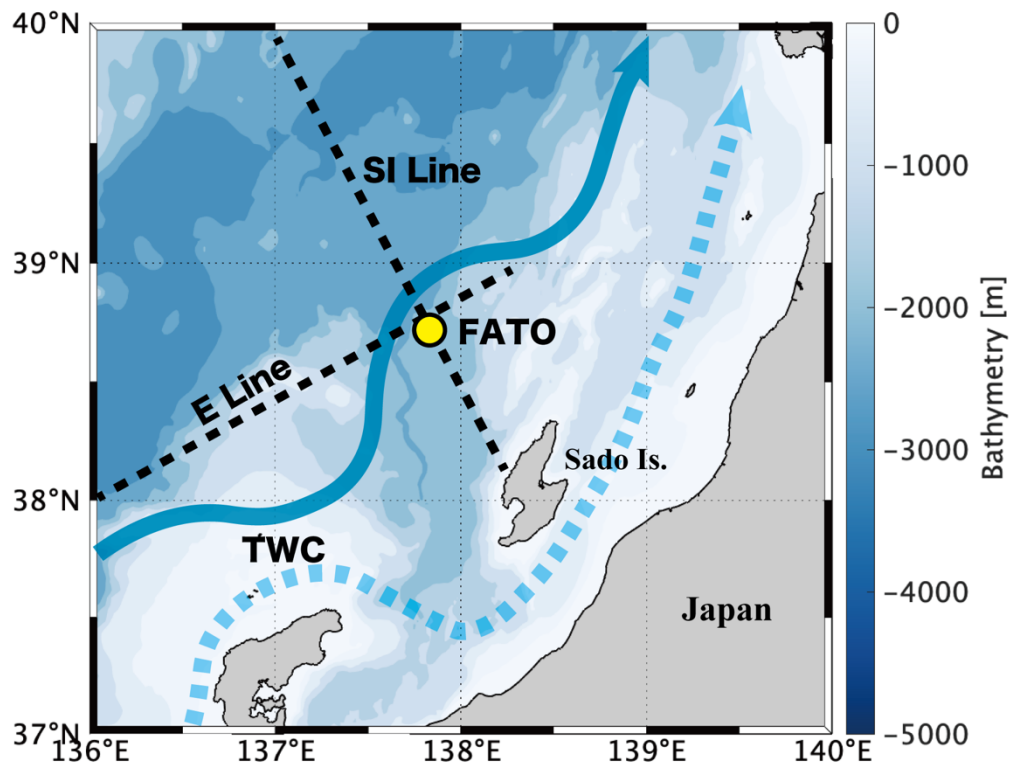
Fig. 3-1: Schematic map of the Tsushima Warm Current in the study area (blue arrows). The yellow circle represents the FATO mooring station. Black dashed lines show positions of hydrographic surveys. Blue shading represents bottom topography.
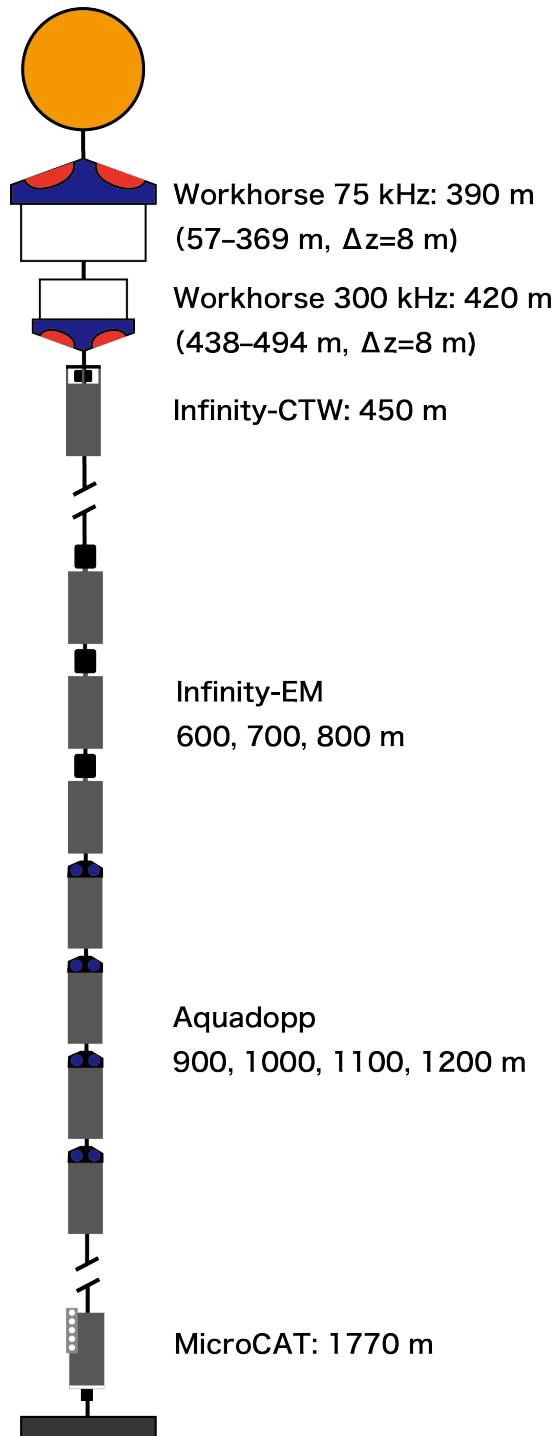
Fig. 3-2: Schematic illustration of the FATO station mooring system.
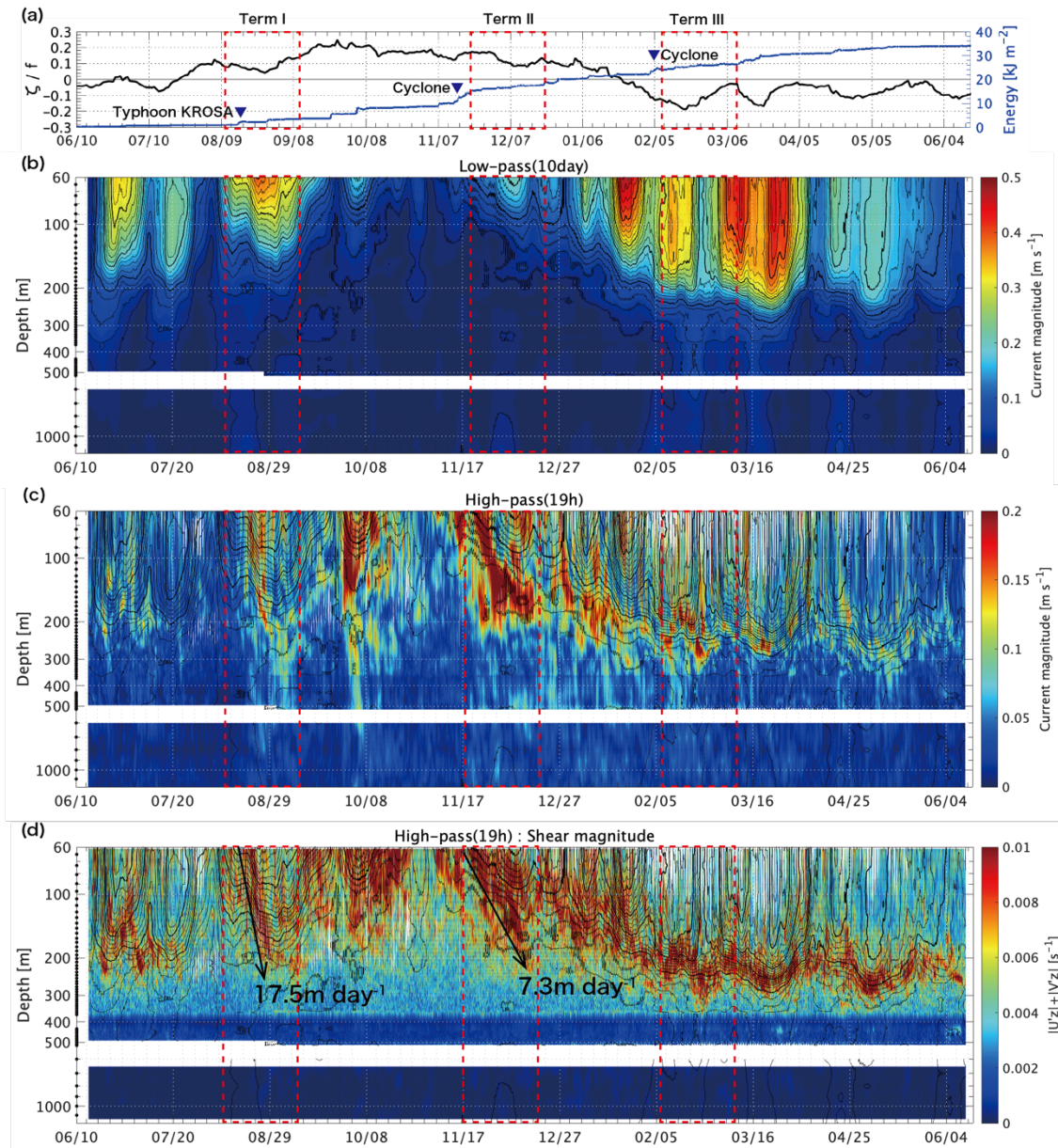
Fig. 3-3: Time series: (a) SSH-based RV ($\zeta_g/f(\varphi)$ Eqn. (4)); (b) geostrophic current magnitude estimated from a running mean over 10 days; (c) deviation from a running mean current magnitude of local inertial period (19 h); (d) vertical shear of current magnitude (c). Geostrophic current magnitude is superimposed in (c) and (d) with interval of 0.02 m s^{-1} (thin lines) and 0.1 m s^{-1} (thick lines). Black arrows and numbers indicate the migration of wave packets and their vertical group velocity. Black circles on the vertical axis in (b), (c), and (d) show the measurement depth of velocity data. The periods we examined are marked by a red box.
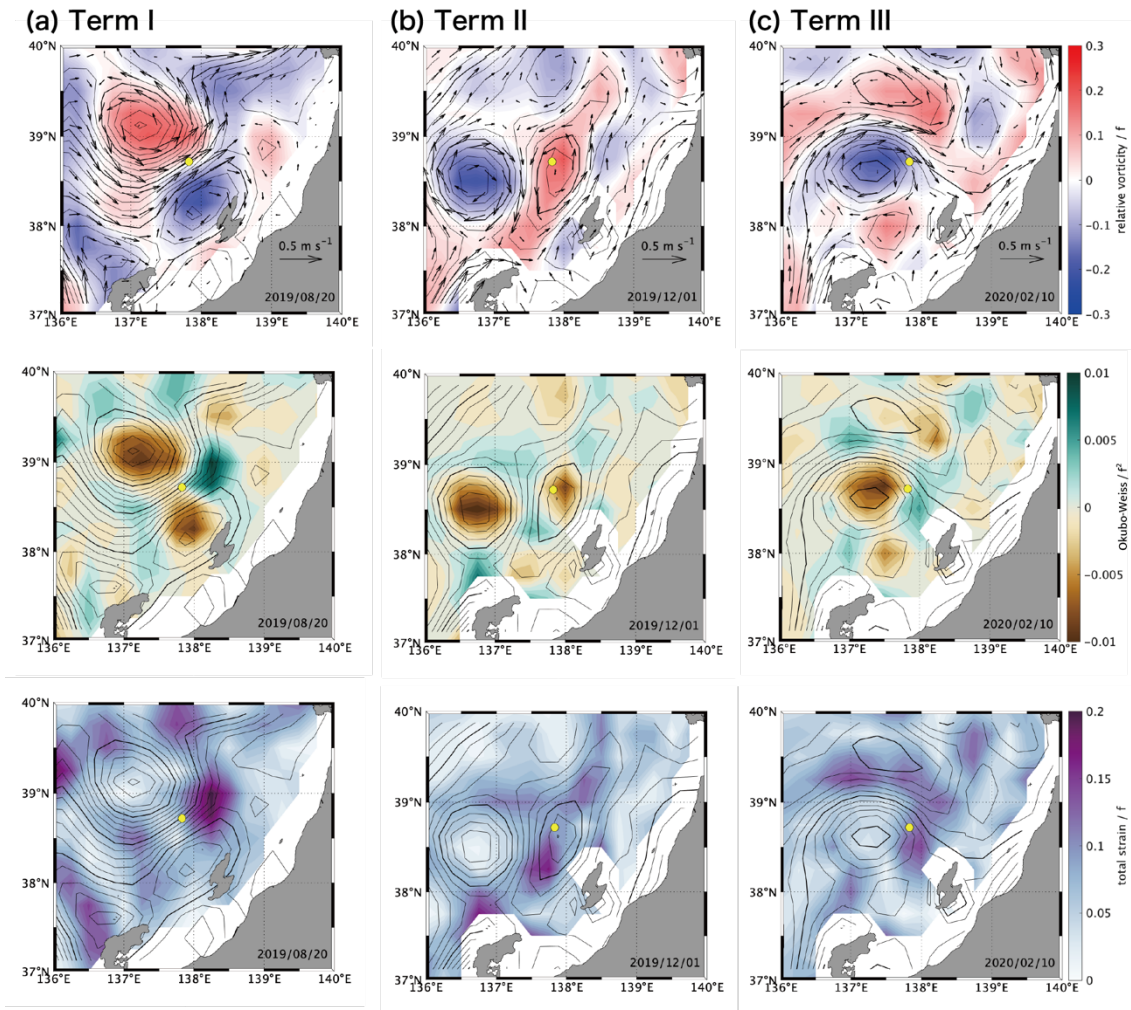
Fig. 3-4: Horizontal map of relative vorticity (ζ/f, upper panels), Okubo–Weiss parameter (middle panels), and total strain (lower panels) on (a) 20 August in Term I, (b) 1 December in Term II, (c) 10 February in Term III. In each panel, satellite-based SSH contours, with intervals of 0.02 m (thin lines) and 0.1 m (thick lines), are superimposed. SSH-based geostrophic currents are indicated by black arrows in the upper panels. Colored circles represent the mooring position FATO.
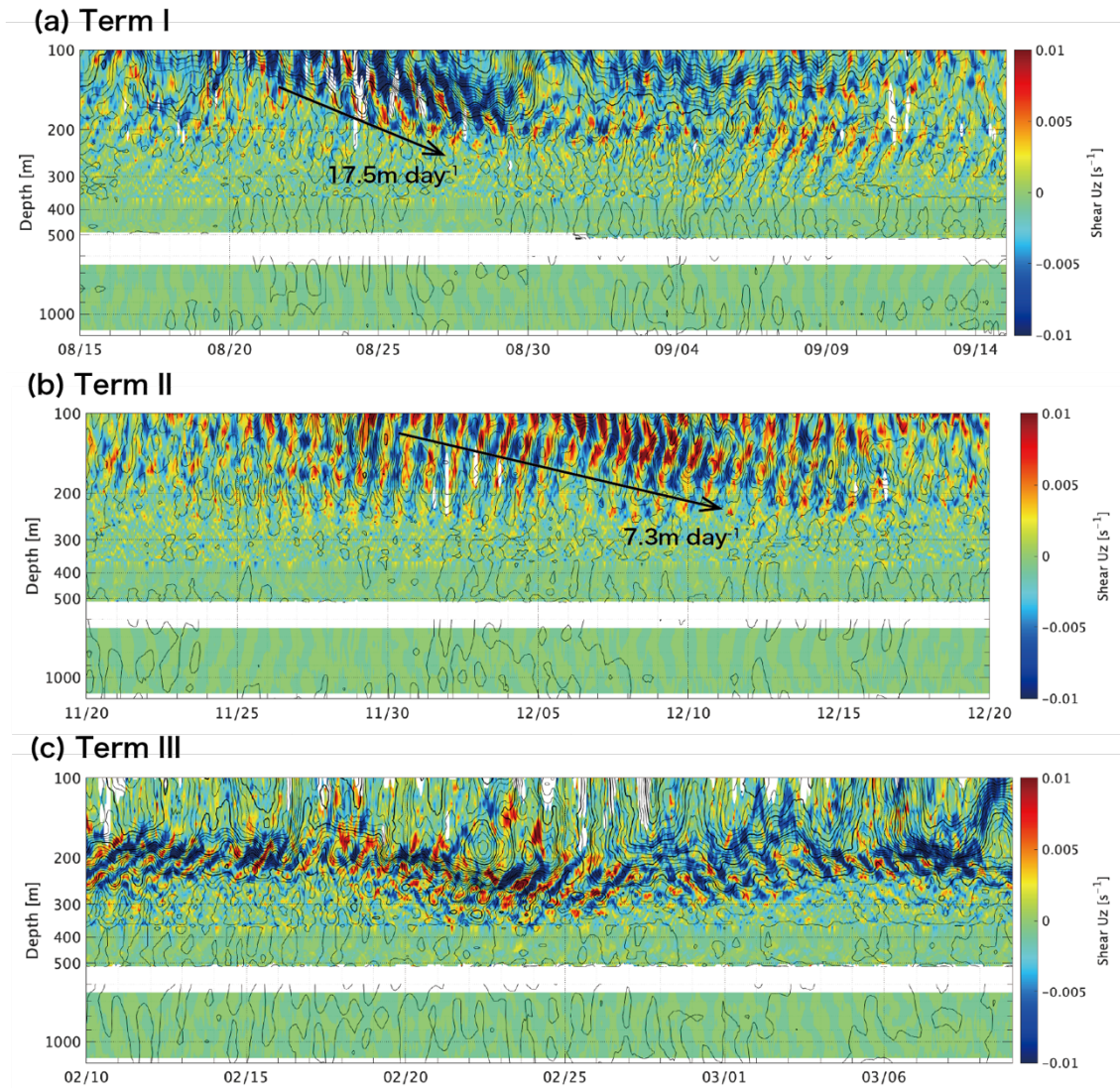
Fig. 3-5: Time series of vertical shear of eastward velocity (color) and 25-hr mean current magnitude (isolines) in three event terms. The contour interval is 0.05 m s⁻¹ for thin lines and 0.1 m s⁻¹ for thick lines. Black arrows and numbers show migration of the wave packets and their vertical group velocity.
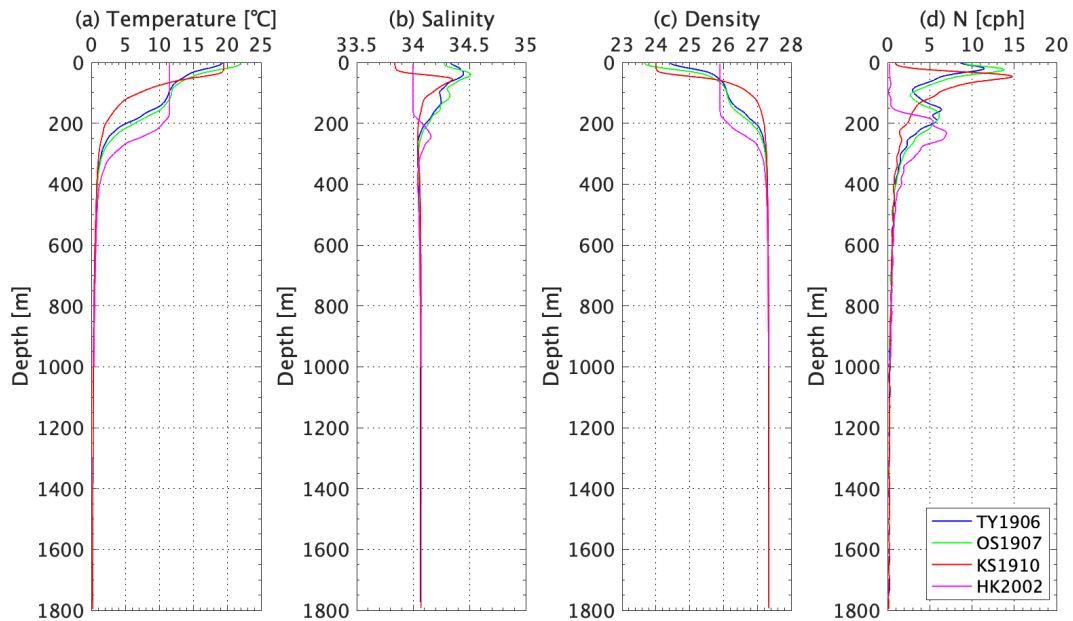
Fig. 3-6: Vertical profile of (a) in situ temperature (°C), (b) practical salinity, (c) sigma-T, and (d) buoyancy frequency $N(z)$ (cycle per hour: cph, Eqn. 2) at mooring position during the four cruises of TY1906, OS1907, KS1910, and HK2002. The cruises corresponding to Terms I, II, and III, are respectively OS1907, KS1910, and HK2002 (Table 3-1).

Table 3-1: MLDs estimated by the temperature profile from the shipboard CTD (Fig. 3-6) and the accumulated near-inertial kinetic energy (KE) inputs estimated by the slab model (Fig. 3-3a, Section 3.3.4). The MLD is determined as depth where the temperature difference from that at 5 m deep exceeds 0.25 °C. The CTD profiles of the nearest cruise date are used for the MLD calculation (Fig. 3-6).

Term	Cruise	MLD [m]	KE input [kJ m^{-2}]
I	OS1907	12	1.41
II	KS1910	35	2.37
III	HK2002	176	1.81
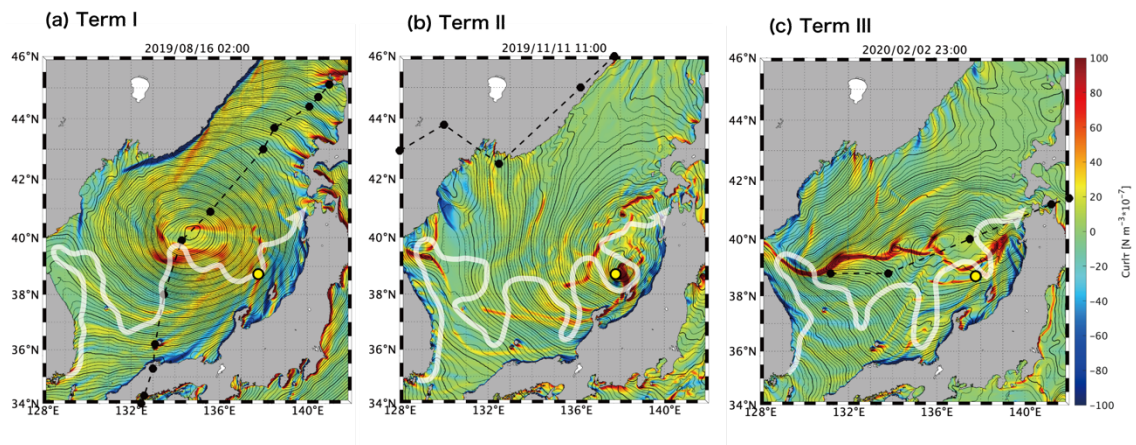
Fig. 3-7: Horizontal map of sea level pressure (isolines) and wind stress curl τ (colors, Eqn. (19)) in (a) August 16, (b) November 11, and (c) February 2. The contour interval is 0.2 hPa for thin lines and 1.0 hPa for thick lines. Black circles with a broken line show the typhoon or cyclone trajectories. White curves show the offshore north current of TWC in each term. Yellow circles show the mooring position.
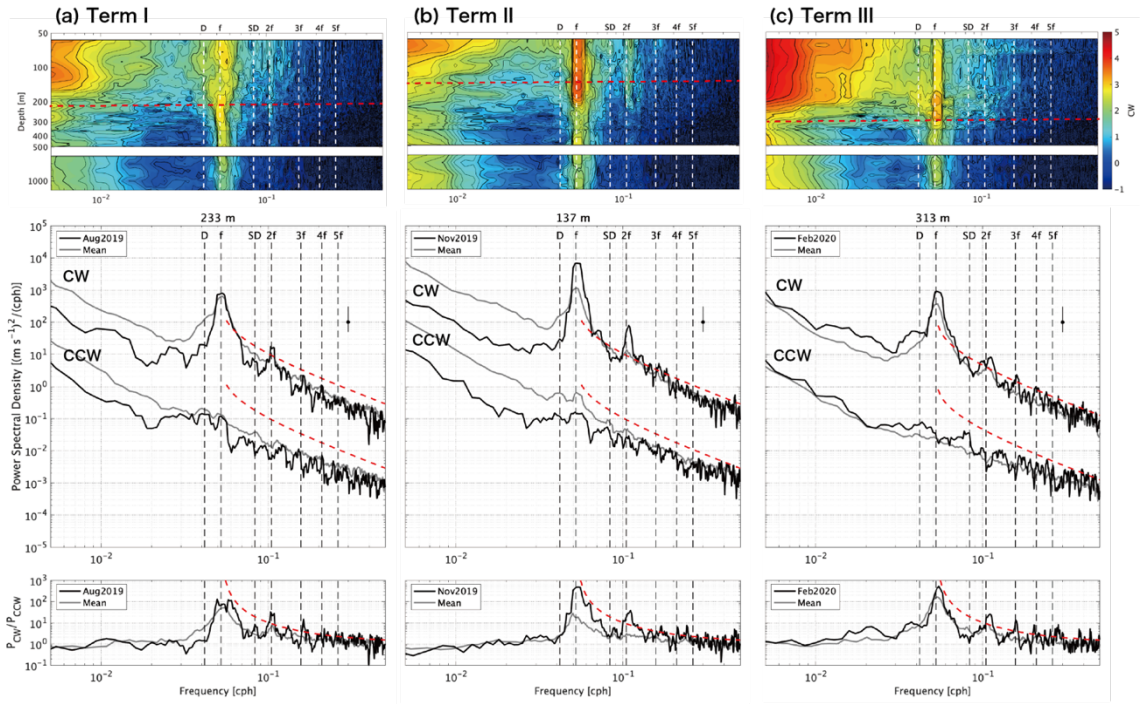
Fig. 3-8: Rotary frequency spectrum for horizontal current at 233 m, 137 m, and 313 m depth for (a) Term I (August 15–September 15, 2019), (b) Term II (November 20 – December 20, 2019), and (c) Term III (February 10 – March 10, 2020). The gray curve in each figure shows the annual-mean spectrum (June 15, 2019 – June 15, 2020). The red dashed curve shows the GM75 spectrum. CCW component are lower by 100 times for display. A ratio of kinetic energy between CW and CCW are shown in the lower panel, where a canonical curve of the linear internal wave theory is shown for the reference (red, dashed curve, Eqn. (20)). Vertical dashed lines show multiple inertial frequencies of f to $5f$ and diurnal and semi-diurnal frequency. In upper panels, the vertical bar denotes the 95% confidence interval.
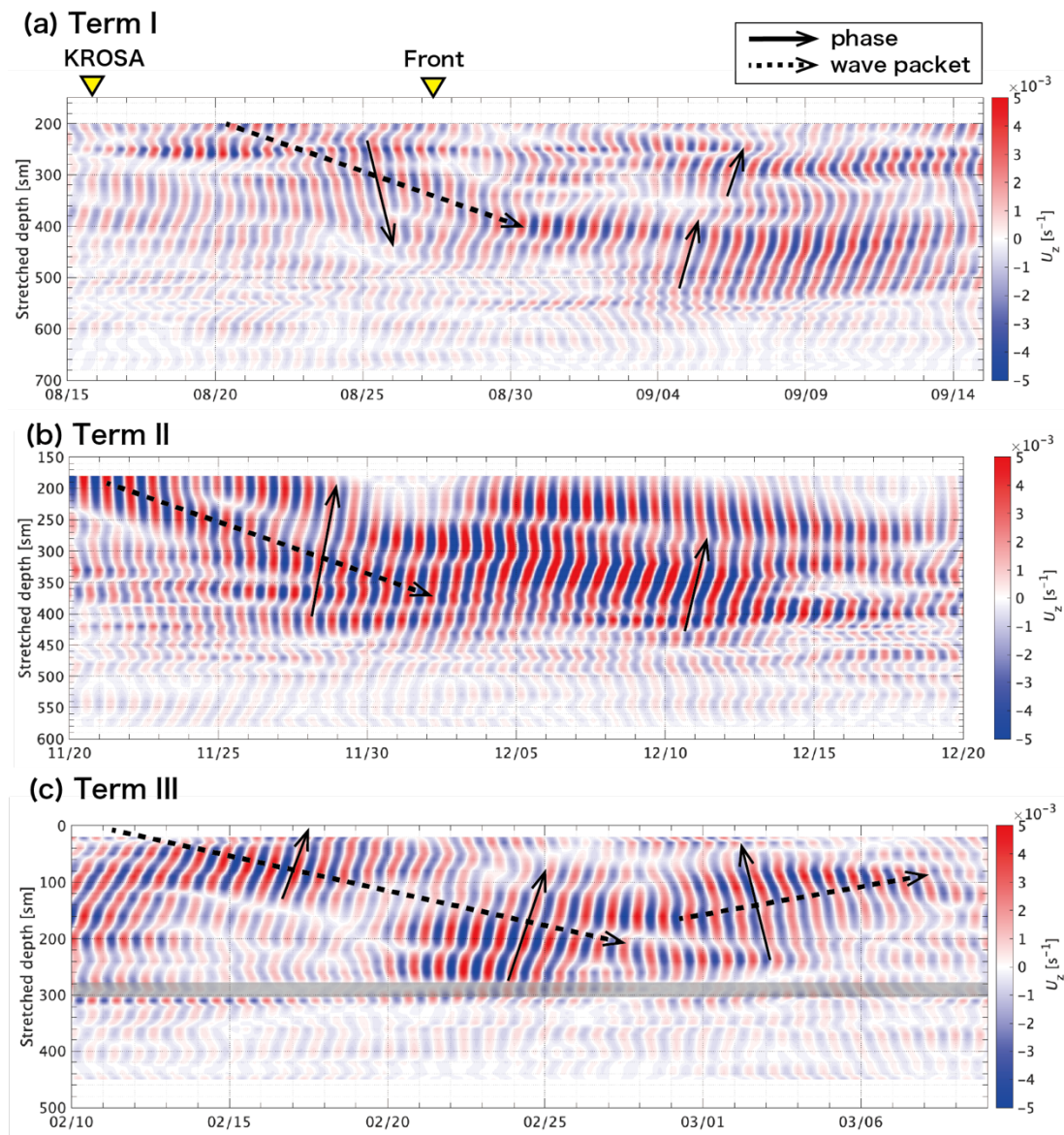
Fig. 3-9: Time series of the eastward vertical shear in (a) Term I, (b) Term II, and (c) Term III, which is a band passed around f (0.9–1.1f). Shear magnitude is scaled by $N_0/N(z)$. The WKB stretching is applied to vertical axis z* with a unit of stretched meter (sm) (see Section 3.3.3). Yellow triangles represent the passage date of the typhoon KROSA and the front at the FATO mooring site. Solid and broken arrows respectively specify the iso-phase line and wave packet propagation. The gray hatched area implies the reflection depth.
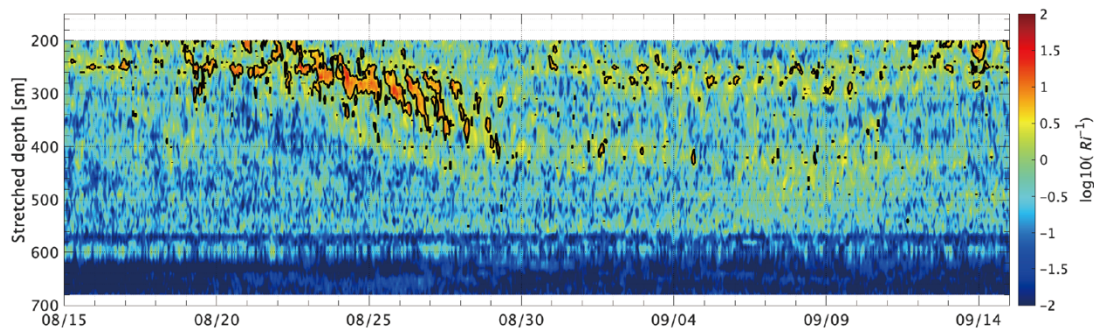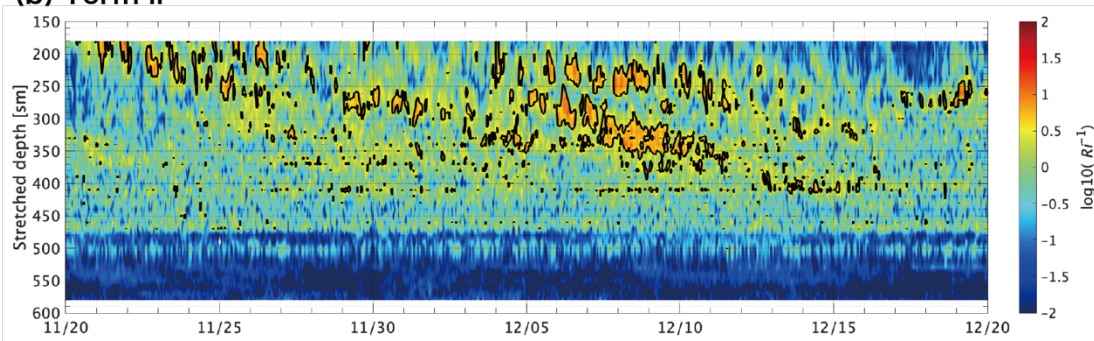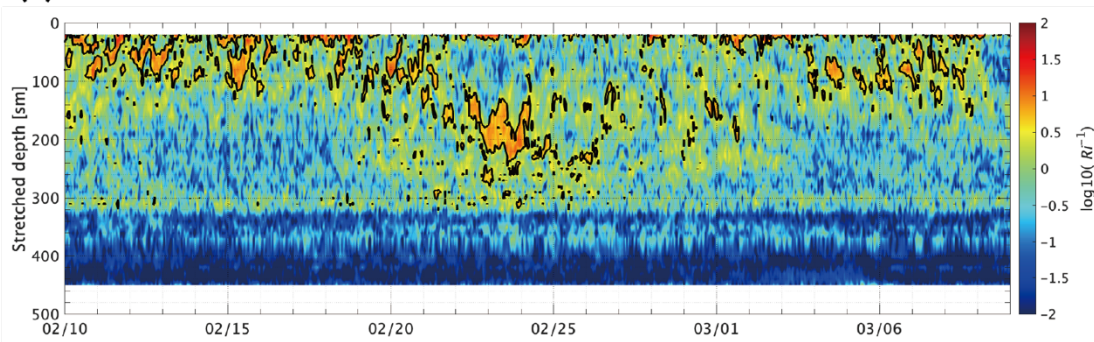
Fig. 3-10: Time series of Richardson number (Ri_g^{-1}, Eqn. (7)) in (a) Term I, (b) Term II, and (c) Term III. Empirical threshold for wave breaking, i.e., $Ri = 0.25$ ($Ri^{-1} = 0.6$), is delimited by black contours.
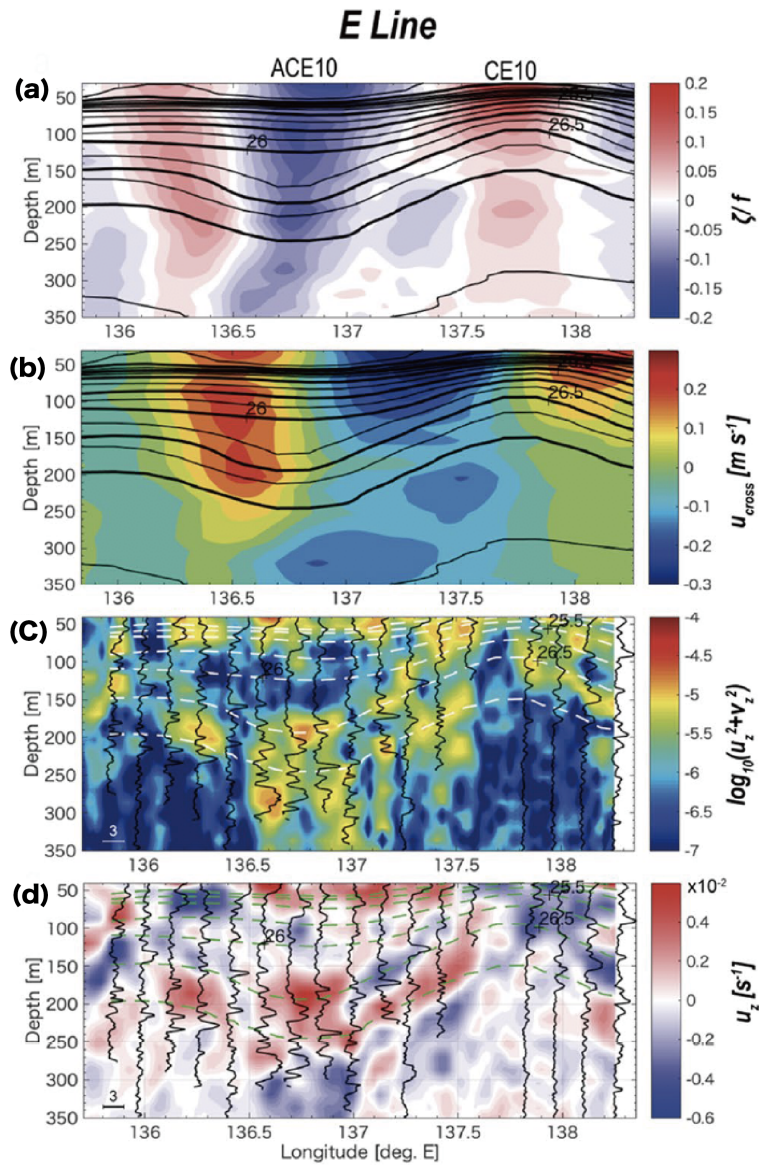
Fig. 3-11: Vertical sections along E line (Kawaguchi et al., 2021): (a) f-normalized relative vorticity anomaly; (b) horizontal normal velocity, where northward and northwestward give, respectively, positive values; (c) squared vertical shear of horizontal velocity, presented on a logarithmic scale; (d) vertical shear of back-rotated zonal velocity. Contour lines denote σ_θ, with respective intervals of 0.25 and 0.50 kg m^{-3}. In (c) and (d), vertical profiles of log10 ε from turbulence observations are overlain (see horizontal bars for a reference scale). The location of E line is shown as a black dotted line in Fig. 3-1.
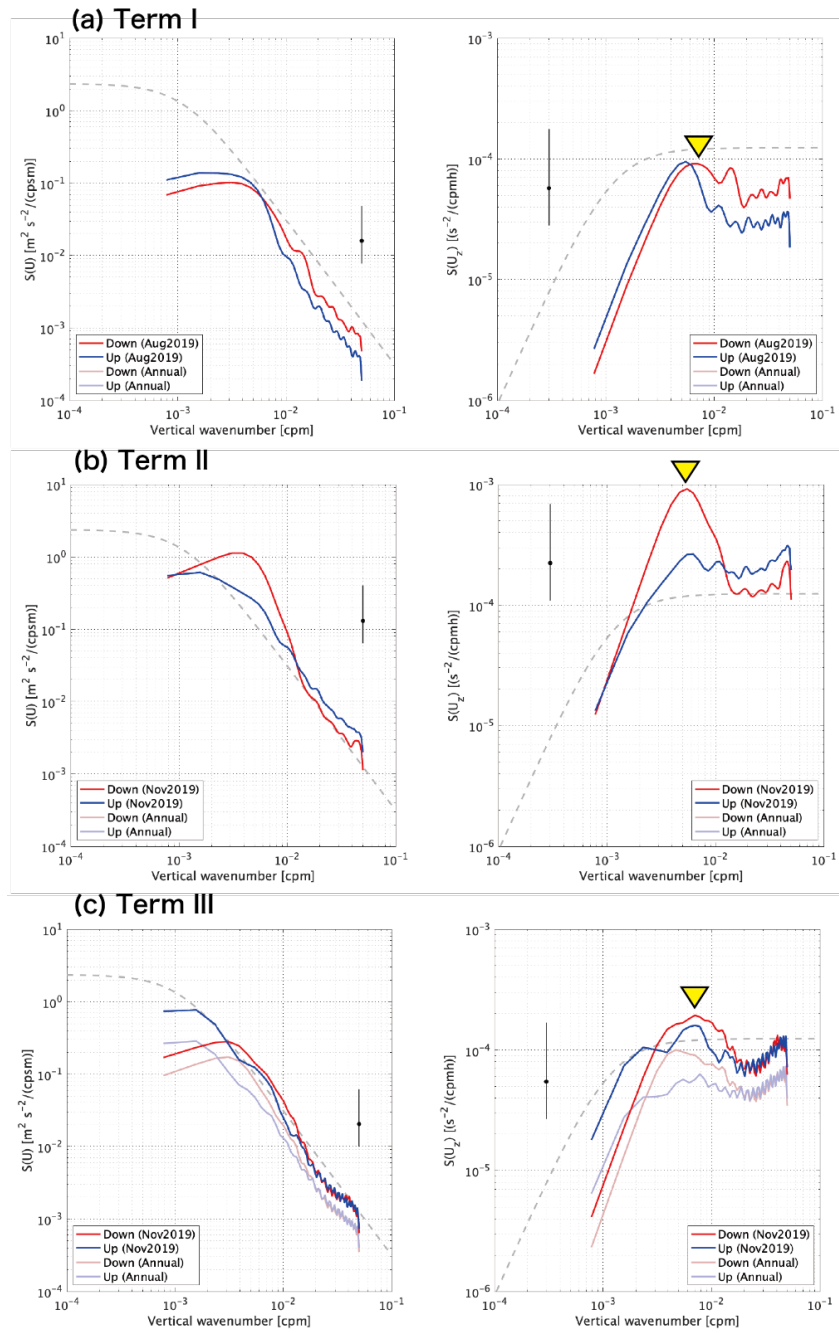
117

Fig. 3-12: Vertical wavenumber rotary spectra of band-passed horizontal velocity (left panels) and vertical shear (right panels) for the near-inertial oscillations in (a) Term I, (b) Term II, and (c) Term III. Downward and upward components are represented respectively as red and blue lines. Results for the annual mean are shown by pale-colored lines in the figures. Dashed curves show the canonical curve of GM75. The yellow triangles represent the prominent vertical wavenumber in each term presented in Table 3-1.
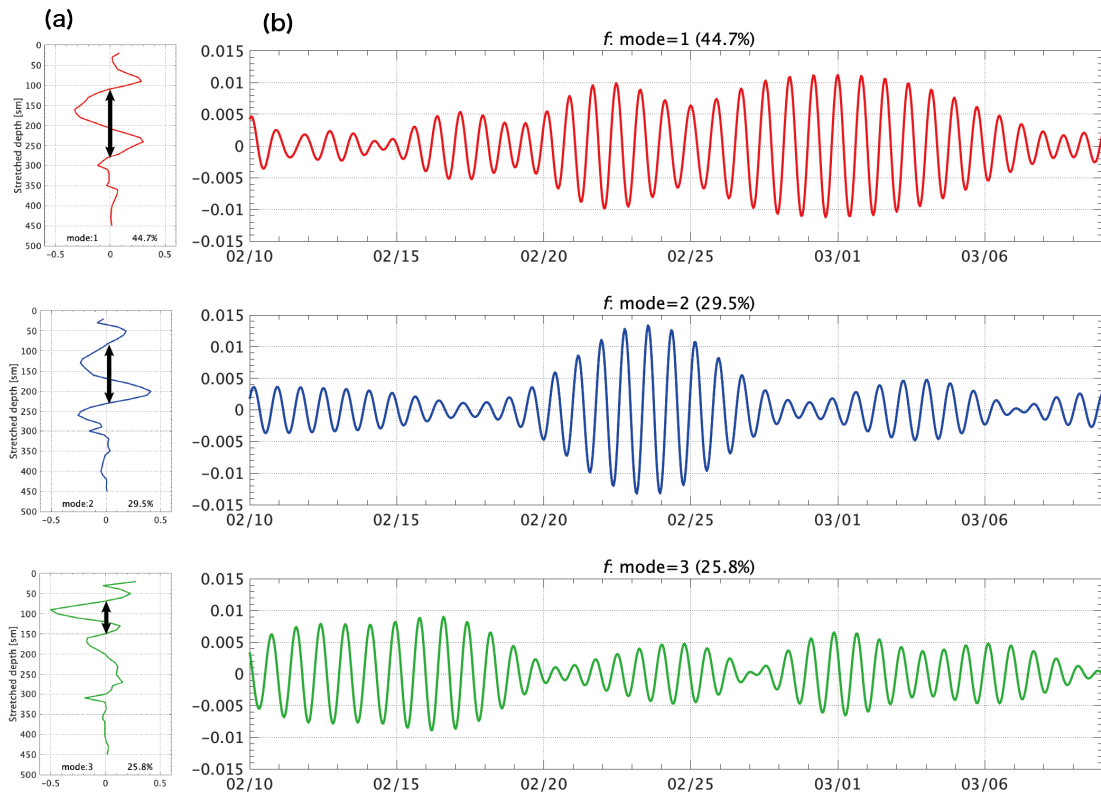
Fig. 3-13: (a) Vertical profiles for the first three EOF modes and (b) time series of normalized amplitude in Term III. Black arrows indicate the determined wavelength. Rates of contribution to the variance are indicated at the top of the figures.

Table 3-2: Vertical wavelength of band-passed velocity around f by EOF analysis (black arrows in Fig. 3-13a) and the vertical wavenumber rotary spectra (yellow triangles in Fig. 3-12). Mean values were calculated considering the normalized variances.

Term	λ_v [m]				
	EOF analysis				Shear spectrum
	Mode 1	Mode 2	Mode 3	mean	
I	190	170	80	158	142
II	260	270	100	240	183
III	170	150	80	141	142

Table 3-3: NIW properties estimated from the dispersion relation for linear internal waves, i.e. internal wave frequency ω, and vertical and horizontal group velocity C_{gz} and C_{gh} (Eqn. (24), (25), and (26)). Horizontal wavelength λ_h is determined from the horizontal scale of wind curl τ (Fig. 3-7, Eqn. (19)). Vertical wavelength λ_v is estimated from vertical shear rotary spectra (Fig. 3-12, Table 3-2). Effective Coriolis frequency f_{eff} is estimated from the local Coriolis frequency $f(\varphi)$ (Eqn. (1)) and the relative vorticity ζ_g (Eqn. (4)).

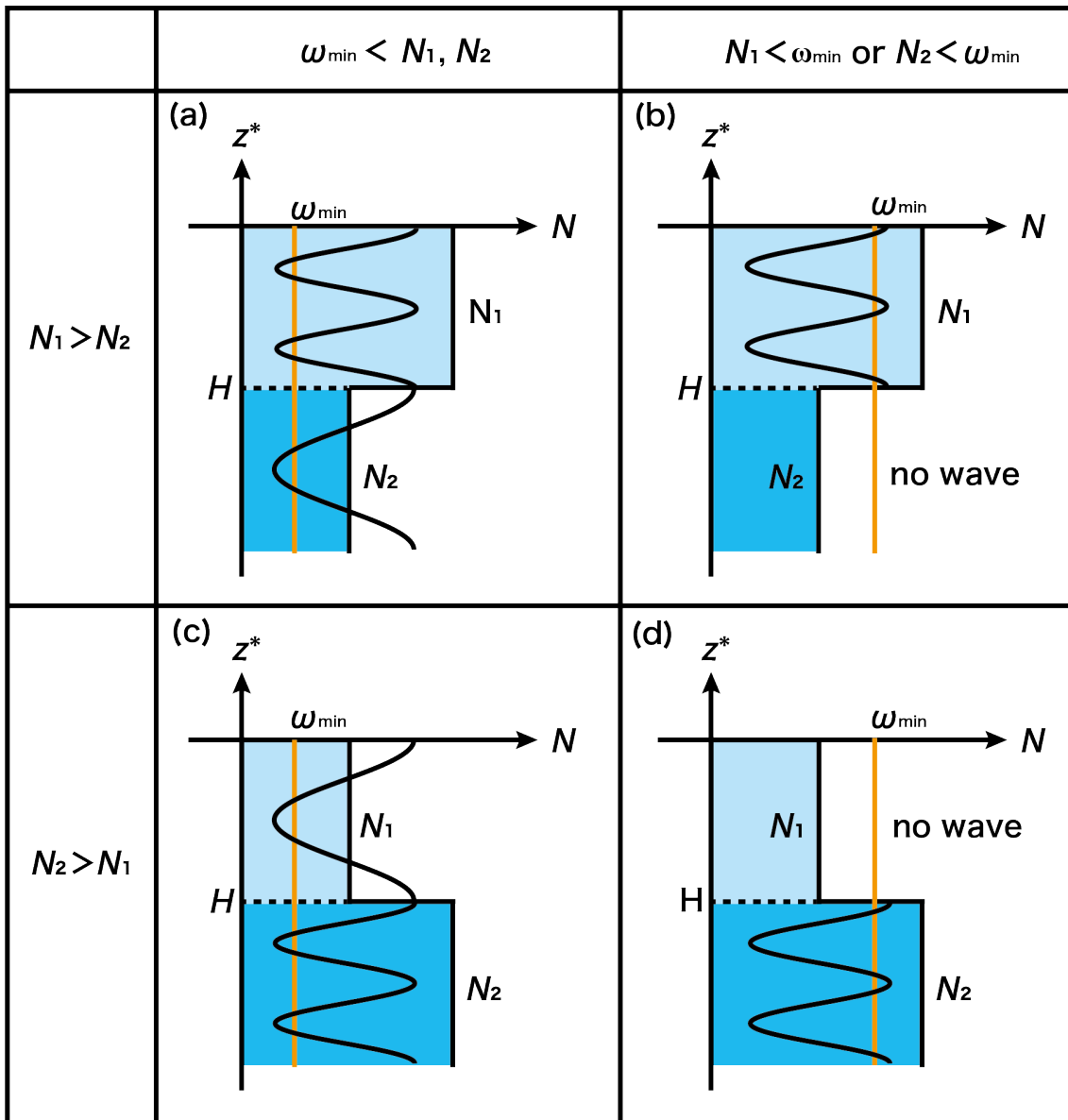| Term	λ_h [km]	λ_v [m]	f_{eff}/f	ω/f	C_{gz} [m day^{-1}]	C_{gh} [m s^{-1}]
I	39.5	142	1.05	1.08	46.7	0.15
II	68.6	183	1.08	1.10	33.5	0.15
III	37.1	163	0.95	0.98	79.3	0.21
reference	Fig. 3-7, Eqn. (19)	Fig. 3-12, Table 3-2	Eqn. (3)	Eqn. (24)	Eqn. (25)	Eqn. (26)

Fig. 3-14: Schematic diagrams of wave propagation in the two-layered system, where N_1 and N_2 respectively represent upper and lower stratifications, $\omega_{\min}$ is the minimum frequency of NIW. Internal waves can propagate when $\omega_{\min}$ is less than N_n (n=1,2). Vertical wavy lines represent the existence of internal waves at the layer.
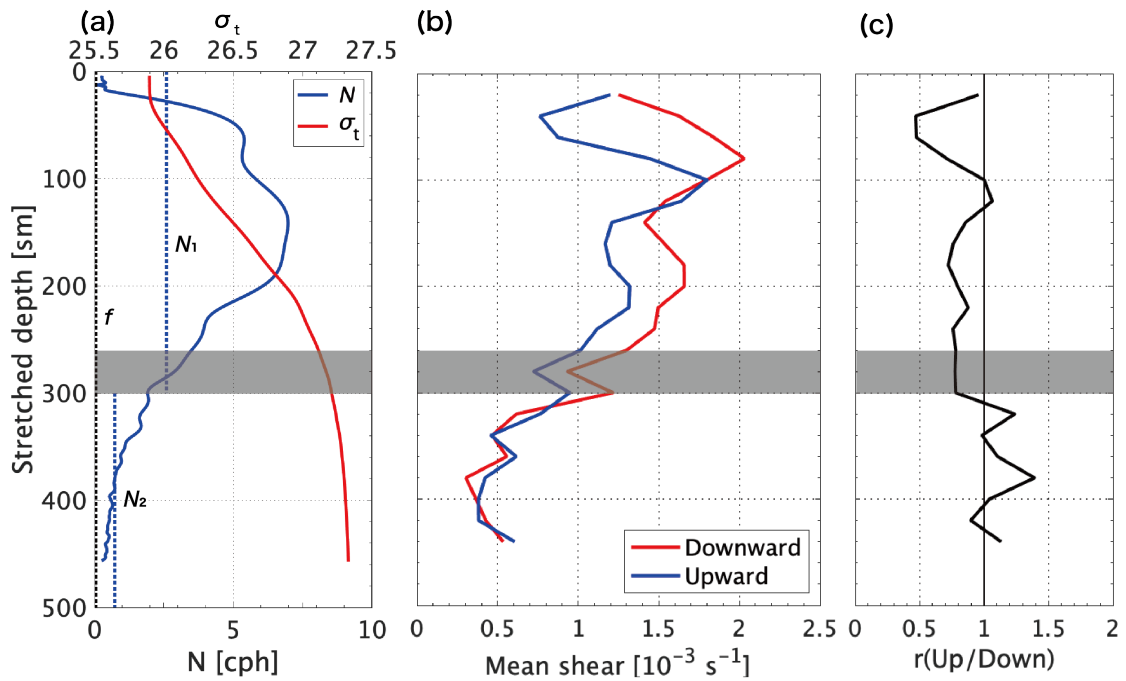
Fig. 3-15: (a) Vertical profiles of σ_t and $N(z)$ at the mooring site, for which a CTD profile was obtained during the HK2002 cruise, (b) time-averaged vertical shear magnitude of downward (red curve) and upward (blue curve) in Term III, and (c) the reflection coefficient r (see Eqn. 23) as the ratio between downward and upward shear in (b).
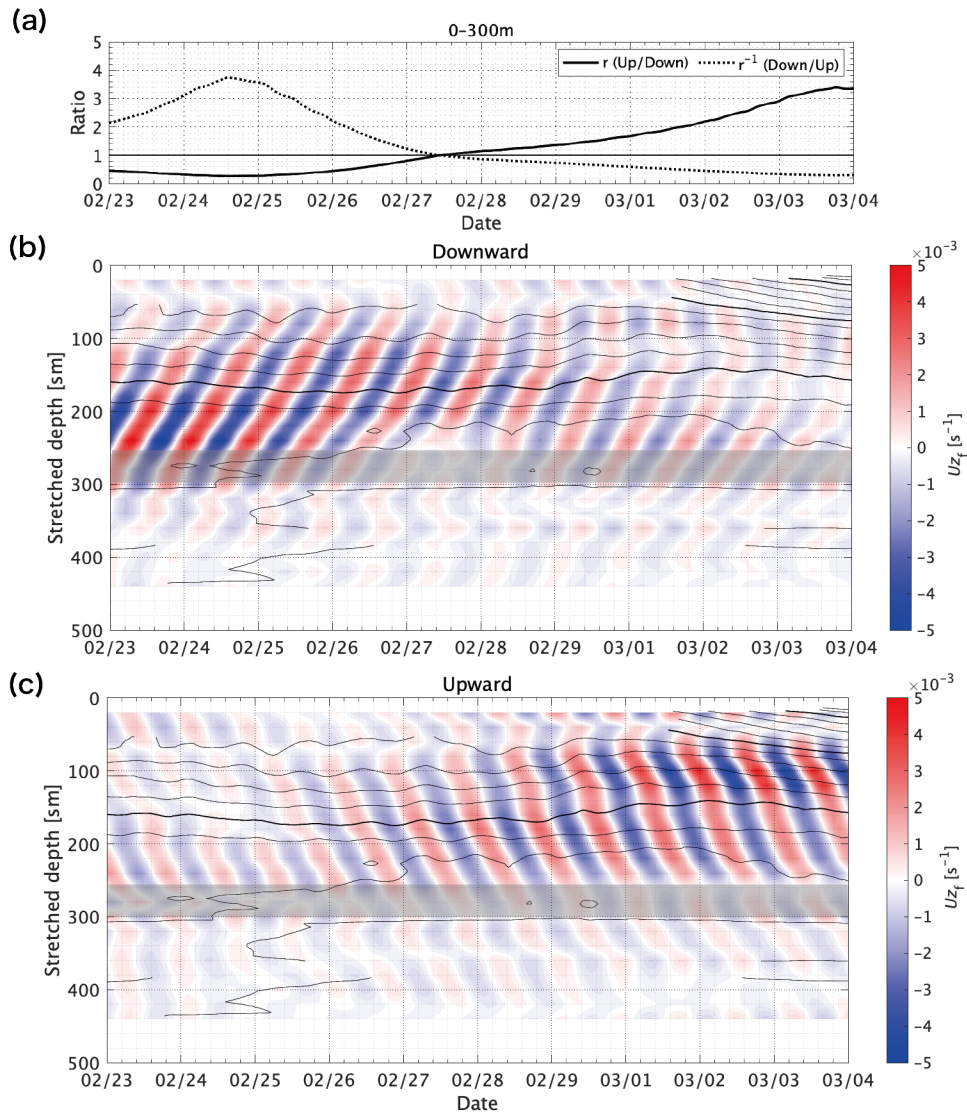
Fig. 3-16: Decomposition of near-inertial vertical shear for Term III: (a) the reflection ratio *r* (see Eqn. (27)), (b) downward and (c) upward components of the group velocity from zonal velocity, which is band-passed for $\omega = 0.9$–$1.1f$. Contour represents the geostrophic current magnitude averaged over 10days, whose interval is 0.02 m s^{-1} for thin lines and 0.1 m s^{-1} for thick lines. In (a), *r* is shown as an average for depths between 0 sm and 300 sm.
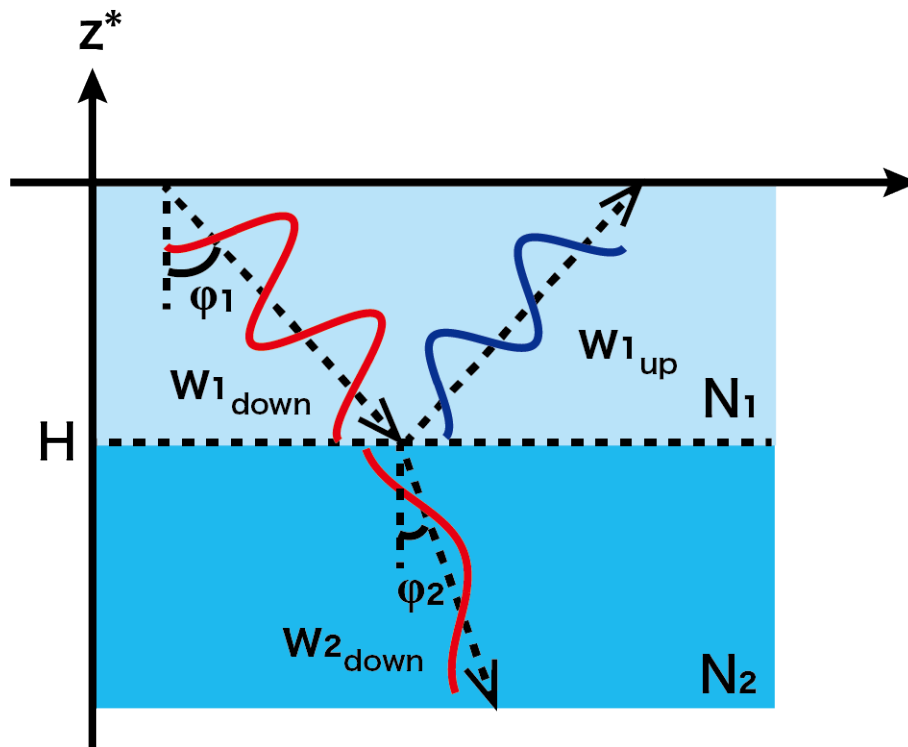
Fig. 3-17: Schematic illustration of reflection and refraction of internal waves in a two-layer system. The configuration for atmospheric lee waves (Gill, 1982) is modified to be applicable to the oceanic case with an anti-cyclonic eddy in the upper layer.
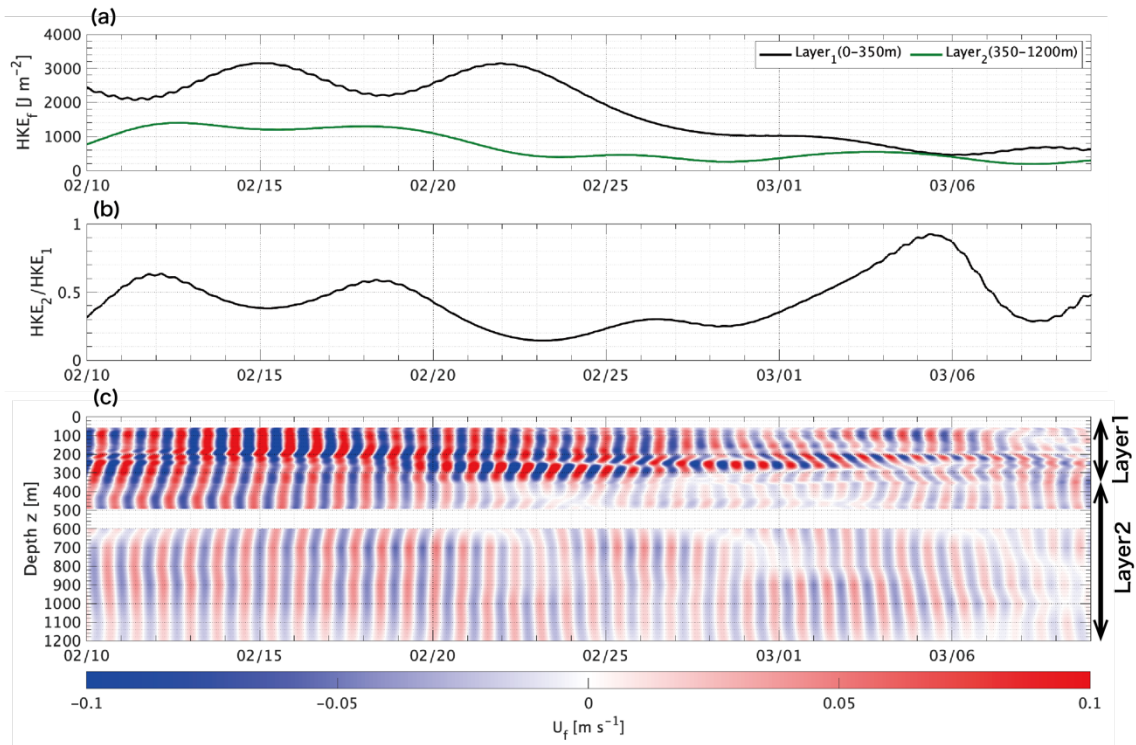
Fig. 3-18: Time series of (a) accumulated values of HKE for the upper layer of 0–350 m (black) and the lower layer of 350–1200 m (green), (b) ratio of HKE between the upper and the lower layer, and (c) near-inertially band-passed eastward velocity.

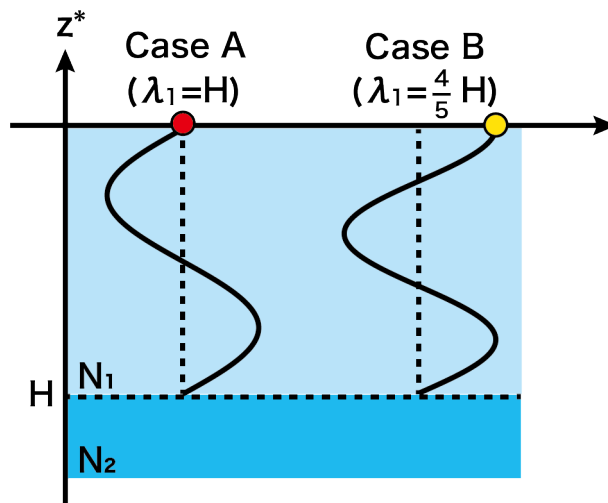Fig. 3-19: Schematic diagram depicting the relation between boundary depth H and vertical wavelength λ_1. In Case A, the vertical wavelength λ_1 equal to the surface. In Case B, the vertical wavelength $\lambda_1 = \frac{4}{5}H$. In Case A, the node of the wave corresponds to the surface (red circle), while in Case B the peak of the wave corresponds to the surface (yellow circle).
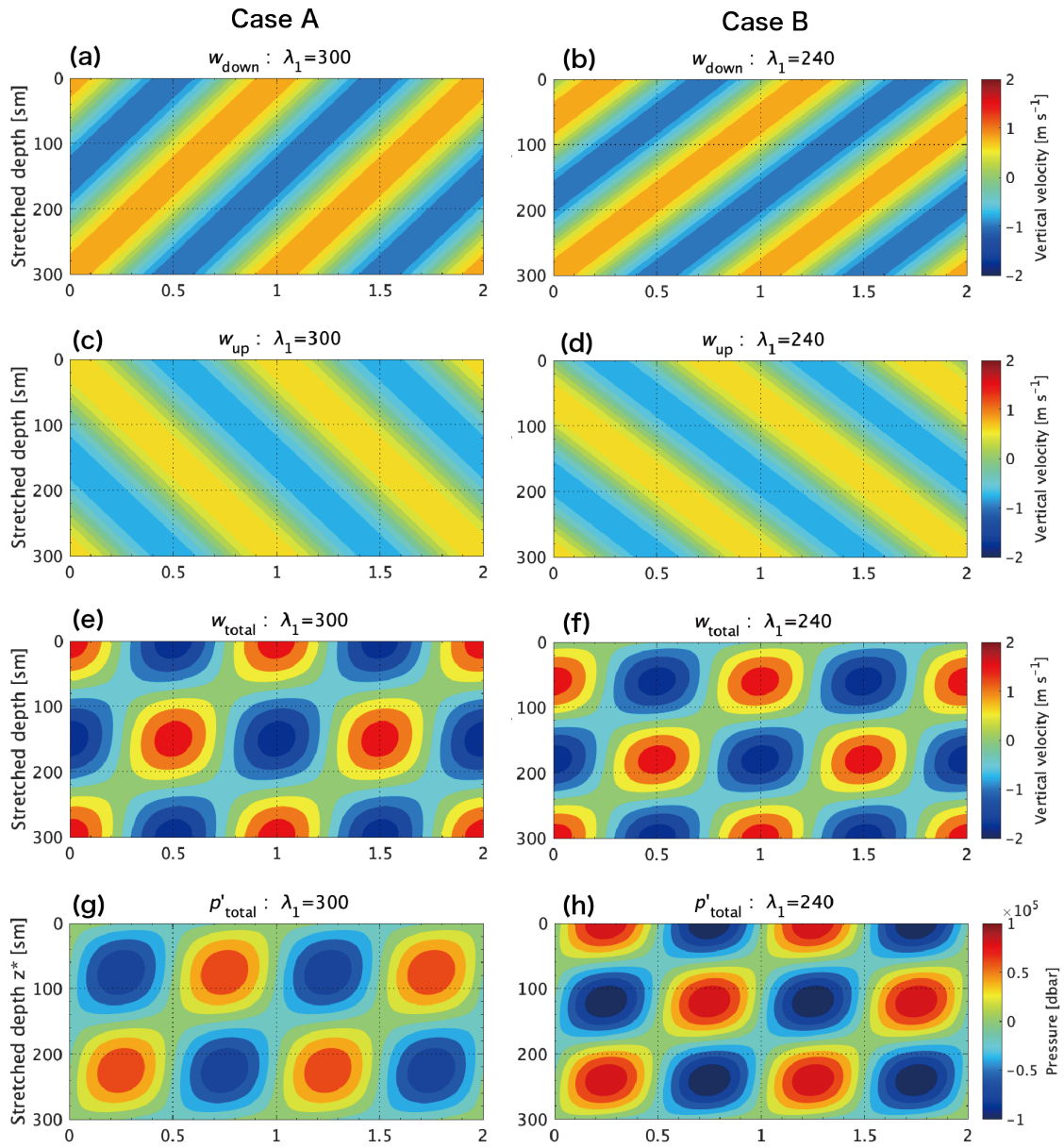
Fig. 3-20: Time–depth plot in case A (left panels) and case B (right panels). The vertical velocity of (a), (b) upward propagating component (first term of Eqn. (30)), (c), (d) downward propagating component (second term of Eqn. (30)), (e), (f) superposition of both components, (g), (h) pressure perturbations (Eqn. (31)) are shown.

Table 3-4: Parameters used for the calculation of vertical energy flux density $F'z$, i.e., boundary depth of two-layer system H, reflection coefficients r, local Coriolis frequency f, seawater density ρ_0, amplitude of vertical velocity w_0, horizontal wavelength λ_h, and vertical wavelength in the upper layer λ_1.

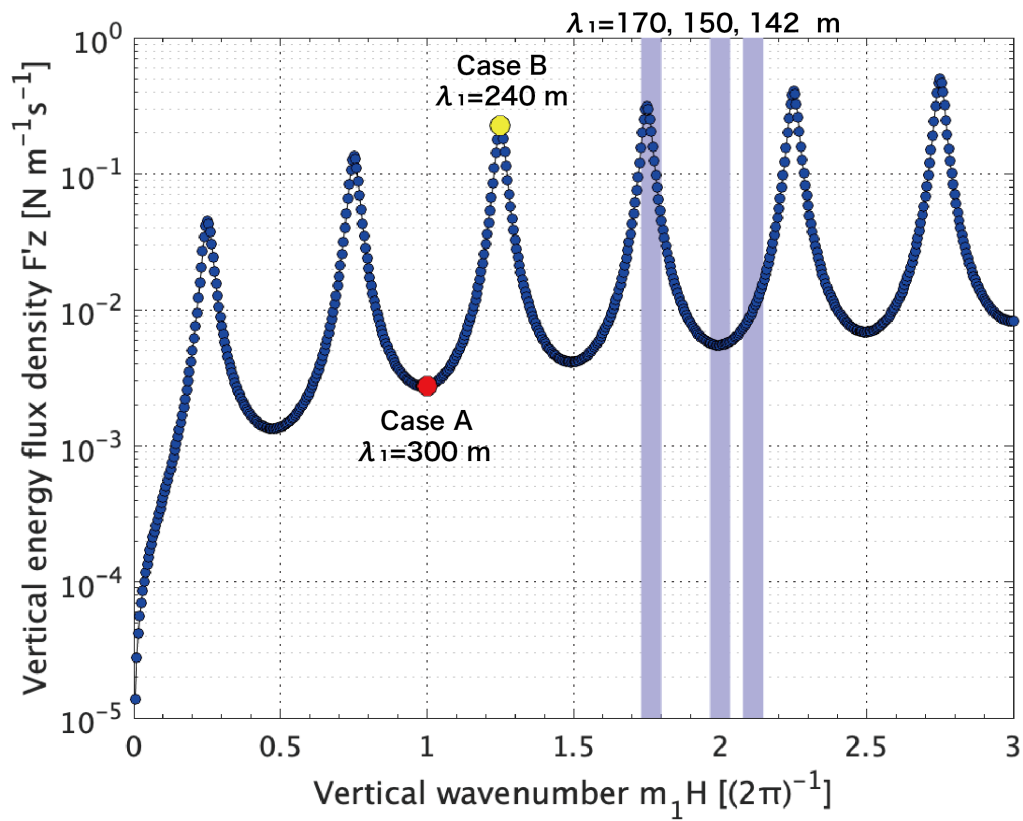| Parameter	Value	Reference
H [m]	300	Fig. 3-15
r	0.78	Fig. 3-15, Eqn. (35)
f [s^{-1}]	9.123×10^{-3}	
ρ_0 [kg m^{-3}]	1025	
w_0 [m s^{-1}]	1.0×10^{-3}	
λ_h [m]	30×10^3	Fig. 3-7
λ_1 [m]	300	Case A
	240	Case B
	170, 150, 142	Table 3-2

Fig. 3-21: Vertical energy flux density *F'z* (Eqn. (39)) at reflection rate *r* = 0.78 (Eqn. (35)) and $w_0 = 1 \times 10^{-3}$. Colored circles represent the *F'z* in Case A (red) and Case B (yellow), illustrated in Fig. 3-18. Blue shading shows the vertical wavelength of NIW, 170, 150, and 142 sm (Table 3-2).

4. General conclusions

Humans use the ocean for a variety of purposes, including eating habits, transportation, energy resources, and leisure. Familiar phenomena to our life have various spatiotemporal scales such as waves, tides, currents, storm surges, tsunamis, and sea level rise due to global warming. In particular, the ocean is important for us because Japan is surrounded by the Pacific Ocean, the Sea of Japan, the Sea of Okhotsk, and the East China Sea. Various phenomena in the multiscale structure (Fig. 1-3) exists in the Sea of Japan, and a comprehensive study is required to understand themselves and their interactions precisely. In this thesis, we focused on the essential features in the Sea of Japan, such as the Tsushima Warm Current (TWC), the Subpolar Front, mesoscale eddies, inertial oscillation, and internal gravity waves.

In Chapter 2, we developed the algorithm to determine the TWC pathway, which is the main current in the surface layer in the Sea of Japan. We clarified the positions of the pathways and their seasonal variations statistically. The offshore south branch (OSC) and the offshore north branch (ONC) show two different pathways at the Yamato Basin in winter and in summer. The seasonal development and position of anti-cyclonic eddy (ACE) and cyclonic eddy (CE) cause those changes of the pathways. In this way,

mesoscale eddies have a significant influence on the variation of ocean currents.

While this study focused mainly on the seasonal variation, currents and eddies have multiple temporal scales. Hirose and Ostrovskii (2000) found an interannual variation with a period of 2.5 years of the ACEs in the Yamato Basin. Using a map of the velocity derived from surface drifting buoys Watanabe et al. (2009) clarified that the interannual variation of the ACE influences the TWC pathway. We found that temperature anomaly from the monthly climatology also showed the interannual variation along the PM line which crossed the ACE in the Yamato Basin (Figs. 2-12 and 2-13). The northeastward OSC and ONC pathways were formed when the ACE developed, whereas the coastal pathway along the continental shelf was formed when the ACE decreased.

Using our 25-year dataset of TWC pathways we can examine longer variations than previous studies done. Figure 4-1 shows the yearly timeseries of current magnitude and path length of the ONC. They gradually increase through all our analyzing period from 1993 to 2015. This tendency implies a long-term variation internally occurred in the Sea of Japan, because the geostrophic current magnitude around the Tsushima Strait was not increased. Although it is difficult to specify what phenomena cause it because our knowledge on the Sea of Japan is limited for such a long term, we attempt to point out a possibility. The Sea of Japan is very small, but it has its own thermohaline circulation. Its

temporal scale of the circulation is one order smaller than that in other oceans, and

therefore the impacts of global warming observed sooner: dissolved oxygen in bottom

water of the Japan Sea Proper Water (JSPW) decreases and it is ascribed by the decline

of the formation of JSPW which sinks offshore Vladivostok, Russia (Gamo et al., 1986;

Gamo, 1999). The upper part of the thermohaline circulation plays a minor role in the

surface circulation of the Sea of Japan, but the weakening should affect the TWC

pathways. At the present, phenomena with large spatiotemporal scales is not observed

from shipboard surveys, but a method such in this study can be utilized well. In the future,

a collaborated work can clarify their full picture.

We analyzed the monthly mean pathways because we took into account the

coarse temporal resolution of the satellite observation for sea surface height (SSH). As

shown in Figs. 2-6 and 2-16, the pathways change month by month apparently greatly.

The baroclinic instabilities would affect such short-term variations of the pathways, as

suggested by Hase et al. (1999) who examined the variability of the OSC pathways using

multi-year hydrographic data. To apply our method for such short-term phenomena

including frontal waves, we need satellites which observe SSH in finer temporal

resolution and they will be developed in the near future. In another way, output of the

numerical simulation is useful if it assimilates a variety of data. The methodology and the

statistical and objective approach in this study can be applied to small-scale phenomena to clarify their dynamics.

According to Chapter 3, the vertical propagations of near-inertial internal waves (NIWs) were affected by mesoscale eddies, and according to Chapter 2, the TWC pathways were also affected by them. NIWs with frequencies smaller than the local inertial frequency are trapped inside a region with a negative vorticity by ACEs and they transport kinetic energy efficiently to the deep layers (Kunze, 1985; Jeon et al., 2019). Additionally, the geostrophic adjustment of mesoscale eddies generates internal waves (Vanneste, 2013). We showed that the NIWs in the southern part of the Sea of Japan were influenced strongly by the currents and eddies, because the TWC flows there and the eddy kinetic energy is extremely higher than in regions far from it (Fig. 2-12). This is the reason that we planned to observe current velocity by the mooring system off Sado Island. As we expected, the kinetic energy was high at the bottom of the ACE where the vertical shear of the 10-day mean current magnitude was strong.

By breaking, NIWs transfer kinetic energy to microscale phenomena such as turbulent mixing. Similar transfer through submesoscale phenomena is clarified recently with numerical simulations (e.g., Ito et al., 2019). Observational studies for submeso- and microscales have just started with the progress of measurement instruments. In June 2021,

we carried out hydrographic observations across an ACE to investigate the submesoscale

structure in the Yamato Basin, which is one of the high eddy activity areas in the Sea of

Japan and the ACE exists throughout a year (Fig. 2-12). According to our analysis, the

seasonal variation of the ACE in the area is more evident than that off Sado Island (Fig.

2-14). We will clarify the relationship among the NIWs, the submesoscale structures and

the turbulent mixing in our future work.

The turbulent mixing caused by NIWs leads to the upwelling from the deep layer

to the surface layer. Sinking occurs in limited areas in the subarctic region to compensate

it, and the upwelling forms a cyclonic abyssal circulation. The microscale turbulence is

thus responsible for the largest phenomenon of the thermohaline circulation (Munk and

Wunsch, 1998). As we mentioned above, the formation of the JSPW off Vladivostok and

the resulting abyssal circulation are weakening due to global warming in recent years

(Gamo et al., 1986; Gamo, 1999). Studies to examine the influence of the NIWs on global

warming are thus challenging. The Sea of Japan would be the most appropriate field for

such studies because of rapid change due to its smallness. In addition, the upwelling by

turbulent mixing is a key role in supplying nutrients from the deep layer to the surface

layer (Tanaka, 2017), and it maintains the primary production in biomass. The TWC

originates from the Kuroshio which is nutrient-poor, and therefore the turbulent mixing

should be particularly important in the Sea of Japan whose abundant fishery product is a benefit for Japan. Multiscale phenomena are interacted not only between physical processes but also the biogeochemical circulation.

This study focused on the phenomena in the Sea of Japan which closely related to Japanese life, climate, and industries, but the North Pacific, the East China Sea, and the Sea of Okhotsk are also adjacent to Japan. In particular, the Sea of Okhotsk is similar to the Sea of Japan because both sea is extremely closed and deep. In Chapter 2, we examined the TWC which enters from the Tsushima Strait and branches by being trapped along the coastline of the Japan and the Korean Peninsula. They are strongly influenced by the bottom topography of the Yamato Rise and the Noto Peninsula in the downstream region as well. Studies using the satellite altimetry have been used for the North Pacific but has not been applied to other marginal seas. The Sea of Okhotsk will be interesting because of similarity. Its water originates from the East Kamtchatka Current and enters between a few straits between the Kuril Islands. Not only Hokkaido faces this sea, but also the partly originating Oyashio flows off the Pacific coast. Our method will be able to track pathways of the surface currents there. In Chapter 3, we clarified the vertical propagation of the NIW was influenced by the high eddy activity and the existence of extremely uniform JSPW. The NIW is a ubiquitous phenomenon in the world's oceans,

but the behavior is still unclear. Another key energy source of the internal gravity waves is tides. Because the tidal currents in the Sea of Japan is extremely small compared to other seas. However, the interaction between the NIW and the tidal currents will be a topic. In particular the tidal mixing in the Kuril Island straits is a cause of Intermediate North Pacific Water which spreads widely.

We handle only a few of scales in this study, but through them we can stress the importance of interactions among the multiscale phenomena. Many phenomena affect not only the oceanography, but also the meteorology, ocean utilization and our social living, and therefore their comprehensive studies are essential for earth science.
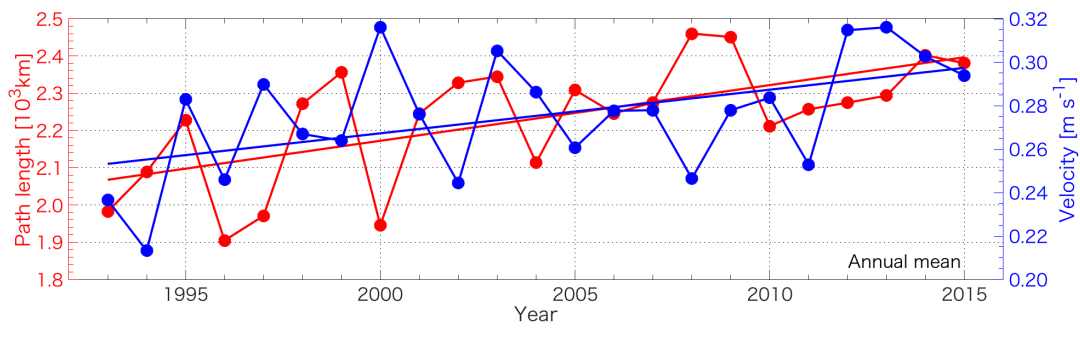
Fig.4-6: Timeseries of annual mean path length (red) and current magnitude (blue) for the ONC.

References

Alford, M. H., MacKinnon, J. A., Simmons, H. L., Nash, J. D., 2016. Near-Inertial Internal Gravity Waves in the Ocean. Annu. Rev. Mar. Sci. 8, 95-123, doi: 10.1146/annurev-marine-010814-015746.

Byun, S., Park, J. J., Chang, K., Schmitt, R. W., 2010. Observation of near-inertial wave reflections within the thermostad layer of an anticyclonic mesoscale eddy. Geophys. Res. Lett. 37, L01606, doi:10.1029/2009GL041601.

Cairns, J. L., Williams G., 1976. Internal waves observation from a mid water float, J. Geophys. Res., 81, 1943–1950.

Chelton, D.B., Schlax, M.G., Samelson, R.M., 2011. Global observations of nonlinear mesoscale eddies. Prog. Oceanogr. 91 (2), 167-216.

Cushman-Roisin, B., and J. M. Beckers. 2011: Introduction to geophysical fluid dynamics: Physical and numerical aspects. Academic Press, 828pp.

Cuypers, Y., X. Le Vaillant, P. Bouruet-Aubertot, J. Vialard, and M. J. McPhaden, 2013. Tropical storm-induced near-inertial internal waves during the Cirene experiment: Energy fluxes and impact on vertical mixing, J. Geophys. Res. Oceans, 118, 358–380, doi:10.1029/2012JC007881.

Danioux, E., Klein, P., Riviére, P., 2008. A resonance mechanism leading to wind-forced motions with a 2f frequency. J. Phys. Oceanogr. 38, 2322–2329. doi:10.1175/2008JPO3822.1.

D'Asaro, EA., 1985. The energy flux from the wind to near-inertial motions in the mixed

layer. J. Phys. Oceanogr. 15, 1043-1059.

Fukudome, K., Yoon, J., Ostrovskii, A., Takikawa, T., Han, I., 2010. Seasonal Volume Transport Variation in the Tsushima Warm Current through the Tsushima Straits from 10 Years of ADCP Observations. J. Oceanogr. 66 (4), 539-551.

Gamo, T., Nozaki, Y., Sakai, H., Nakai, T., Tsubota, H., 1986. Spacial and temporal variations of water characteristics in the Japan Sea bottom layer. Journal of Marine Research 44, 781–793.

Gamo, T., 1999. Global warming may have slowed down the deep conveyor belt of a marginal sea of the northwestern Pacific: Japan Sea. Geophys. Res. Lett., 26 (20), 3137–3140.

Garrett, C., Munk, W., 1975. Space-time scales of internal waves: a progress report. J Geophys Res 80:291–297.

Gill A. E., 1982. Atmosphere Ocean Dynamics. Academic Press. pp. 662.

Gossard, E. E., Hooke, W. H., 1975. Waves in the Atmosphere. Elsevier, Amsterdam.

Hanawa, K., Mitsudera, H., 1985. On the constructing daily mean data from oceanic data-note on dealing with daily mean data (in Japanese). Bull. Coast. Oceanogr. 23, 79-87.

Hase, H., Yoon J., Koterayama W., 1999. The Current Structure of the Tsushima Warm Current along the Japanese Coast. J. Oceanogr. 55(2), 217-235.

Hirose, N., Ostrovskii, A.G., 2000. Quasi-biennial variability in the Japan Sea. J. Geophys. Res. 105(C6), 14,011-14,027. doi:10.1029/2000JC900046.

Hirose, N., Kumaki, Y., Kaneda, A., Ayukawa, K., Okei, N., Ikeda, S., Igeta, Y., Watanabe, T., 2017. Numerical simulation of the abrupt occurrence of strong current in the southeastern Japan Sea. Cont. Shelf Res., 143, 194-205.

Hosoda, S., T. Ohira, K. Sato, T. Suga, 2010. Improved Description of Global Mixed-Layer Depth Using Argo Profiling Floats. J. Oceanogr. 66, 773-787.

Igeta, Y., Yankovsky, A., Fukudome, K., Ikeda, S., Okei, N., Ayukawa, K., Kaneda, A., Watanabe, T., 2017. Transition of the Tsushima Warm Current Path Observed over Toyama Trough, Japan. J. Phys. Oceanogr. 47, 2721–2739. doi:10.1175/ JPO-D-17-0027.1.

Isobe, A., 1997. The determinant of the volume transport distribution of the Tsushima Warm Current around the Tsushima/Korea Straits. Cont. Shelf Res., 17(3), 319-336.

Isobe, A., Ando, M., Watanabe, T., Senjyu, T., Sugihara, S., Manda, A., 2002. Freshwater and temperature transports through the Tsushima–Korea Straits. J. Geophys. Res. 107(C7), doi:10.1029/2000JC000702.

Isoda, Y., 1994. Warm Eddy Movements in the Eastern Japan Sea. J. Oceanogr. 50(1), 1-15.

Ito, M., Morimoto, A., Watanabe, T., Katoh, O., Takikawa, T., 2014. Tsushima Warm Current paths in the southwestern part of the Japan Sea. Prog. Oceanogr. 121, 83-93.

Ito, D., Kouketsu, S., Suga, T. 2019. Submesoscale Oceanography: Findings and approach through observation. (in Japanese, with English Abstract). J.

Oceanogr. 28(4, 5, 6), 75-95, doi: 10.5928/kaiyou.28.4-5-6_75.

Jeon, C., Park, JH., Park, YG. 2019. Temporal and Spatial Variability of Near-Inertial Waves in the East/Japan Sea From a High-Resolution Wind-Forced Ocean Model. J. Geophys. Res. 124. 6015-6029, doi:10.1029/2018JC014802.

Kato, O., 1994. Structure of the Tsushima Current in the Southwestern Japan Sea. J. Oceanogr. 50(3), 317-338.

Kaneda, A., Ayukawa, K., Hirose, N., Tsuzuki, J., Kumaki, Y., Senjyu, T., Igeta, Y., Watanabe, T. 2017. Sudden strong current generated by an eddy in the eastern part of Wakasa Bay, Japan. J. Oceanogr., 73, 181-192, doi:10.1007/s10872-016-0395-8.

Kawabe, M., 1982a. Branching of the Tsushima Current in the Japan Sea. Part I. Data Analysis. J. Oceanogr. Soc. Japan, 38(2), 95-107.

Kawabe, M., 1982b. Branching of the Tsushima Current in the Japan Sea. Part II. Numerical Experiment. J. Oceanogr. Soc. Japan, 38(4), 183-192.

Kawaguchi, Y., Wagawa, T., Igeta, Y., 2020. Near-inertial internal waves and multiple-inertial oscillations trapped by negative vorticity anomaly in the central Sea of Japan. Prog. Oceanogr. 181, 102240.

Kawaguchi, Y. Wagawa, T., Yabe, I., Ito, D., Senjyu, T., Itoh, S., Igeta, Y., 2021a. Mesoscale-dependent near-inertial internal waves and microscale turbulence in the Tsushima Warm Current. J. Oceanogr. doi:10.1007/s10872-020-00583-1.

Kawaguchi, Y., Yabe, I., Wagawa, T., 2021b. On Research Program of the Tsushima Warm

Current in the Sea of Japan, named "FATO" (in Japanese). Gekkan Kaiyo, 53.

Kunze, E., 1985. Near-Inertial Wave Propagation in Geostrophic Shear. J. Phys. Oceanogr. 15, 544-565.

Kunze, E., R. W. Schmitt, J. M. Tool, 1995. The Energy Balance in a Warm-Core Ring's Near-Inertial Critical Layer. J. Phys. Oceanogr. 25, 942-957.

Leaman, K.D., Sanford, T.B., 1975. Vertical energy propagation of inertial waves: a vector spectral analysis of velocity profiles. J. Geophys. Res. 80, 1975–1978.

Lee, D.-K., Niiler, P.P., 2010. Surface circulation in the southwestern Japan/East Sea as observed from drifters and sea surface height. Deep-Sea Res. I 57, 1222-1232.

Lee, M.C., Thomas, L.N., Yoshikawa, Y., 2006. Intermediate Water Formation at the Japan/East Sea Subpolar Front. Oceanography, 19(3), 110-121, doi:10.5670/oceanog. 2006.48.

MacKinnon, J. A., and Coauthors, 2017: Climate process team on internal wave–driven ocean mixing. Bull. Amer. Meteor. Soc., 98, 2429–2454, doi:10.1175/ BAMS-D-16-0030.1.

McTaggart, K.E., Johnson, G.C., Johnson, M.C., Delahoyde, F.M., Swift, J.H., 2010. The GO-SHIP repeat hydrography manual: a collection of expert reports and Guidelines. IOCCP Report 14, ICPO Publication Series No. 134 Version 1.

Massel S. R., 2015. Internal gravity waves in the shallow seas. Springer, Berlin, pp. 163.

Mori, K., Matsuno, T., Senjyu, T., 2005. Seasonal/Spatial Variations of the Near-Inertial Oscillations in the Deep Water of the Japan Sea. J. Oceanogr., 61, 761–773.

Morie, R., Isoda, Y., Fujiwara, S., Xaorong, F., 2015. The contribution of standing Rossby waves to the development of the Tsushima Warm Current-meandering (in Japanese, with English Abstract). J. Oceanogr. 24(1), 29–47.

Morimoto, A., Yanagi, T., Kaneko, A., 2000. Eddy Field in the Japan Sea Derived from Satellite Altimetric Data. J. Oceanogr. 56(4), 449-462.

Morimoto, A., Yanagi, T., 2001. Variability of Sea Surface Circulation in the Japan Sea. J. Oceanogr. 57(1), 1-13.

Munk, W., Wunsch, C. 1998. Abyssal recipes II: Energetics of tidal and wind mixing, Deep Sea Res., Part I, 45, 1977– 2010, doi:10.1016/S0967-0637(98)00070-3.

Naganuma, K., 1985. Fishing and Oceanographic Conditions in the Japan Sea (in Japanese, with English Abstract). Umi Sora 60, 89-103.

Nakano, H., Tsujino, H., Sakamoto, K., Urakawa, S., Toyoda, T., Yamanaka, G., 2018. Identification of the fronts from the Kuroshio Extension to the Subarctic Current using absolute dynamic topographies in satellite altimetry products. J. Oceanogr. 74(4), 393-420.

Niwa, Y., Hibiya, T., 1997. Nonlinear processes of energy transfer from traveling hurricanes to the deep ocean inertial wave field. J. Geophys. Res., 102(C6), 12469–12477.

Odamaki, M., 1989. Co-oscillating and independent tides of the Japan Sea. J. Oceanogr. 45, 217-232.

Okubo A., 1970. Horizontal distribution of floatable particles in the vicinity of velocity

singularities such as convergence. Deep Sea Res 17:445–454.

Park, K.-A., Ullman, D. S., Kim, K., Chung, J. Y., Kim, K.-R., 2007. Spatial and temporal variability of satellite-observed Subpolar Front in the East/Japan Sea. Deep-Sea Res. I 54, 453-470.

Pollard, R. T., R. C. Millard Jr., 1970. Comparison between observed and simulated wind-generated inertial oscillations. Deep-Sea Res. Oceanogr. Abstr., 17, 813–821, doi:10.1016/0011-7471(70)90043-4.

Polzin K. L., 2008. Mesoscale eddy-internal wave coupling. Part I: symmetry, wave capture, and results from the mid-ocean dynamics experiment. J Phys Oceanogr 38:2556–2574.

Qiu, B., Chen, S., 2005. Variability of the Kuroshio Extension Jet, Recirculation Gyre, and Mesoscale Eddies on Decadal Time Scales. J. Phys. Oceanogr. 35 (11), 2090-2103.

Qiu, B, Chen, S., Hacker, P. 2007. Effect of Mesoscale Eddies on Subtropical Mode Water Variability from the Kuroshio Extension System Study (KESS). J. Phys. Oceanogr. 37 (4), 982-1000.

Senjyu, T., 1999. The Japan Sea Intermediate Water; Its Characteristics and Circulation. J. Oceanogr. 55(2), 111-122.

Senjyu, T., Shin, H. R., Yoon, J. H., Nagano, Z., An, H. S., Byun, S. K., Lee, C. K., 2005. Deep flow field in the Japan/East Sea as deduced from direct current measurements., Deep-Sea Res. II 52, 1726-1741.

Senjyu, T., 2015. Observation of near-inertial waves in the abyssal Japan Sea. La mer, 53, 43-51.

Smith, R. B., 1979. The influence of mountains on the atmosphere. Adv. Geophys., 21, 87-230.

Smyth, W. D., Moum, J. N. 2012. Ocean Mixing by Kelvin-Helmholtz Instability. Oceanography, 25(2), 140-149.

Suda, K., Hidaka, K., 1932. The results of the oceanographical observations on board R.M.S. 'Syunpu Maru' in the southern part of the Japan Sea in the summer of 1929. Part 1 (in Japanese). J. Oceanogr. Imp. Mar. Observ. 3, 291-375.

Talley, L.D., Min, D.H., Lobanov, V.B, Luchin, V.A., Ponomarev, V.I., Salyuk, A.N., Shcherbina, A.Y., Tishchenko, P.Y., Zhabin, I., 2006. Japan/East Sea Water Masses and Their Relation to the Sea's Circulation. Oceanography 19(3), 32-49, doi:10.5670/oceanog. 2006.42.

Tanaka, T. 2017. A brief review of vertical mixing observations at mixing hotspots in the North Pacific (in Japanese, with English Abstract). J. Oceanogr. 26(5), 151-174.

Thomson, R.E., Emery, W.J., 2014. Data Analysis Methods in Physical Oceanography, Third Edition. Elsevier Science, Amsterdam. pp. 728.

Thorpe S. A., 2005. The turbulent ocean. Cambridge University Press, Cambridge.

Vanneste, J. 2013. Balance and Spontaneous Wave Generation in Geophysical Flows. Annu. Rev. Fluid Mech., 45, 147–172, doi:10.1146/annurev-fluid-011212-140730.

Wagawa, T., Kawaguchi, Y., Igeta, Y., 2019. Detailed water properties of baroclinic jets and mesoscale eddies in the Sea of Japan from a glider. J Mar Syst 201:103242. doi:10.1016/j.jmarsys.2019.10324 2

Watanabe, T., Katoh, O., Yamada, H., 2006. Structure of the Tsushima Warm Current in the Northeastern Japan Sea. J. Oceanogr. 62 (4), 527-538.

Watanabe, T., Simizu, D., Nishiuchi, K., Hasegawa, T., Katoh, O., 2009. Surface Current Structure of the Tsushima Warm Current Region in the Japan Sea Derived by Satellite-Tracked Surface Drifters. J. Oceanogr. 65 (6), 791-801.

Watanabe, M., Hibiya, T., 2018. A near-inertial current event in the homogeneous deep layer of the northern Sea of Japan during winter. J. Oceanogr. 74, 209-218.

Whitt, D. B., L. N. Thomas, 2013. Near-Inertial Waves in Strongly Baroclinic Currents. J. Phys. Oceanogr., 43, 706-725.

Wunsch, S., Ku, H., Delwiche, I., Awadallah, R., 2014. Simulations of nonlinear harmonic generation by an internal wave beam incident on a pycnocline. Nonlin. Processes Geophys., 21, 855-868.

Yabe, I., Y. Kawaguchi, T. Wagawa, S. Fujio, 2021a. Anatomical study of Tsushima Warm Current: Principal pathways and variability, Prog. Oceanogr. doi:10.1016/j. pocean.2021.102590.

Yabe, I., Y. Kawaguchi, T. Wagawa, S. Fujio, 2021b. Tsushima Warm Current Pathways and Its Variation - Current Detecting Algorithm – (in Japanese). Gekkan Kaiyo, 53.